T.R.

GEBZE TECHNICAL UNIVERSITY

GRADUATE SCHOOL OF NATURAL AND APPLIED SCIENCES

POWDER AND THIN FILM BASED Ni-YSZ ANODES FABRICATED FROM POLYMERİC PRECURSORS FOR SOLID OXIDE FUEL CELLS

BUSE BILBEY

A THESIS SUBMITTED FOR DEGREE OF

MASTER OF SCIENCE

DEPARTMENT OF MATERIAL SCIENCE AND ENGINEERING

GEBZE

2020

T.R.

GEBZE TECHNICAL UNIVERSITY

GRADUATE SCHOOL OF NATURAL AND APPLIED SCIENCES

POWDER AND THIN FILM BASED Ni-YSZ ANODES FABRICATED FROM POLYMERİC PRECURSORS FOR SOLID OXIDE FUEL CELLS

BUSE BILBEY

A THESIS SUBMITTED FOR DEGREE OF

MASTER OF SCIENCE

DEPARTMENT OF MATERIAL SCIENCE AND ENGINEERING

THESIS SUPERVISOR

ASSIST. PROF. DR. ALIGUL BUYUKAKSOY

GEBZE

2020

T.C.
GEBZE TEKNİK ÜNİVERSİTESİ
FEN BİLİMLERİ ENSTİTÜSÜ

KATI OKSİT YAKIT HÜCRELERİ İÇİN POLİMERİK ÇÖZELTİ YÖNTEMİ İLE ÜRETİLMİŞ TOZ VE İNCE FİLM TEMELLİ Ni-YSZ ANOTLARI

BUSE BİLBEY

YÜKSEK LİSANS TEZİ
MALZEME BİLİMİ VE MÜHENDİSLİĞİ ANABİLİM DALI

DANIŞMANI
DR. ÖĞR. ÜYESİ ALİGÜL BÜYÜKAKSOY

GEBZE
2020

GEBZE TEKNİK ÜNİVERSİTESİ	YÜKSEK LİSANS JÜRİ ONAY FORMU

GTÜ Fen Bilimleri Enstitüsü Yönetim Kurulu'nun 17/07/2020 tarih ve 2020/34 sayılı kararıyla oluşturulan jüri tarafından 24/07/2020 tarihinde tez savunma sınavı yapılan Buse BİLBEY'in tez çalışması Malzeme Bilimi ve Mühendisliği Anabilim Dalında YÜKSEK LİSANS tezi olarak kabul edilmiştir.

JÜRİ

ÜYE

(TEZ DANIŞMANI) : Dr. Öğr. Üyesi Aligül Büyükaksoy

ÜYE : Prof. Dr. Hüseyin Yılmaz

ÜYE : Prof. Dr. Sedat Akkurt

ONAY

Gebze Teknik Üniversitesi Fen Bilimleri Enstitüsü Yönetim Kurulu'nun
…..…/…..…/..…..… tarih ve ……/…….. sayılı kararı.

İMZA/MÜHÜR

SUMMARY

Solid oxide fuel cells (SOFCs) are the possible solution the worlds green energy demand with >60% electrical efficiency. Conventional SOFCs fabrication requires sintering at high temperatures and operation temperature is also high (800-1000˚C) thus two main problems originate. These problems are the low initial performance and performance instability at long-term operation conditions. Ni-cermet anodes are most preferred SOFC anode materials, but chemical and microstructural degradation occur, because of the Ni particle groves, triple phase boundaries(tpbs) become lower and performance reduces. Also, the redox conditions have same problem even leads to cracks and failure.

In this thesis, we aimed to achieve better and stable anode performance from initial to long-term operation. For the higher anode performance long tpbs thus the small particle size needed. To hindered high temperature sintering despite to conventional methods polymeric precursor method used in this study. NiO-YSZ polymeric precursor coated as thin films and heat treatment at 400˚C. Also, powders derived from the polymeric precursors and powder-based anodes produced, even this way requires sintering at high temperatures performance better than the conventional method. X-ray diffraction, particle size distribution and thermal analysis performed for analysis the crystal structure. Microstructural analysis performed with scanning and transmission electron microscopies (SEM, TEM), electrochemical impedance spectroscopy (EIS) and viscosities analysis also performed.

Key words: Solid Oxide Fuel Cells, Polymeric Precursor Method, Ni-cermet Anodes, NiO-YSZ, Thin film, Nanostructured Composite Powder, Impedance Spectroscopy.

ÖZET

Katı oksit yakıt hücreleri (KOYH) dünyanın enerji gereksinimini karşılayabilecek doğaya zararı olmaya enerji çözümlerinden biridir ve %60 üzerinden bir elektriksel verimlidir. Geleneksel olarak KOYH üretimi yüksek sıcaklıklarda sinterleme gerektirir ve çalışma sıcaklıkları da aynı zamanda yüksektir (800-1000˚C), bu nedenlerden iki ana problem oluşur. Bu problemler başlangıçta düşük performans elde edilmesi ve bu performansın uzun süreli ölçüm şartlarında stabil olmamasıdır. Ni-sermet anotları en çok tercih edilen KOYH anot malzemeleridir, fakat kimyasal ve mikro yapısal degradasyon meydana gelir çünkü Ni parçacıkları büyür, üçlü faz sınırı (üfs) azalır ve performans kötüleşir. Aynı zamanda, redoks şartlarında aynı problem görülür hatta çatlak oluşumu ve kırılma olabilir.

Bu tezde, başlangıçtan uzun süreli çalışma şartlarına kadar daha iyi ve stabil anot performansına ulaşmayı hedefledik. Daha yüksek anot performansı için daha uzun üfs yani daha küçük parçacık boyutuna ihtiyaç vardır. Bu çalışmada geleneksel yöntemlerin tersine yüksek sıcaklıkta sinterlemeyi engelleyebilmek için polimerik çözelti yöntemi kullanılmıştır. NiO-YSZ polimerik çözeltisi ince film olarak kaplanmış ve ısıl işlem sıcaklığı 400˚C' ye düşürülmüştür. Aynı zamanda polimerik çözeltilerden tozlar üretilmiş ve toz-temelli anot üretilmiştir, bu yöntem yüksek sıcaklıkta ısıl işlem gerektirmesine rağmen geleneksel yöntemden performansı daha iyidir. X-ray difraksiyonu, parçacık boyutu dağılımı ve termal analizler kristal yapı analizleri için yapılmıştır. Mikro yapısal analizler taramalı ve geçirimli elektron mikroskopları (SEM ve TEM), elektrokimyasal empedans spektroskopisi ve viskozite analizleri aynı zamanda ölçülmüştür.

Anahtar Kelimeler: Katı Oksit Yakıt Hücreleri, Polimerik Çözelti Yöntemi, Ni-sermet Anotları, NiO-YSZ, İnce Film, Nano Yapılı Kompozit Toz, Empedans Spektroskopisi.

ACKNOWLEDGEMENTS

Firstly, I would like to express my deep and sincere gratitude to my supervisor, Assist. Prof. Dr Aligül Büyükaksoy, who not only shared his profound scientific knowledge with me, but he also encouraged and guided me.

I would like to thank Prof. Dr Ahmet Yavuz Oral, Prof. Dr Cleva Ow-Yang, Assoc. Prof. Dr Meltem Sezen, Ahmet Nazım and Adem Şen for their supports for my experimental studies.

I would like to thank my thesis committee members Prof. Dr Hüseyin Yılmaz and Prof. Dr Sedat Akkurt.

I want to thank Prof. Dr Søren Højgaard Jensen for giving an opportunity to work at Energy Department of Denmark Technical University also his support and precious scientific knowledge. I would like to also thank Dr Theis Løye Skafte and Anne Lyck Smitshuysen for their helps and supports.

I am thankful for my research group friends to their supports.

I am grateful to my parents Filiz and Selahattin and grandparents Mesrure and Enver Öztürk for their love and support.

Finally, I would like to thank TUBITAK to financial funding. (Project no: 217M031)

TABLE of CONTENTS

LIST of ABBREVIATIONS and ACRONYMS

Abbreviations and Acronyms		**Explanations**
E	:	Open Circuit Potential, Voltage
E°	:	Standart Potential
R	:	Ideal Gas Constant
T	:	Temperature
F	:	Faraday Constant
n	:	Numbers of Electrons
p_i	:	Partial Pressure of the Gasses
O^{2-}	:	Oxygen ion
H_2	:	Hydrogen gas
H^+	:	Hydrogen ion
$Vo^{\bullet\bullet}$	:	Oxygen vacancy
Ω	:	Ohm
λ	:	Wavelength
θ	:	Diffraction angle
B	:	Full width at half maximum intensity
Z_0	:	Function of amplitude
Z_{real}	:	Real impedance
Z_{imag}	:	Imaginary impedance
Z'	:	Z real
Z''	:	Z imaginary
I	:	Current
E_t	:	Potential at the t time
E_0	:	Applied AC voltage
ω	:	Frequency as radial (rad/sec)
f	:	Frequency
I_t	:	Responded current to applied AC voltage
I_0	:	Applied current
∅	:	Phase shift

Å	:	Angstrom
t/m²	:	Ton/(meter)^2
S/m	:	Siemens per meter
Ar	:	Argon
C_1	:	High frequency capacitance
C_2	:	Low frequency capacitance
D_p	:	Average crystallite size
Ea	:	Activation energy
$Ea_{Ni\text{-}YSZ}$	:	Activation energy of Ni-YSZ anode
Ea_{TPB}	:	Activation energy of electron transfer at the triple phase boundary
Ea_{YSZ}	:	Activation energy of oxygen ion transportation in the YSZ network
R	:	Resistance
Rs	:	Series Resistance
R_P	:	Polarization Resistance
R_{anode}	:	Resistance of anode
R1	:	High Frequency resistance
R2	:	Low frequency resistance
S	:	Siemens
V	:	Volt
Q1	:	Constant phase element of R1
Q2	:	Constant phase element of R2
ΔT	:	Temperature difference
Al_2O_3	:	Alumina
CeO_2	:	Cerium dioxide, ceria
MgO	:	Magnesium oxide
SiC	:	Silicon carbide
Y_2O_3	:	Yttrium (III) Oxide
ZrO_2	:	Zirconium dioxide
µm	:	Micrometer
mm	:	Milimeter
nm	:	Nanometer
cm	:	Centimeter
mV	:	Millivolt

Pa	:	Pascal
MPa	:	Mega Pascal
mPa.s	:	Mili Pascal second
mA	:	Mili Amper
F	:	Farad
Hz	:	Hertz
h	:	Hour
rpm	:	Rounds per minute
AA	:	Ascorbic Acid
AC	:	Alternative current
AFC	:	Alkaline Fuel Cell
ASR	:	Area Specific Resistance
ASR1	:	Ohmic Resistance
ASR2	:	2 electrode resistance
ASR_{anode}	:	Anode resistance
CA	:	Citric Acid
Ccl	:	Currenct collector layer
CIP	:	Cold Isostatic Press
CTAB	:	Cetyltrimeyhyl Ammonium Bromide
DTA	:	Differential Thermal Analysis
EG	:	Ethylene Glycol
EIS	:	Electrochemical impedance spectroscopy
FC	:	Fuel Cell
GDC	:	Gadolinium-doped ceria
ht	:	Heat treatment
LSC	:	Strontium doped lanthanum cobaltite
LSGM	:	Sr and Mg doped $LaGaO_3$
LSM	:	Strontium doped lanthanum manganite
MCFC	:	Molten Carbonate Fuel Cell
MEIC	:	Mixed electronic and ionic conductor
Nh	:	No heat treatment
PAFC	:	Phosphoric Acid Fuel Cell
PEMFC	:	Proton Exchange Membrane

SDC	:	Samarium doped Ceria
SEM	:	Scanning electron microscopy
SOFC	:	Solid Oxide Fuel Cell
TEM	:	Transmission electron microscopy
TG	:	Thermogravimetric Analysis
TPB	:	Triple phase boundary
XRD	:	X-ray diffraction
YSZ	:	Yttria stabilized Zirconia
8YSZ	:	8 mol Yttria Stabilized Zirconia

LIST of FIGURES

LIST of TABLES

1. INTRODUCTION

1.1. Fuel Cells as a Possible Solution to The Energy Problem

Increasing world population, developing technology and improved standard of life enhance the energy demand. These energy needs are mostly met by the burning of fossil fuels (crude oil, coal and gas), which are comprised of hydrocarbons. Burning hydrocarbons to produce energy is a problematic approach mostly because it generates CO_2 emissions and thereby causes global warming [1]. Also, in the long view, fossil fuel resources are limited, not renewable, world coal resource and the demand shown in figure 1.1 [2]. For these reasons researchers have focused on the generation of environmentally clean and efficient ways to generate electricity.

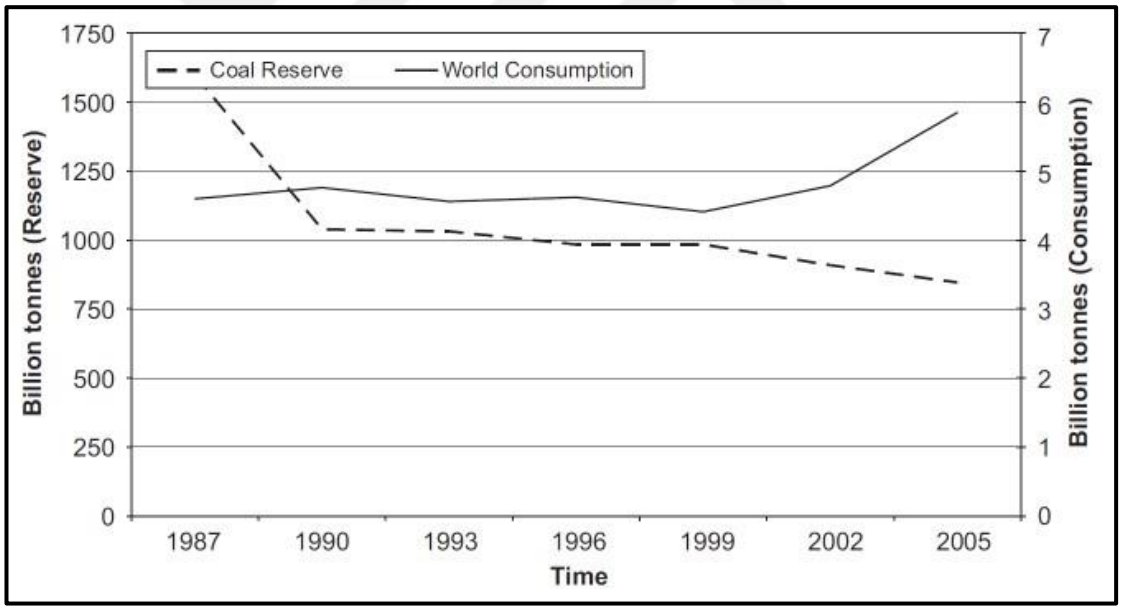

Figure 1.1: Trends of the world coal reserves and demand from 1987 to 2005. (Data collected from EIA and BP.

Among many alternatives, such as solar cells and wind turbines, fuel cells (FC) are being considered as a possible solution to this green energy demand [2-4], due to their superior efficiency (Table 1, 2). The origin of fuel cells goes back to Sir William Grove's invention of the so-called "gaseous voltaic cell" in 1839, where the generation of an electric potential difference in the presence of two different gases on

two separate surfaces of an ionic conductor material was demonstrated for the first time [5].

Table 1.1: Comparison of different energy generation systems.

Energy Generation Systems	**Capacity Range**	**Efficiency**	**Capital Cost ($/kW)**	**O&M Cost ($/kW)**
Reciprocating engine: Diesel	500 kW to 5 MW	35%	200-350	0.005-0.015
Turbine Generator	500 kW to 25 MW	29-42%	450-870	0.005-0.0065
Photo Voltaics	1 kW to 1 MW	6-19%	6600	0.001-0.004
Wind Turbine	10 kW to 1 MW	25%	1000	0.01
Fuel Cells	200 kW to 2 MW	40-60%	1500-3000	0.0019-0.0153

There are several types of fuel cells currently being investigated for mobile or stationary applications. The classification of fuel cells is based on the type of the ion conductor electrolyte material, namely, molten carbonate fuel cell (MCFC), phosphoric acid fuel cell (PAFC), proton exchange membrane (PEMFC), alkaline fuel cell (AFC) and solid oxide fuel cell (SOFC). Table 1.2 summarizes some general information about these fuel cell types. [3,7]

Table 1.2: Comparation of fuel cell systems.

Fuel cell type	**Typical electrolyte**	**Charge carrier**	**Operation temperature(°C)**	**Electrical efficiency (%)**
MCFC	Liquid molten carbonate	CO_3^{2-}	600-700	50-55%
PAFC	Liquid phosphoric acid	H^+	160-220	35-45%
PEMFC	Ion exchange membranes	H^+	60-180	40-60%
AFC	Aqueous solution of KOH	OH^-	65-220	60%
SOFC	Solid ceramic	O^{2-}	600-1000	>60%

2. SOLID OXIDE FUEL CELLS

The typical solid oxide fuel cell (SOFC)structure, shown in Figure 2.1, consists of a dense ceramic electrolyte placed in the middle of porous cathode and anode, preventing the intermixture of air and fuel gases. The driving force for power generation in SOFCs is the electric potential difference (called open circuit voltage, OCV) generated as a result of the chemical potential difference between the oxygen and fuel, e.g., hydrogen gases. The magnitude of the OCV follows the Nernst equation (Equation 2.1):

$$E = E^{o} + \frac{R.T}{n.F}\ln\left(\frac{p_{H_2}p_{O_2}^{1/2}}{p_{H_2O}}\right) \quad (2.1)$$

where, E is the open circuit potential, E° is the standard potential, R is the ideal gas constant (8,31 $J.mol^{-1}.K^{-1}$), T(K) is the temperature, n is the number of electrons, F is the Faraday constant (9,65x10^{4} $C.mol^{-1}$), n is the number of electrons which is 2 in this system and p_i is the partial pressure of the gases.

The electrochemical reactions that take place upon the drawing of current from the fuel cell are schematically depicted in Figure 2.1. At typically SOFCs operated at 700-900°C when fuel and air gases reach the anode and cathode hydrogen absorbed at the anode and ionized (Equation 2.2), then the oxygen gas absorbed at the cathode (Equation 2.3) with electrons which arrives from first equation (Equation 2.2). The oxide ion O^{2-} is conducted from cathode to anode by ionic conductor ceramic electrolyte. O^{2-} ions at the anode react with H_2, then hydrogen gives electrons and water forms. (Equation 2.4), that circuit is shown in Figure 2.1. When the anode fed with fuel that is oxidized, oxygen reduction reactions takes place at the cathode.[8]

The reaction on the anode side is:

$$H_2 = 2H^{+} + 2e^{-} \quad (2.2)$$

The reaction on the cathode side is:

$$\frac{1}{2}O_2 + 2e^{-} = O^{2-} \quad (2.3)$$

The overall reaction on SOFC system:

$$O^{2-} + H_2 = H_2O + 2e^- \quad (2.4)$$

Although the operating principle of solid oxide fuel cells – and fuel cells in general – resemble that of a battery, a major difference between these two types of devices exist: A fuel cell system can produce electrical energy as long as continuous oxidant and fuel gas feeds are maintained [6].

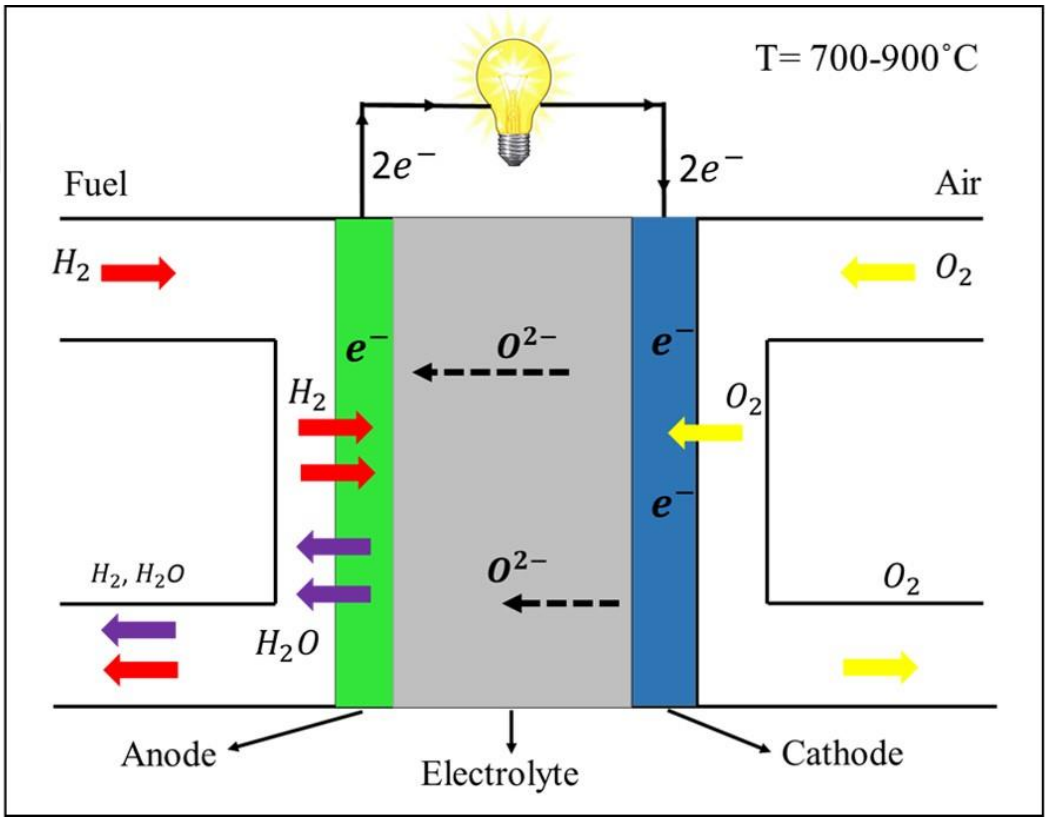

Figure 2.1: Schematic representation of the electrochemical reactions that take place in an SOFC during operation.

2.1. SOFC Components and Material Selection

Originating from the fact that different electrochemical processes take place in each SOFC component, they all require different properties.

2.1.1. Electrolyte

As shown in Figure 2.1, in a SOFC, O^{2-} ions must be passing from cathode through the electrolyte and to the anode, while not allowing any electron or gas passage. Thus, the electrolyte must be a dense ceramic with a high oxygen ion conductivity (0,03-0,1 $S.cm^{-1}$ at 800 and 1000°C) but also with no electronic conductivity under both oxidizing and reducing atmospheres [9].

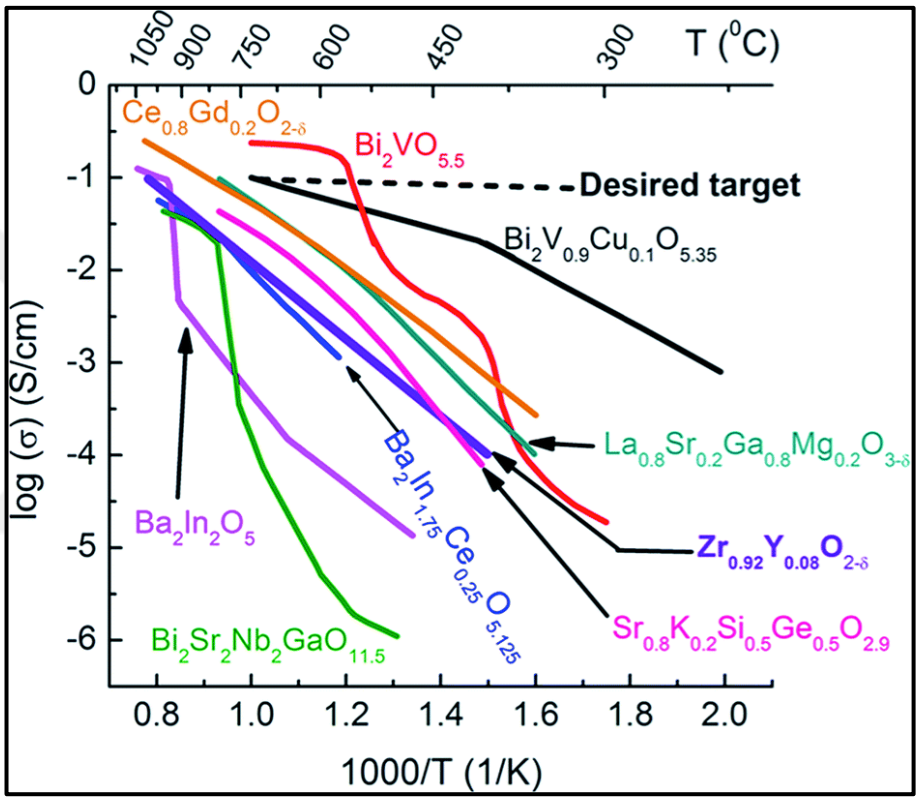

Figure 2.2: Temperature dependent oxide ion conductivities of common electrolyte materials.

Ionic conductivity of electrolyte material candidates at different temperatures are shown in Figure 2.2 [10-13]. Despite the fact that yttria stabilized zirconia (YSZ) does not exhibit the highest ionic conductivity (Figure 2.2), it is one of the most widely preferred materials. This is due to its extremely high chemical stability under reducing and oxidizing atmospheres [14]. The ionic conduction in YSZ, like many other oxides, takes place via the vacancy diffusion of the oxygen ions, which renders the oxygen vacancy concentration detrimental to the ionic conductivity of the

material. The generation of oxygen vacancies in the ZrO_2 matrix is ensured by the Y_2O_3 doping, expressed in Equation 2.5 in terms of Kröger-Vink notation.

$$Y_2O_3 \xrightarrow{ZrO_2} 2Y'_{Zr} + 3O^x_O + V_{\ddot{O}} \qquad (2.5)$$

Besides oxygen vacancy generation, At the same temperature, Y_2O_3 doping also stabilizes the cubic fluorite structure – which also allows facile oxygen diffusion - over a wide temperature range. Figure 2.3. shows the ZrO_2 - Y_2O_3 phase diagram [15], indicating that at Y_2O_3 contents higher than 8 mol% cubic YSZ are stabilized. Besides its high oxide ion conductivity, the extremely low electronic conductivity of YSZ is another parameter that makes it a preferable electrolyte material.

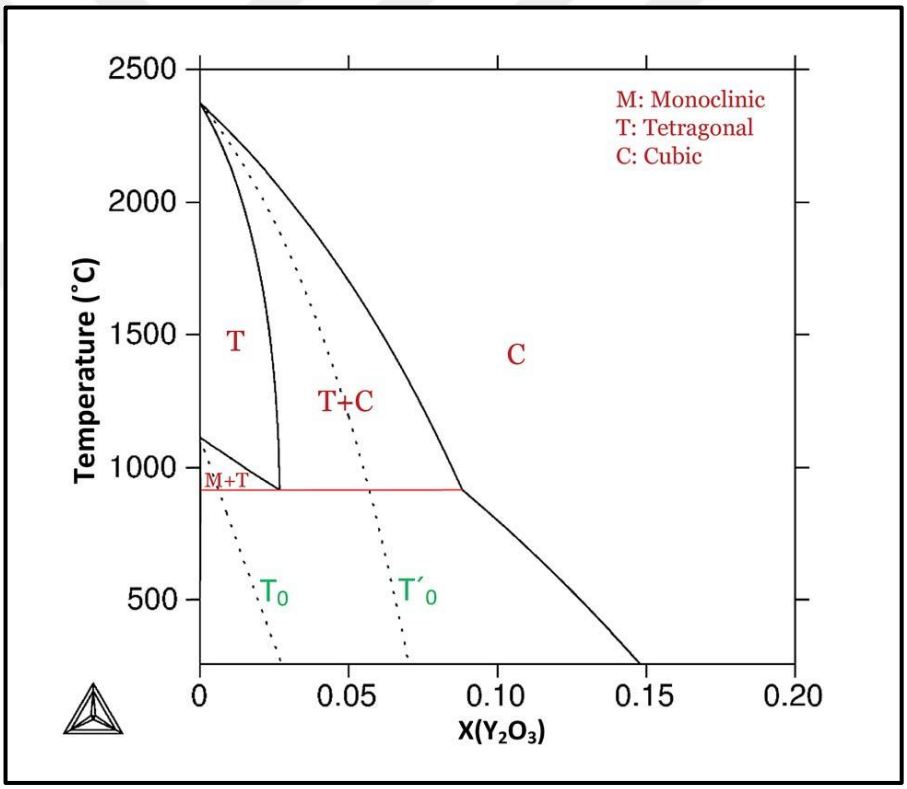

Figure 2.3: A part of Y_2O_3-ZrO_2 phase diagram.

2.1.2 Cathode

Reduction of oxygen takes place at the cathode. The requirements for a high performance cathode material are high electrocatalytic activity for oxygen reduction, high electronic and ionic conductivity, physical and chemical stability under an oxidizing atmosphere, ca. 30% porosity and matching thermal expansion coefficient to those of other SOFC components.

Initially, noble metals, such as Pt, Pd, Au, and Ag were considered as cathode materials. The low melting temperature and high vapour pressure of Ag, Au and Pd render these materials not suitable for cathode applications, especially in SOFCs that operate at ≥800 °C [4]. Although Platinum exhibits high electrocatalytic activity for oxygen reduction and has a high melting temperature, the fact that it is not cost-efficient has prevented its widespread use. As an alternative, perovskite structured oxides with the general formula ABO_3 have been developed. Figure 2.4 schematically shows the crystal structure of the ABO_3 –type perovskite material, where A and B are cations with a total charge of + 6. A-site cations are generally rare-earth oxides with a 3+ charge, such as La and Sm, doped with IIA elements, such as Sr and Ca. B-site cations are transition metals with a 3+ formal charge such as Fe, Co and Mn. A-site cations are larger than other atoms having 12 neighbouring oxygen atoms, while B-site cations form much smaller octahedral holes with 6 neighbouring oxygen atoms [16].

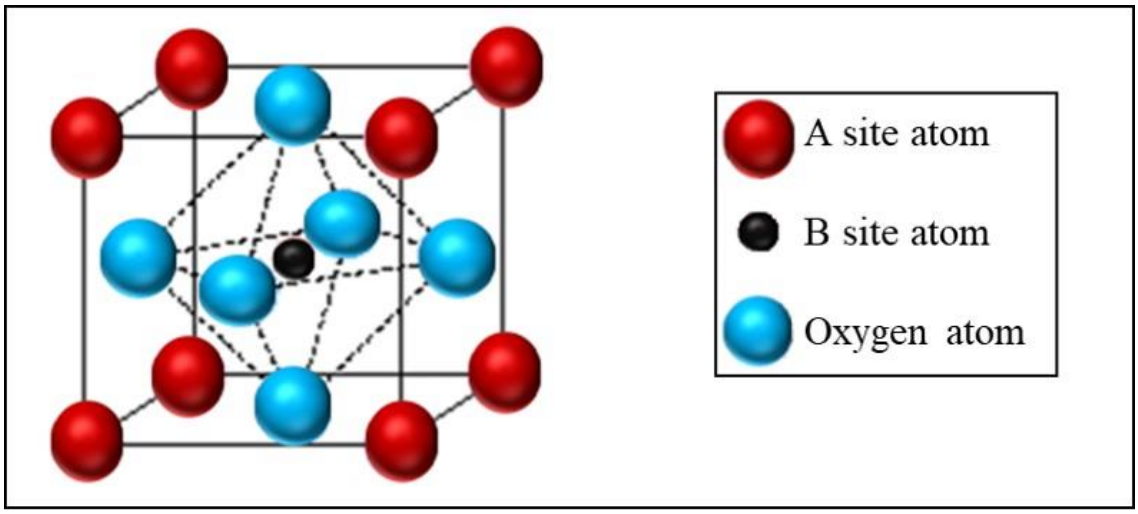

Figure 2.4: Unit cell of an ABO_3-type perovskite oxide.

The most widely used cathode material is lanthanum manganite doped with strontium (LSM), which has an abundance of electron holes as a result of the defect reaction shown in equation 2.6. To enhance the electrochemical performance of LSM, it is usually mixed with an oxygen ionic conductor ceramic, such as YSZ or GDC.

$$O_2 + SrO \xrightarrow{LaMnO_3} Sr'_{La} + Mn_{Mn}^{\cdot} + 3O_O^x \quad (2.6)$$

Another alternative cathode is mixed electronic and ionic conductor (MEIC) perovskites which show both electronic and ionic conductivity all in one material. Strontium doped lanthanum cobaltite (LSC) is an example of such a cathode material, which has an abundance of oxygen vacancies generated through the defect reaction shown in equation 2.7. The MEIC electrocatalysts do not require to be mixed with an oxygen ion conductor material to achieve sufficient performance.

$$\tfrac{5}{2}O_2 + 3SrO \xrightarrow{LaCoO_3} 3Sr'_{La} + V_{\ddot{O}} + 2Co_{Co}^x + Co_{Co}^{\cdot} + 8O_O^x \quad (2.7)$$

2.1.3. Anode

The fuel electrode, anode, must also meet some requirements to work, such as; chemical and physical stability, sufficient electrical conductivity, matching thermal expansion coefficient to prevent flaking between electrolyte and anode, high electrocatalytic activity for fuel oxidation, sufficient electronic and ionic conductivity, long triple phase boundary (TPB), and ca. 30-40% to permit gas diffusion.

2.1.3.1. Ni-Based Anode Materials

Pt, Au, Fe and Ni were the first materials to be tried as SOFC anodes [3]. However, Au and Fe were found to not exhibit high enough electrocatalytic activity, while Pt was too expensive [3,7]. The most preferred anode material up to date is a porous, Ni-ionic conducting ceramic composite (cermet) [8], due to its high electrocatalytic activity, chemical and mechanical stability and effective cost

compared to other possible metals (Co, Pt and Pd) [8,9,17,18]. The ionic conductor ceramic component of the anode cermet is most commonly, yttria-stabilized zirconia (YSZ) [8, while other alternatives are Gd or Sm-doped CeO_2 (GDC, SDC) [19,20,21] and Sr and Mg doped $LaGaO_3$ (LSGM) [22].

The mechanism of fuel oxidation over a typical Ni-YSZ cermet anode is schematically depicted in Figure 2.5, for the case when hydrogen is used as fuel [23]. As shown, hydrogen arriving at the Ni/YSZ interface through the pore channels meets the oxygen ion transported from the electrolyte and through the ionic conductor ceramic phase of the anode and forms water vapour and electrons (Figure 2.5) [24]. The latter is to be collected via the metallic Ni phase to the external circuit, while the former is to be transported out of the system via the interconnected porosity (Figure 2.5). As a result, it can be concluded that the higher the number of sites that allows the meeting of Ni, YSZ and gas phases (i.e., the triple phase boundary-TPB) the higher the reaction rate and thus, the higher the electrochemical performance. Significant research has thus focused on the development of fabrication methods that would allow long TPBs [25,26].

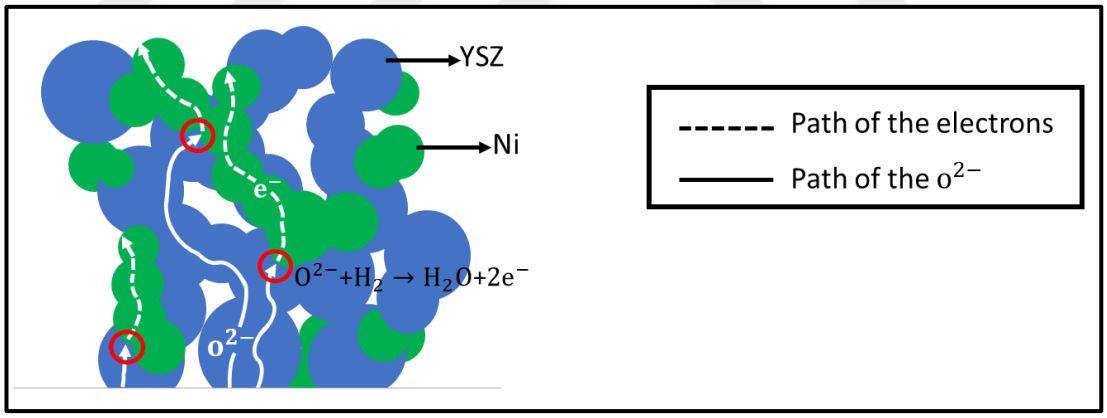

Figure 2.5: Triple phase boundary in Ni-YSZ anodes.

2.1.3.2. Alternative Anode Materials

In addition to Ni-based cermets, some effort has also focused on the development of all ceramic anodes, which would also have to exhibit the same performance requirements (such as; electronic conductivity, ionic conductivity and electrocatalytic activity for fuel oxidation, etc.) to be eligible for use in SOFCs. Since the SOFC anode is subjected to reducing conditions, the ceramic anode is preferred

to exhibit n-type semiconductivity. Below are a few examples of ceramic anodes developed thus far in the literature.

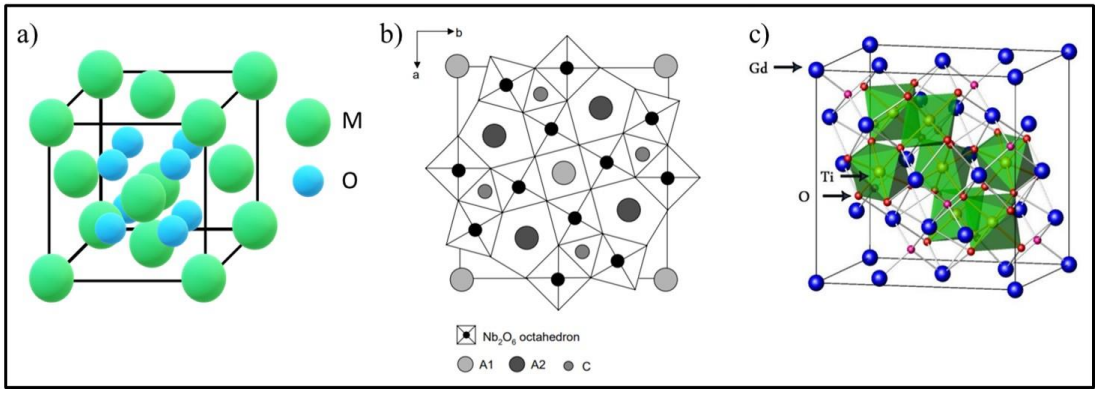

Figure 2.6: Unit cell of a) Fluorite structure, b) Tungsten-bronze structure projected on c-axis c) Pyrochlore structure.

Fluorite anode materials are one of the alternatives ceramics based on CeO_2 exhibit MIEC in the reducing atmosphere, the unit cell of the structure shown in Figure 2.6.a. M and O present Ce and O. Cerium has two stable oxidation states; +4 and +3. The switching between these two states is the essential factor for its catalytic activity. Reduction of Ce^{4+} to Ce^{3+}, causes the oxygen vacancy ($Vo^{\bullet\bullet}$) and electron formation, rendering CeO_2 promising for SOFC anode applications. CeO_2 has been frequently used in the development of coke-resistant anodes, in the form of nanoparticles distributed into a porous YSZ scaffold along with Cu, to boost the electronic conductivity of the overall anode [27,28].

Tungsten bronze anode materials are oxides with the general formula $A_6C_4B_{10}O_{30}$ (with B = Nb, Ta, Mo, W, and A or C = Ba, Na, etc.) and crystallize in the tetragonal and or the orthorhombic tungsten bronze structure (TTB or OTB, respectively), structure shown in Figure 2.6.b [16,29,30]. The pyrochlore-structured oxides have the general formula of $A_2 B_2O_7$ (e.g. $Gd_2Ti_2O_7$) structure of the unit cell shown in figure 2.6.c. Their structure can be derived from fluorite, by removing $1/8$ of the oxygens, ordering the two cations and the oxygen vacancies [16,31].

The perovskite-type oxides have the general formula ABO_3, shown before in Figure 2.4. A and B are cations with a total charge of 6+. A-site cations are usually cations with 2+ or 3+ charge such as; La, Sr or Ca, whereas the B – site is occupied by a transition metal with an effective charge of 3+ or 4+ (e.g., Ti, Cr, Ni, Fe, Co or

Zr). A-site cations are larger than other atoms and are coordinated to 12 oxygen atoms, while the much smaller B cations occupy the octahedral holes and are coordinated to six oxygen neighbor atoms [16]. N-type doping is common practice to improve the electronic conductivity by generating extra charge in the lattice. Doped material valance must be higher than A site valance to achieve n-type doping. For example, $SrTiO_3$-based perovskite could be anode with doping La_2O_3, Y_2O_3, ZrO_2.

Overall, in the table 2.1. [32] anode materials with different structures are compared among each other.

Table 2.1: Comparison of anode materials.

Structure	Typical materials	Stability in reducing atmosphere	Ionic conductivity	Electronic conductivity	Chemical compatibility with YSZ	Thermal compatibility with YSZ	Performance using H_2 as fuel	Performance using CH_4 as fuel	Redox stability
Mixture	Ni-YSZ	✓	✓	✓	✓	✓	✓	✗	✗
Mixture	Cu-YSZ	?	✓	✓	✓	✓	✓	✓	✓
Fluorite	YZT, ScYZT CGO	✓	✓	✗	✓	✓	ok	ok	✓
Perovskite	$La_{1-x}Sr_xCr_{1-y}TM_yO_3$	✓	?	✓	✓	✓	✓	✓	✓
Pyrochlore	Gd_2TiMoO_7	✗	ok	✓	✓	?	?	?	✗
Tungsten bronze	$Sr_{0.4}Ti_{0.2}Nb_{0.8}O_3$	✓	✗	✓	✓	?	✗	?	✓
Monoclinic S.G. C2/m	Nb_2TiO_7	✓	✗	✓	✓	✗	?	?	✗

3. CONVENTIONAL FABRICATION of SOFCs

The method used to fabricate the SOFCs is detrimental to i) the microstructure of the components and ii) the presence/absence of any undesired phases at material interfaces and interphases. Since microstructure of the SOFC components (especially the electrodes) and the chemistry of the solid/solid and solid/gas interfaces strongly impact the electrochemical performance of the SOFCs [33], the SOFC fabrication route must be carefully selected. The two most commonly preferred SOFC designs are the anode and electrolyte supported ones. The former employs a 0.5-1mm thick, porous Ni-based anode cermet as the mechanical support, a 5-50 μm-thick dense electrolyte and a 5-20 μm-thick, porous cathode. The electrolyte supported design consists of a 100-300 μm thick, dense electrolyte and 5-20 μm-thick, porous electrodes. The conventional fabrication method of both types of SOFCs relies on the sintering of powders at elevated temperatures (1200-1500 °C, depending on the component type and material chemistry). The major impact of the SOFC design is on the sequence of the sintering procedure, which, in turn, determines the maximum temperature a component must be subjected to. More specifically, the fabrication of anode supported SOFCs involves the co-sintering of anode and electrolyte layers, most frequently, both fabricated by tape casting (Figure 3.1. a). Here, the anode tape is cast from a slurry, which consists of a mixture of NiO and YSZ powders dispersed in a binder and plasticizer containing solvent [34]. The electrolyte layer is also prepared in a similar manner, the only difference being the tape casting slurry containing only YSZ powders, instead of NiO-YSZ powder mixture. The NiO-YSZ and YSZ tapes are then laminated and co-sintered at temperatures that would allow a gas-tight YSZ layer, i.e., 1350-1500 °C (Figure 3.1. a). The cathode layer is formed by the deposition of a solvent, binder and cathode powder (typically LSM and YSZ) containing ink. As the dense electrolyte is already achieved, the cathode heat treatment temperature is no longer determined by the densification temperature of YSZ and sintering can be performed at 1100-1300 °C (Figure 3.1. a).

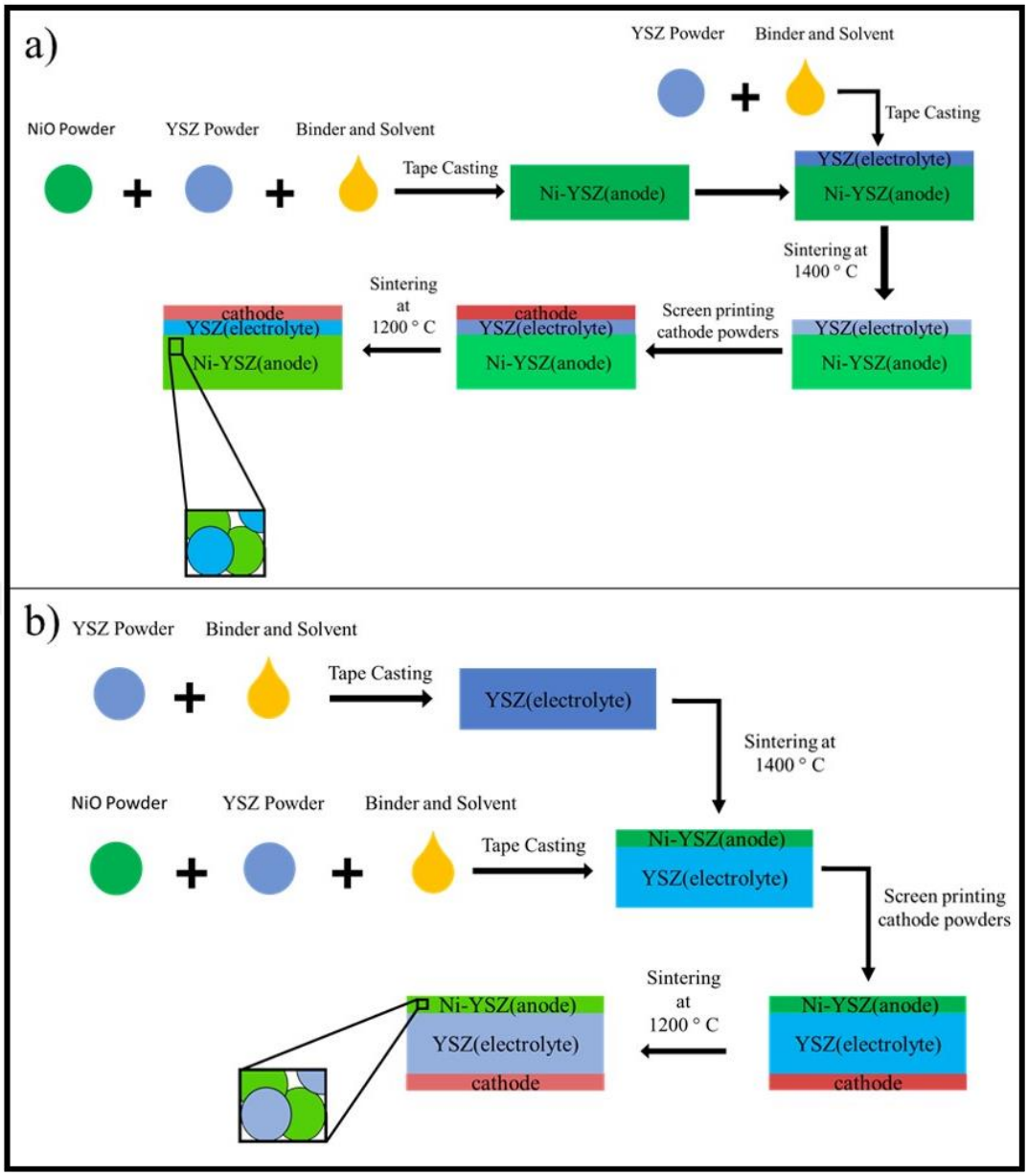

Figure 3.1: a) Conventional fabrication technique of anode supported SOFC
b) Conventional fabrication technique of electrolyte supported SOFC.

The fabrication of the electrolyte-supported SOFC involves the fabrication of the electrolyte layer first, by sintering a tape-cast YSZ layer at 1350-1500 °C (Figure 3.1.b). As a result, both the cathode and the anode layers can be fabricated by the sintering of inks containing the anode and cathode powders deposited onto the already densified electrolyte at 1200-1300 °C (Figure 3.1.b).

4. PROBLEMS RELATED TO SOFCs

The conventional SOFC system has some problems which originate from both production and operation conditions. The two main problems are i) the low initial performance and ii) performance instability upon long-term operation.

4.1. Low Performance

Among the two SOFC designs described earlier, in general, the anode-supported design provides higher performance, mainly due to the lower ohmic resistance it exhibits enabled by the thin electrolyte. Meanwhile, the high temperatures the anode/electrolyte bilayer is exposed to (1350-1500˚C) to ensure gas-tight electrolyte (Figure 3.1a) results in coarse microstructures, which corresponds to short TPBs and thus, high anode polarization resistance. For example, Sarikaya et al fabricated anode-supported SOFCs by sintering the Ni-YSZ anode/YSZ electrolyte bilayer at 1300-1400˚C [35]. The resultant microstructure had an average grain size range of ca. ~0,5 μm (Figure 4.1a) and allowed acceptable polarization resistances (ca. 0.6 $\Omega.cm^2$) only at high operating temperatures, i.e., 800 °C [35]. Even in the case of electrolyte-supported design, sintering of inks containing NiO-YSZ powder mixtures require a minimum of ca. 1200 ˚C to ensure bonding of powders to each other and to the electrolyte substrate, which still produces microstructures with micron-scale features. The microstructure of electrolyte supported cell fabricated by J.-H. Lee et al. is shown in Figure 4.1b. NiO and YSZ powders with an average diameter of ca. 2 μm were sintered at 1400˚C for 3 hours. Coarse microstructure and a consequent short triple phase boundary are evident (figure 4.1b, [36]).

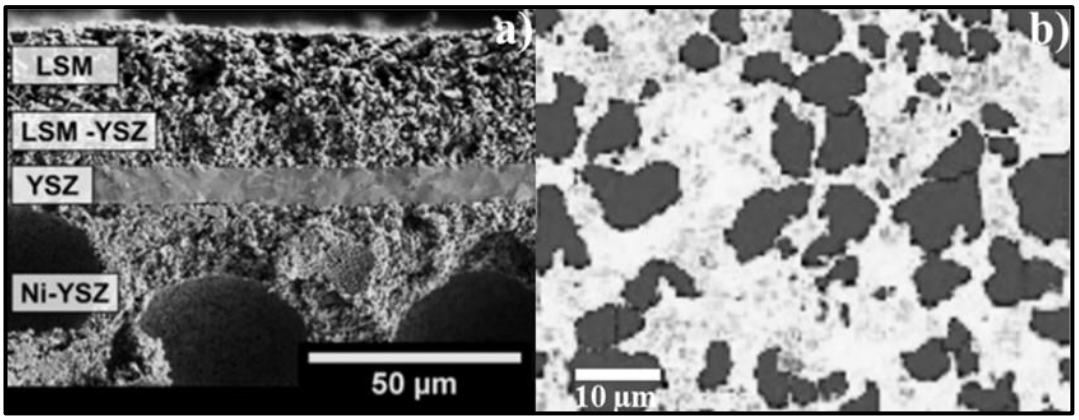

Figure 4.1: Microstructure of a) anode supported cell from cross-section
b) electrolyte supported Ni-YSZ anodes.

4.2. Long-Term Performance Degradation

Another main problem of the SOFCs is that these devices conventionally operate at high temperatures (800-1000˚C), which causes chemical and microstructural degradation. For example, it has been observed that Ni particles coarsen under the anode conditions, resulting in shortening of the triple phase boundaries and performance degradation [37]. For example, Simwonis et al investigated microstructural change and decrease in electrical conductivity in Ni-YSZ anodes. Ni particles increased 2 to 2,6 µm operation at 1000 ˚C for 4000 h [37].

Since the coarsening process is diffusion mediated, it is also thermally activated. Therefore, it may appear straightforward to address this issue by reducing the operating temperatures and thereby slow down/eliminate coarsening. However, at lower operating temperatures, electrochemical reactions at the SOFC electrodes also slow down significantly, yielding high electrode polarization resistance [3,38].

Another important issue is the ability of SOFCs to tolerate interruptions in the fuel supply. It is expected that a conventional SOFC will undergo 10-20 intentional/unintentional interruptions in the fuel supply during the targeted operation duration of 40000 hours [39]. In the absence of fuel flow, the anode compartment atmosphere becomes oxidizing, which results in the conversion of Ni into NiO [40,41]. This conversion is concomitant to an increase in volume of this phase by ca. 66-69%, resulting from the larger molar volume of NiO in comparison to Ni [42,43], and Nickels Pilling-Bedworth ratio is ca. 1,66 [44]. In conventionally prepared anodes, this expansion causes cracks in the YSZ network, as shown in figure 4.2.a, or

in some cases, a complete destruction of the anode/fuel cell [45]. Figure 4.2.b. shows schematically the microstructural changes in the Ni-YSZ anode that took place upon after 10th oxidation/reduction (redox) cycle [46].

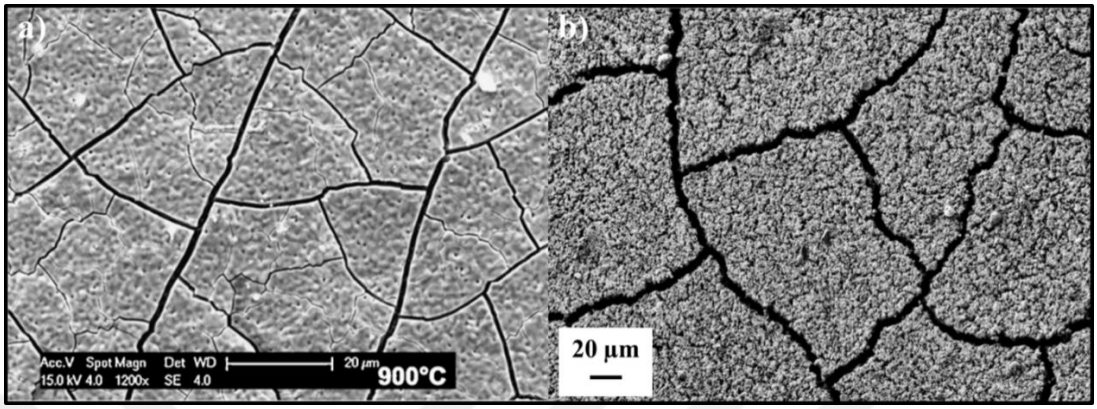

Figure 4.2: SEM images of cracks on a) the electrolyte after one redox cycle at 900˚C b) the Ni–YSZ anode after the 10th redox cycle at the same temperature.

5. SOLUTIONS OFFERED IN THE LITERATURE

Evidently, a significant portion of the SOFC issues are anode-related. Furthermore, low performance, long-term performance degradation and redox intolerance of anodes are considered to be related to i) the conventional fabrication method, which requires high heat treatment temperatures and ii) high operation temperature. For example, if a lower-temperature fabrication method is developed, a finer anode microstructure and thus lower anode polarization resistances even at lower operating temperatures (ca. 600 °C) may be achieved. In turn, operation at lower temperatures may induce long-term performance stability and redox tolerance.

One route to fabricate Ni-YSZ composite anodes has been infiltration [47]. In this technique, a liquid precursor containing Ni cations is deposited onto a porous YSZ scaffold, which is then infiltrated into the porous structure through capillary action. The Ni precursor in the scaffold is then decomposed to form solid NiO, the morphology of which depends strongly on the nature of the precursor [48]. This procedure is repeated as many times as necessary to acquire the desired amount of Ni within the porous scaffold. A schematic representation showing the infiltration-based fabrication steps is provided in Figure 5.1. This fabrication route has been considered to provide i) long triple phase boundaries due to the low heat treatment temperatures it involves and ii) redox tolerance due to the smaller amount of Ni required to achieve its percolation within the scaffold, originating from the nature of the process [47,49].

In the literature, Sarantidis et al fabricated Ni-YSZ anodes by infiltrating an aqueous Ni-nitrate solution into a porous YSZ scaffold and found that no dimensional change occurred upon redox-cycling [50]. Furthermore, Ni-YSZ anodes prepared by the infiltration of a film-forming polymeric Ni precursor into porous YSZ scaffolds has exhibited i) low polarization resistance at conventional operating conditions (ca. 0.1 $\Omega.cm^2$ at 800 °C) [47] and ii) redox tolerance [51]. On the other hand, if an aqueous Ni nitrate solution is infiltrated into porous YSZ scaffold, extremely fast performance degradation even at 650 °C was observed [52].

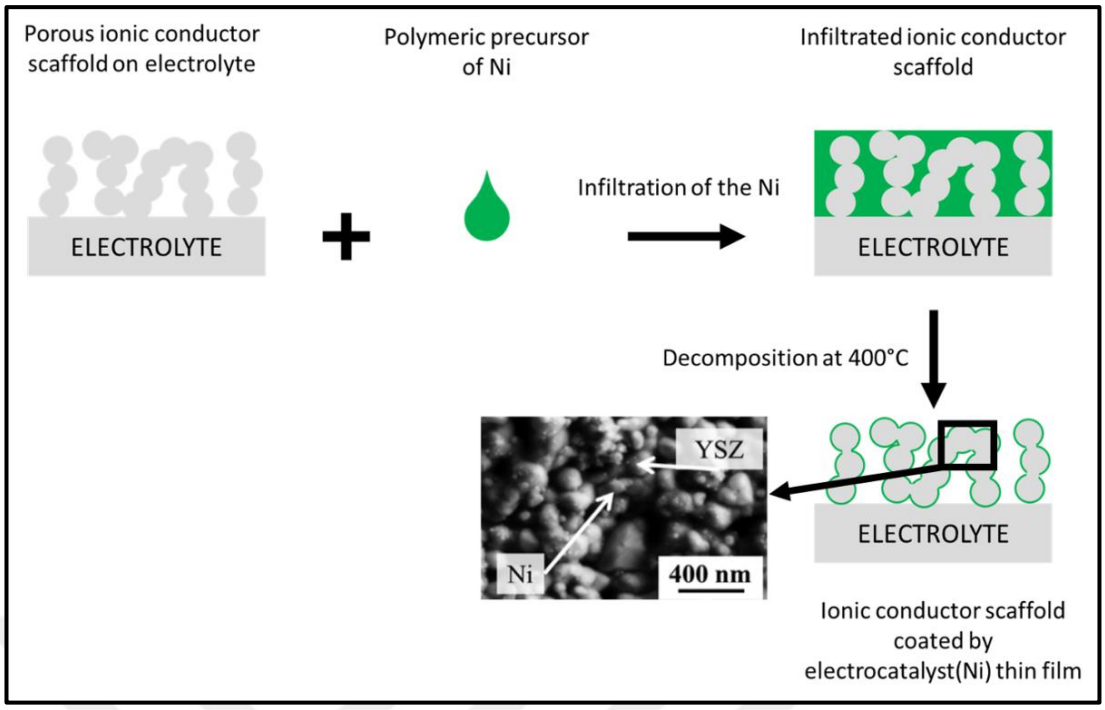

Figure 5.1: Scheme of Ni-Y SZ anode production by infiltration method.

For better SOFC performance, polarization resistance of anode should be reduced, which, in turn, requires a smaller particle size than the co-sintering and infiltration techniques offer. For this purpose, Gauckler group at ETH proposed spray pyrolysis of a solution containing Ni, Gd and Ce cations. This way a nanocomposite structure, consisting of ca 53 nm sized Ni grains was achieved after reduction at 600°C. Fast Ni coarsening evidenced by the large Ni particles forming at the outer anode surface (Figure 5.2) was observed upon reduction at 800˚C for 10 hours [53].

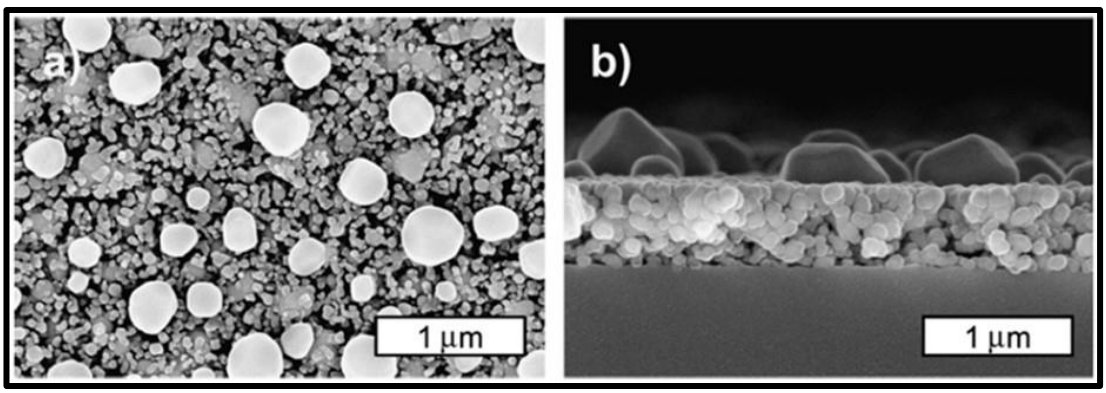

Figure 5.2: SEM of Ni-GDC anode at 800˚C after 10 hours a) surface b) cross section.

6. AIM OF THIS STUDY

The principal aim of this study is to fabricate Ni-based anodes utilizing a novel method based on liquid polymeric precursors which allows the synthesis of either powders upon calcination or thin films upon direct deposition onto a dense substrate. The method involves the use of a mixture of polymeric Ni and YSZ precursors, which are thought to yield nanocomposite powders or films upon heat treatment as a result of preferential clustering of cations. This method allows for i) molecular level mixing of the cations of electrocatalyst and ionic conductor phases and ii) low-temperature fabrication (i.e., 350-800 °C) in the case of thin film fabrication. We envision that the nanocomposite structure will produce long triple phase boundaries and thus, high electrochemical performance.

The powders synthesized by this method had to be heat treated at relatively high temperatures (1350 °C) to ensure bonding to the electrolyte. Thus, microstructures with micron-sized particles – yet with a very homogeneous Ni and YSZ distribution are expected. Naturally, these anodes are considered for conventional SOFCs operating at 700-900 °C. ,On the other hand, thin films deposited from the polymeric precursor mixtures did not require such high heat treatment temperatures – a drying step at 380 °C was sufficient to ensure good adhesion to the substrate. The lack of a high temperature heat treatment step is considered to ensure the nanoscale microstructure and low polarization resistances at lower temperatures, i.e., 600 °C after each deposition cycle were used to fabricate Ni-YSZ anodes.

In this work, we have largely focused on the microstructure – electrochemical performance relationship in thin film Ni-YSZ anodes, as well as their long-term performance stability. For general microstructural analyses, scanning electron microscopy was used routinely. We have utilized transmission electron microscopy-energy dispersive x-ray spectroscopy (TEM-EDX) analyses to be able to accurately resolve the spatial Ni, Y and Zr distribution at nanoscale. Electrochemical performance measurements were carried out by electrochemical impedance spectroscopy analyses of symmetrical half-cells.

7. EXPERIMENTAL METHODS

This thesis focuses on the fabrication of Ni-YSZ anodes via polymeric precursor method, in the form of both powders and thin films. The samples were prepared in the symmetrical half-cell configuration for both electrochemical and microstructural analysis. The symmetrical half-cell configuration consisted of a thick electrolyte with two symmetrical electrodes deposited onto its two sides (figure 7.1).

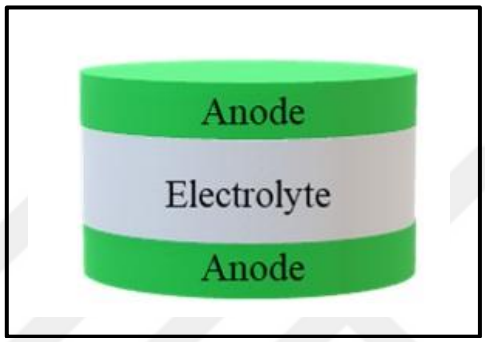

Figure 7.1: Schematic representation of symmetrical half-cell.

7.1 Fabrication of Electrolyte Substrate

Cubic structured, 8 mol% Y_2O_3 doped ZrO_2 (8YSZ) was chosen as the electrolyte, because of its desirable properties, as mentioned earlier in Section 2.1. 8YSZ electrolyte substrates were fabricated from commercial YSZ powder (TOSOH TZ-8Y). 0,7 grams of commercial YSZ powder was die-pressed into a pellet at 0,15 ton/m² pressure, using a die with a 1 cm diameter. To achieve better green strength, die-pressed pellets were subjected to cold isostatic pressure (CIP) at 200 MPa. After the CIP process pellets were sintered in stagnant air for 2 hours at 1400˚C. The photograph of the dense YSZ ceramic substrate is shown in figure 7.2.

Figure 7.2: YSZ electrolyte pellet.

7.2. Fabrication of Anode

Ni-YSZ anodes were fabricated via an ethylene glycol-based Pechini method in which separately prepared NiO and YSZ polymeric precursors were prepared separately. To obtain NiO polymeric precursor Nickel(II) nitrate hexahydrate ($Ni(NO_3).6H_2O$,Sigma-Aldrich, crystals or chunks) was first dissolved in distilled water then, ethylene glycol $(CH_2OH)_2$, Alfa Aeser, 99%) added to the solution to achieve 0.04:1 cation to ethylene glycol molar ratio. The clear solution was stirred at 80˚C until added water evaporated, and polymerization took place. The reaction that leads to polymerization shown in figure 7.3, metal nitrate powder ($Ni(NO_3).6H_2O$) dissolved in water, nitric acid (HNO_3) forms. Nitric acid oxidizes ethylene glycol and converts it into oxalic acid, which binds to the cations. Then, oxalic acid and ethylene glycol form polyester bonds, resulting in the polymeric precursor. When this polymeric precursor is coated onto a substrate in the thin film form and heat-treated, shrinkage takes place homogeneously [55].

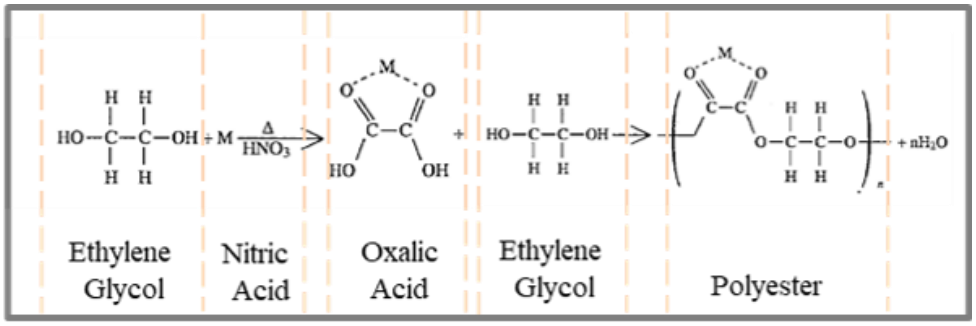

Figure 7.3: Polymerization reactions at polymeric precursor method.

The polymeric precursor of YSZ was prepared similarly. Yttrium (III) nitrate hexahydrate ($Y(NO_3)_3.6H_2O$, Alfa Aesar, 99.9%) and zirconium(IV) oxychloride octahydrate ($ZrOCl_2.8H_2O$, Sigma-Aldrich, ≥99.5%) were dissolved in distilled water to achieve an Y: Zr molar ratio of 0.16:0.84, which is the proportion of 8YSZ. Then, ethylene glycol was added to the solution to achieve a cation to ethylene glycol molar ratio of 0.02:1. The solution was stirred on a hot plate at 80˚C until the added water evaporated. To obtain composite polymeric precursor of NiO-YSZ, separately prepared NiO and YSZ solution precursors were mixed in appropriate amounts which are 60:40 volumetric ratio of Ni to YSZ. The prepared polymeric precursors can be used to either synthesize composite NiO-YSZ powders upon drying and calcination or thin films upon deposition via spin or dip coating methods (figure 7.4.). In this study, anode fabrication via both routes was investigated. Powder based anode application is similar to the conventional fabrication method, only offering a more intimately mixed electrocatalyst and ionic conductor phases, which would also yield longer TPBs than conventional anodes (Figure 7.5a). To obtain crystalline powders of NiO-YSZ polymeric precursor was dried at 120˚C and then calcined at 600, 700 or 800˚C 4 hours, in stagnant air (Figure 7.5a). Synthesized NiO-YSZ composite powders were then mixed with α-Terpineol ($C_{10}H_{18}O$, Alfa Aesar, ≥96%) and 2-Butoxyethanol ($C_6H_{14}O_2$, Sigma Aldrich) to obtain inks, which were deposited onto both surfaces of electrolyte. The deposited inks were sintered at 1350˚C for 2 hours in stagnant air to achieve bonding to powders and powder electrolyte interface (figure 7.5.a).

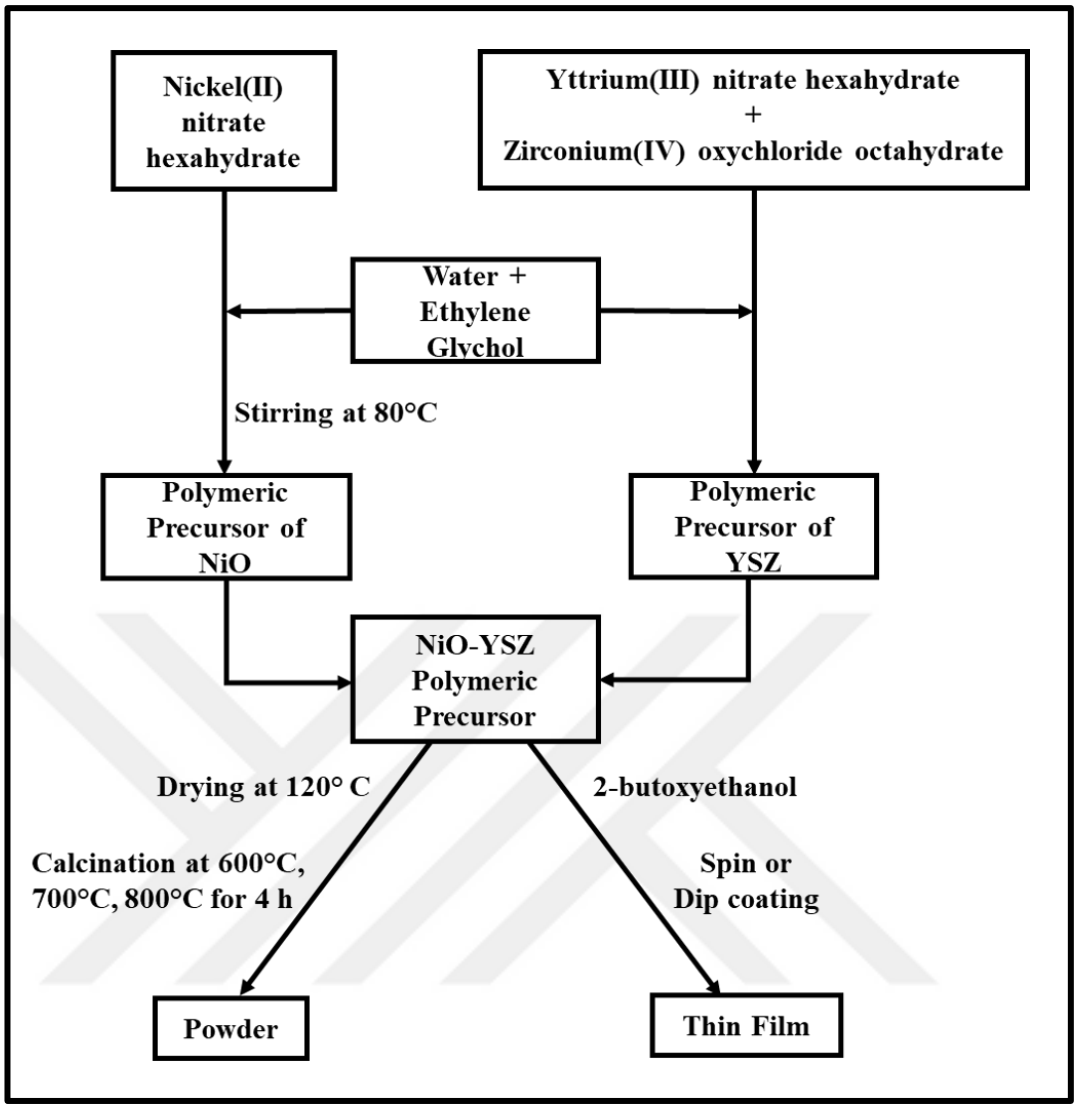

Figure 7.4: Flowchart describing NiO-YSZ polymeric precursor preparation and thin film/powder synthesis.

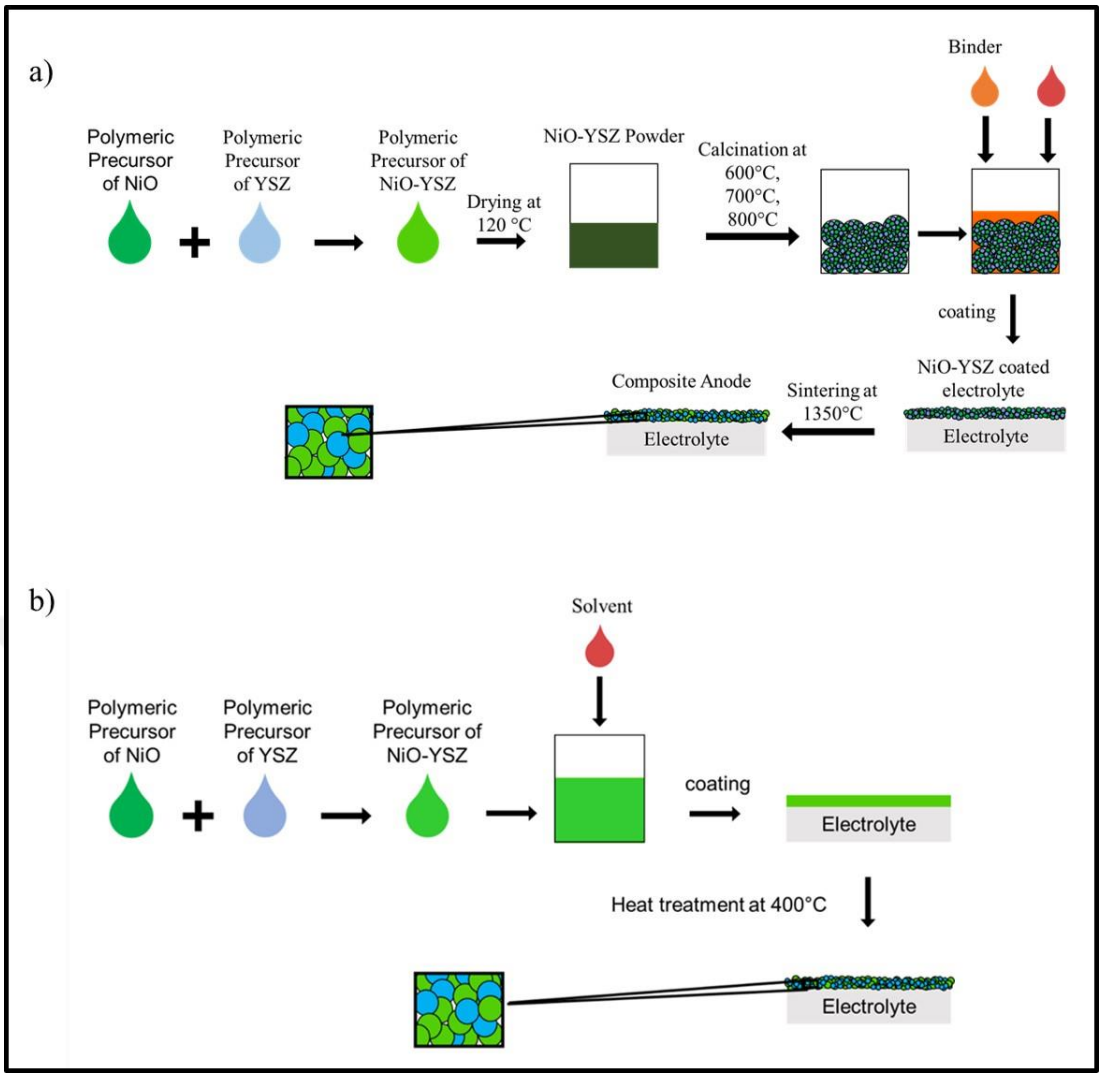

Figure 7.5: a) Fabrication of NiO-YSZ composite powders anode via ethylene glycol based Pechini method b) Fabrication of NiO-YSZ thin film anode ethylene glycol based Pechini method.

Mixtures of separately prepared NiO and YSZ solution precursors were also used to fabricate thin films, which did not require high temperature sintering to bond to the substrate and thus, were expected to have a more favorable microstructure. To reduce the surface tension of the polymeric precursor and thus obtain a homogenous coverage of the electrolyte surface 2-Butoxyethanol ($C_6H_{14}O_2$, Sigma Aldrich) was added in equal amounts to that of the precursor weight. The deposition onto the electrolyte surface was performed by spin coating at 1000-3000 rpm for 40 seconds then heat treated at 400˚C degrees. The deposition/decomposition cycle was repeated 5-20 times to achieve the required thin film thickness, the process shown in figure 7.5. b.

To demonstrate the applicability of this fabrication method to other materials, Ni-GDC anode thin films were also prepared. In this case, the polymeric precursor of GDC was prepared the same way YSZ as, i.e., gadolinium trinitrate hexahydrate ($Gd(NO_3)_3.6H_2O$, Alfa Aesar, ≥99.9%) and cerium (III) nitrate hexahydrate ($Ce(NO_3)_3.6H_2O$, Alfa Aesar, 99.5%) were dissolved in distilled water to achieve a Gd: Ce molar ratio 0.2:0.8 then ethylene glycol added and stirred at 80˚C until the water evaporated. After that, NiO and GDC polymeric precursors mixed to achieve Ni to GDC 60:40 volumetric ratio.

7.3. Characterization Techniques

7.3.1 Crystal Structure Analysis

To determine the crystal structure, x-ray diffraction (XRD) method was used. In a film-coated sample, due to the signal contribution to the XRD data from the substrate the phase determination is usually troublesome. To prevent this, phase analysis was performed using gels dried from NiO, YSZ and NiO-YSZ polymeric precursors after calcination at 600, 700 and 800˚C for 4 hours in stagnant air. XRD measurements were performed with Rigaku D-Max 2200 and Bruker D8 Advance devices using Cu Kα radiation source. The data was collected between 2θ=10-80˚ with a scan rate of 2˚ per minute.

To determine the effect of mixing polymeric NiO and YSZ precursors on the crystallization behaviour of these two phases; the average crystallite sizes of calcined NiO, YSZ and NiO-YSZ gels were calculated using Scherrer equation (equation 7.1).

$$D_p = \frac{0.9\lambda}{B\cos\theta} \tag{7.1}$$

Here, λ is x-ray wavelength which is 1.54 Å, θ is the diffraction angle and B is the full width at half maximum intensity and Dp is the average crystallite size.

7.3.2. Particle Size Distribution Analysis

Particle size distribution was measured by laser diffraction method by Malvern Mastersizer 2000. The dried gel of NiO-YSZ polymeric precursors calcined at 600-800˚C for 4 hours in stagnant air then that powders were used.

7.3.3. Thermal Analysis

Differential thermal analysis (DTA) and thermogravimetric analysis (TG) were used to determine the temperatures for decomposition, crystallization and phase transformation of the dried gels. These thermal analyses were performed at 25-1000 °C at a scan rate of 10 °C/min with Netzsch STA 449 F3, differential thermal analysis device.

7.3.4. Stability of the Polymeric Precursors

To fabricate thin film anodes, polymeric precursor solutions need to remain stable, i.e., not undergo precipitation, further gelation etc., with time for homogeneous coating. To test the polymeric precursor stability with time, changes in the viscosity was measured with time using Vibro Viscometer SV-10 (A&D Company, Limited, Japan). Temperature fluctuations were also recorded for an accurate analysis.

7.3.5. Microstructural Analysis

To examine the phase distribution microstructural analysis of carried out with scanning electron microscopy (SEM) by Philips XL 30 SFEG and transmission electron microscopy (TEM) by TEM-EDS Jeol Arm 200F. For the powder based symmetrical half cells, images were collected from cross-section and top surfaces on samples after electrochemical tests performed. To collect electrons conductive surface wanted for that reason surface of the samples coated with gold for 15 seconds. For the thin film based symmetrical half cells and fuel cells images were collected before and the after long term electrochemical tests. With that before and

after long term comparison test aim was determining if there is structural deterioration occurs or not.

7.3.6. Electrochemical Analysis

Electrical resistance is the ability to resist electrical current flow in an electrical circuit, basically, determine by Ohm's Law which is shown in equation 7.2. Ohm's Law defines resistance (R) as the ratio of voltage (E) to current (I). This law is acceptable for an ideal resistor assumption. There are three main assumptions, Ohm's Law is valid for all voltage and current flow levels, resistance independent of frequency, voltage and alternative current (AC) signals are in phase.

$$R \equiv {}^{E}/_{I} \tag{7.2}$$

Impedance is the ability to resist electrical current flow without assumptions. Electrochemical resistance measured by applying AC potential to a cell which is also symmetrical half cell in our study, response sinusoidal voltage and sinusoidal current. The applied and responded sinusoidal voltage is shown in equation 7.3.

$$E_t = E_0 \, sin(\omega t) \tag{7.3}$$

As can be seen in equation 7.3 it is function of time. E_0 is applied AC voltage, E_t is potential at the $\boldsymbol{t}$ time and ω is frequency as radial. Relation between frequency f (Hertz) and radial frequency ω (rad/sec) shown in equation 7.4.

$$\omega = 2\pi f \tag{7.4}$$

Responded current (I_t) to applied AC voltage is shown in equation 7.5, $\emptyset$ is the phase shift.

$$I_t = I_0 \, sin(\omega t + \emptyset) \tag{7.5}$$

If we expressed impedance as Ohm's Law form, potential (E_t) is derived by current (I_t) shown in equation 7.6 as a function of amplitude (Z_0) and phase shift ($\emptyset$).

$$Z = \frac{E_t}{I_t} = \frac{E_0 \sin(wt)}{I_0 \sin(wt+\emptyset)} = Z_0 \tag{7.6}$$

When a graph plotted E_t as a x-axis and I_t as y-axis Lissajous curve seen and impedance can be expressed with Euler's relation which is shown equation 7.7.

$$\exp(j\emptyset) = cos\emptyset + jsin\emptyset \tag{7.7}$$

As a complex function potential and current response shown in equation 7.8 and 7.9.

$$E_t = E_0\, exp(j\omega t) \tag{7.8}$$

$$I_t = I_0\, exp(j\omega t - \emptyset) \tag{7.9}$$

Impedance is a complex equation shown in equation 7.10, j is the imaginary unit, the real component is $Z_{real} = Z_0 cos\emptyset$ and imaginary component is $Z_{imag} = Z_0 sin\emptyset$. In this study Nyquist and Bode plots used for analysis the eis data. Sample of Nyquist plot shown in figure 7.6, the x-axis is shows Zreal (Z') and the y-axis is showing Zimag (Z''). Bode plot has a frequency in x-axis and Zimag in y-axis so that graph gives frequency data information.

$$Z(\omega) = \frac{E}{I} = Z_0 exp(j\emptyset) = Z_0(cos\emptyset + jsin\emptyset) \tag{7.10}$$

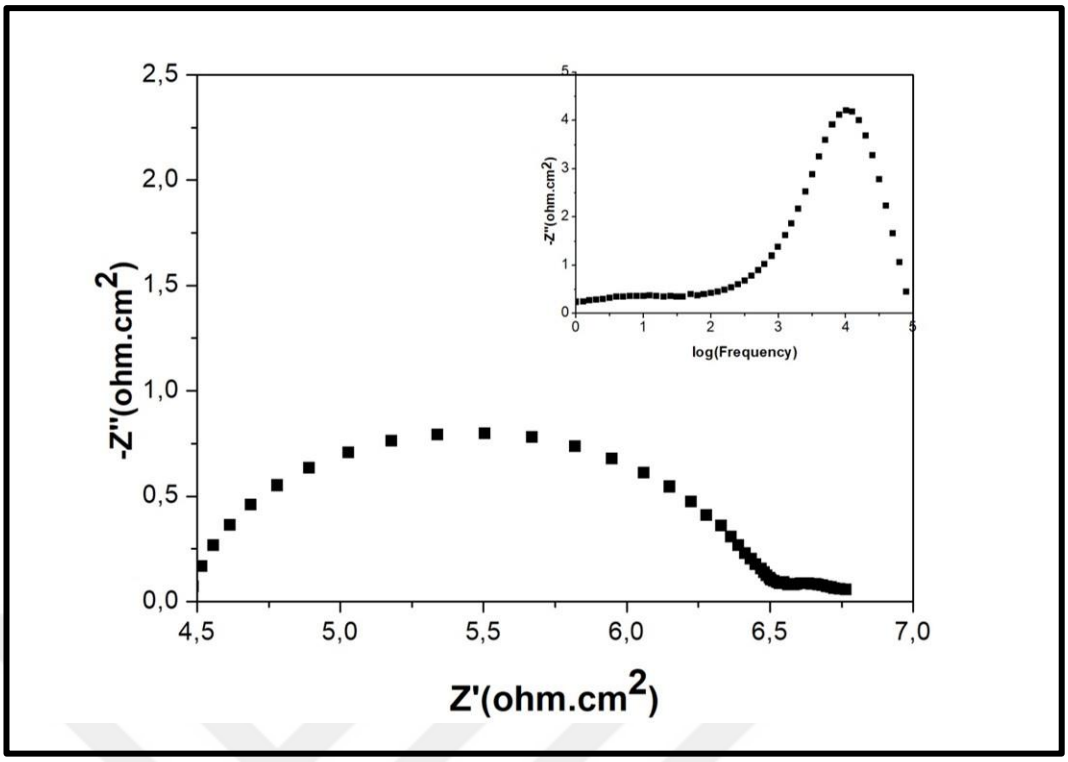

Figure 7.6: Nyquist and inset Bode plot sample.

For the EIS measurements in this study, Ni or Ag was used as a current collector. These current collectors were deposited onto the electrodes in the form of inks prepared by mixing Ni (II) oxide powder (Alfa-Aesar, 99%), α-Terpineol (Alfa-Aesar, ≥96%) and 2-Butoxyethanol (Sigma-Aldrich). Electrical contacts were made by attaching Nickel wires (Alfa-Aesar, 0.25 mm diameter, 99.98%) onto the electrodes using Ceramabond adhesive, the scheme shown in Figure 7.7.

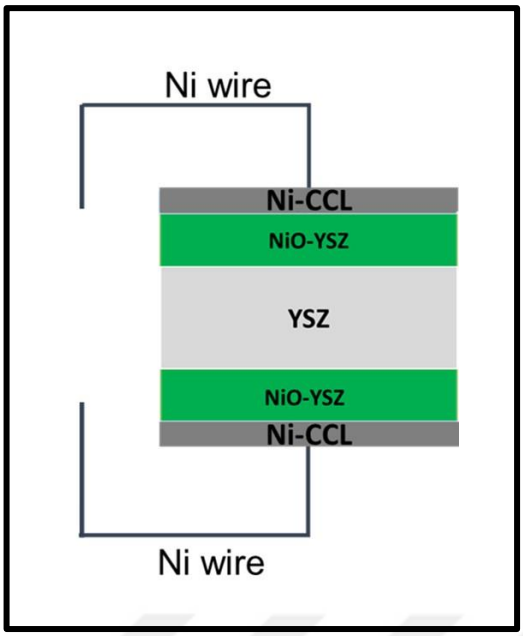

Figure 7.7: Symmetrical half cell preparation for electrochemical impedance spectroscopy test.

After symmetrical half-cell measurements, the EIS data was multiplied by the contact area for normalization and thus, area-specific resistance (ASR) was obtained Nyquist plot in figure 7.8 show the two type ASR. ASR1 caused by electrolyte is called ohmic resistance or series resistance (Rs). ASR2 is caused by electrode resistance which is anode, because of the symmetrical cell design we measure 2 symmetric anode resistance so multiplication to 2 the ASR2 value gives an $ASR_{anode.}$

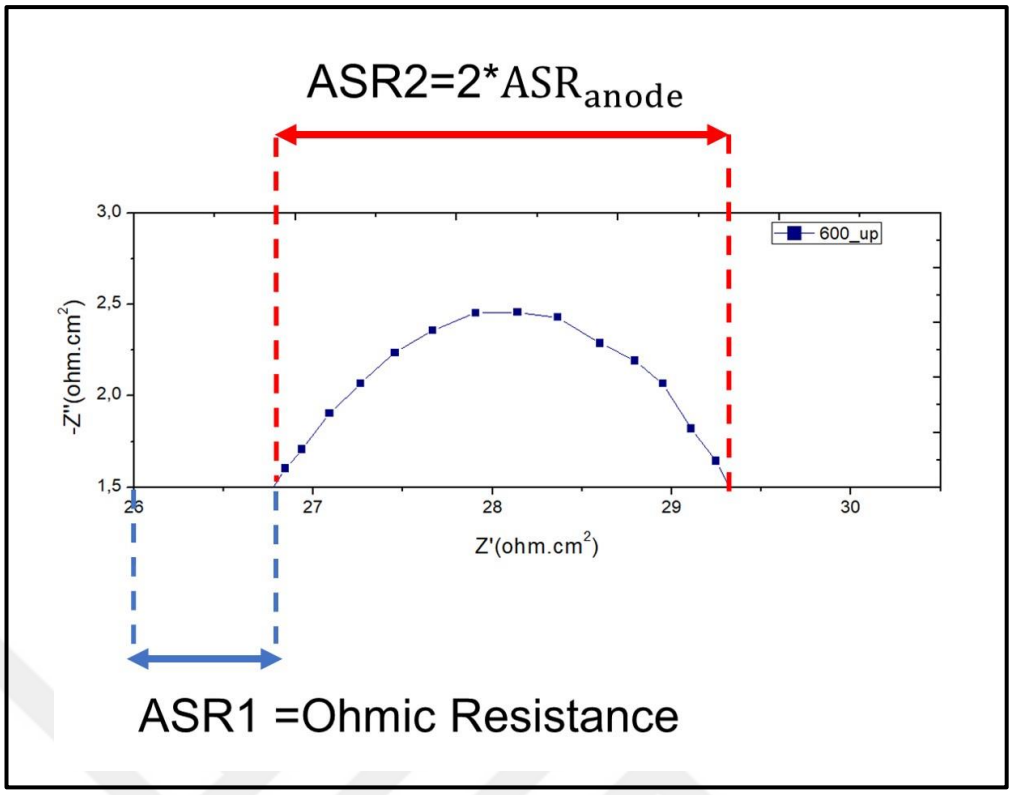

Figure 7.8: Naming the resistance types in symmetrical half cell Nyquist plot.

For the electrochemical analysis, electrochemical impedance spectroscopy (EIS) measurements were performed in %10 H_2 - %90 Ar atmosphere by Gamry Potentiostat Reference 3000 device. EIS measurements were performed between 500-600°C for thin film based samples and 500-750°C for powder based samples, in stagnant air at the 5×10^{-2} - 10^5 Hz frequency range, using ±10 mV excitation voltage. Sample holder and test system is shown in figure 7.9.

Figure 7.9: a) A sample prepared for electrochemical characterization connected to sample holder b) Electrochemical characterization test system.

8. RESULTS AND DISCUSSION

Using mixtures of polymeric electrocatalyst (Ni) and ionic conductor (YSZ) precursors, both composite powders and thin films produced. Figure 8.1 shows schematically the processing routes that lead to powder-based or thin film anodes using a mixture of polymeric precursors. To synthesize composite NiO-YSZ powders, the mixture of polymeric NiO and YSZ precursor solutions were dried, gelled and calcined at 600-800 °C. To form the anode layers, the synthesized powders had to be dispersed in an ink, deposited onto the previously sintered YSZ substrate and sintered at 1350 °C to allow for powder-powder and powder-electrolyte bonding.

To fabricate composite thin films, polymeric precursor mixtures were mixed with a surfactant to reduce their surface tension and deposited onto the YSZ electrolyte substrate via spin coating. In this case, the films could be formed on the electrolytes upon heating the samples to 380 °C to ensure the decomposition of the deposited precursor and much lower heat treatment temperatures in comparison to the powder method (i.e., up to 800 °C) were required to achieve desired electrochemical performance. Thus, better electrochemical performance is expected in the thin film electrodes.

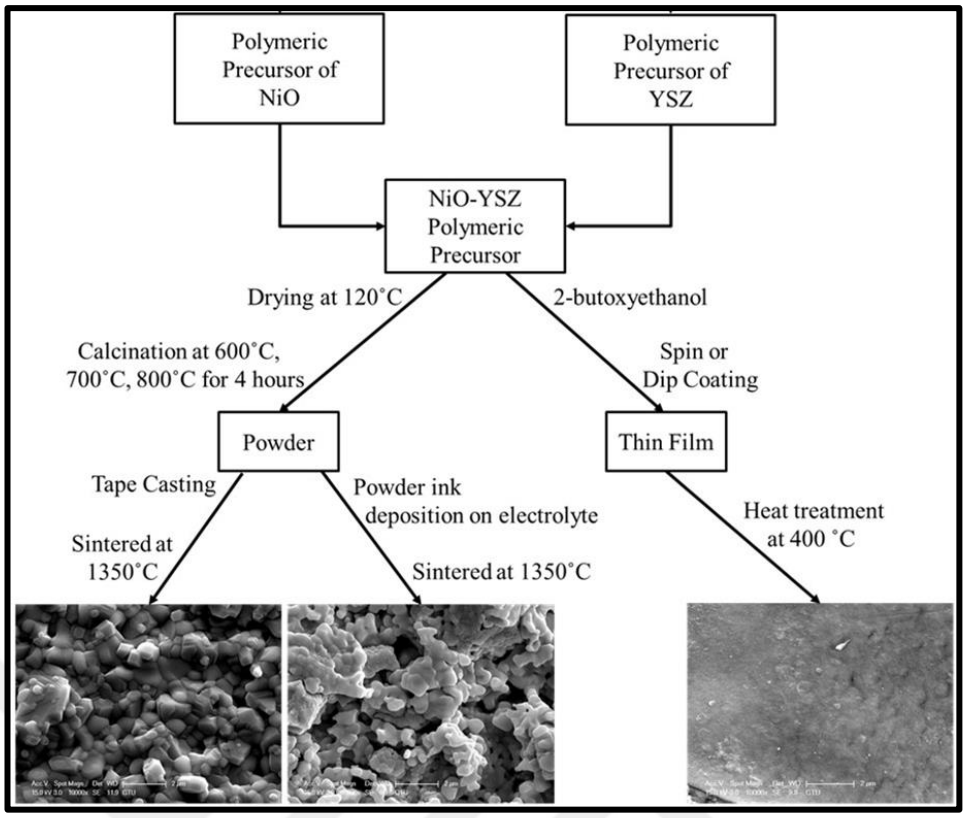

Figure 8.1: Comparison of microstructures obtained from polymeric precursor-derived powders/thin films.

8.1. Properties of The Polymeric Precursors

8.1.1. Stability of The Polymeric Precursors

[2] Bilbey B., Sezen M., Ow-Yang C., Buyukaksoy A., "Addressing the Performance Degradation Issue in Nanoscaled Ni-YSZ Anodes in Solid Oxide Fuel Cells", Electroceramics XVII (August 2020), Darmstadt/Germany.

[3] Bilbey B., Sezen M., Ow-Yang C., Buyukaksoy A., "Influence of Processing Conditions on the Electrochemical Performance of Ni-YSZ Thin Film Anodes Prepared by Polymeric Precursor Deposition", mESC-IS 2019, 4th International Symposium on Materials for Energy Storage and Conversion, Muğla, Turkey.

Different polymeric precursor properties are required for the powder synthesis and thin film fabrication. For example, a clear solution that is precipitate-free is required for both routes, to avoid chemical inhomogeneity. Meanwhile, for a polymeric precursor to be useful for thin film deposition, it has to have low enough viscosity to be spread over the substrate surface during spin coating and low enough

surface tension is required for effective surface coverage. While the latter is ensured by the addition of the surfactant 2-butoxyethanol to the mixture of polymeric precursors (see an experimental section for details), the former has to be investigated.

Here, the stability of the viscosities of the NiO, YSZ and NiO-YSZ polymeric precursors were measured intermittently over 300-hours period (Figure 8.2). Changes in the temperature were also tracked to correct viscosity fluctuations (Figure 8.2). Photographs of the polymeric precursors before and after the experiments are also provided in the insets (Figure 8.2). The viscosity of the as-prepared NiO precursor was 22.2 mPa.s and 24.1 mPa.s 405 hours later (Figure 8.2.a). The viscosity of the YSZ precursor also remained quite stable under laboratory conditions in the 29.7-34.1 mPa.s range (Figure 8.2b). In contrast, the NiO-YSZ precursor viscosity increased from 8.71 to 35.10 mPa.s after 387 hours (Figure 8.2c). The increase in viscosity along with the decay in the clarity of the solution (Figure 8.2c), suggests that the NiO-YSZ precursor underwent gelation and precipitation, which renders it unfit for use in thin film deposition. Therefore, for thin film deposition, NiO-YSZ precursors were used as soon as they were prepared, whereas NiO and YSZ precursors had a relatively long shelf-life.

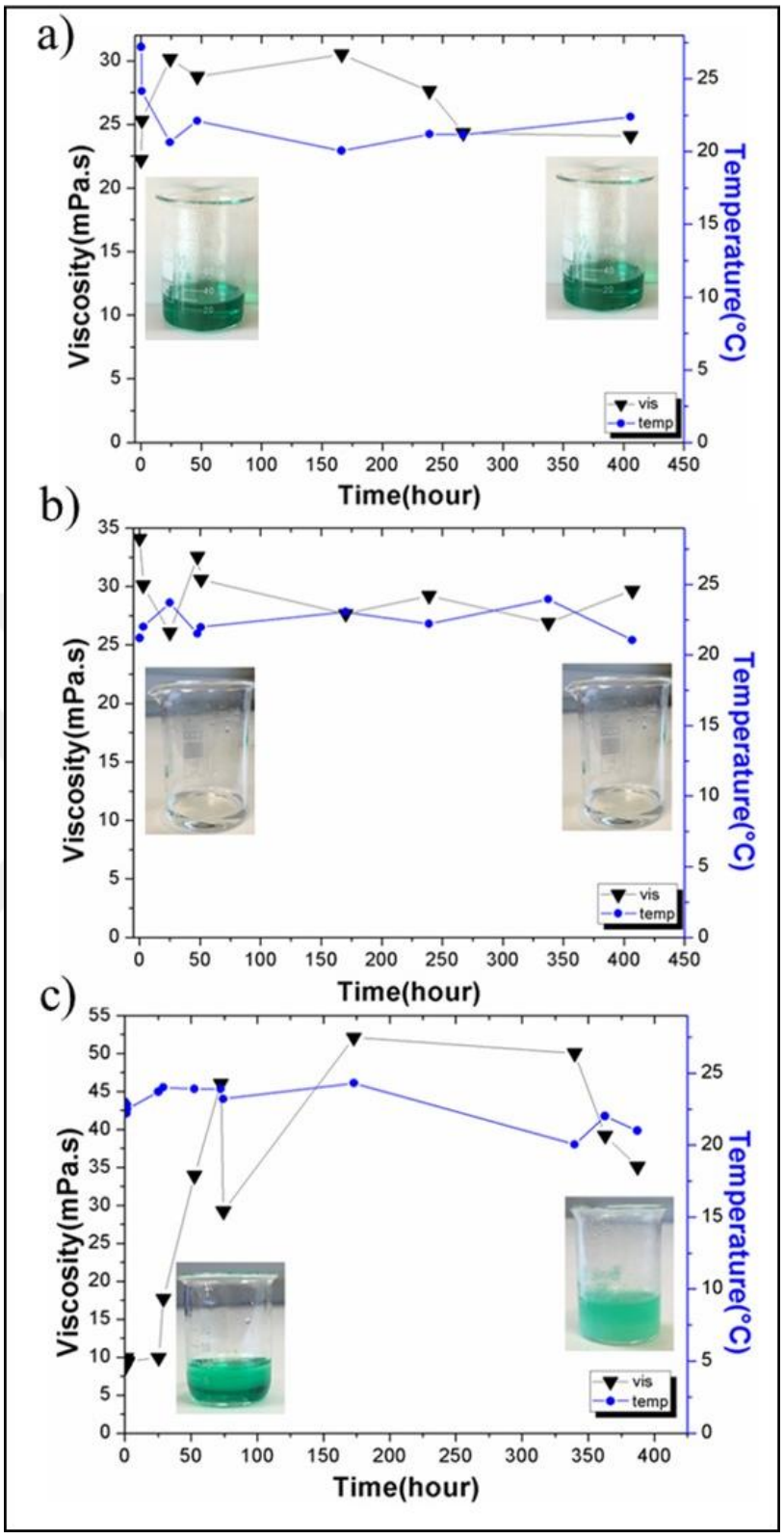

Figure 8.2: Changes in the viscosities of polymeric a) NiO, b) YSZ, and c) NiO-YSZ precursors with time. Changes in the solution temperature as well as solution photographs before and after long-term measurement are also shown.

8.1.2. Thermal Decomposition Behaviour

Differential thermal and thermogravimetric analysis used to determine the crystallization behaviours of gels derived from the NiO, YSZ and NiO-YSZ polymeric precursors by drying at 120˚C. Figure 8.3a shows the DTA/TGA analysis of NiO powders derived from the polymeric precursor. Endothermic peaks were observed at 220, 420-465 and 745˚C, while the exothermic peaks were at 175, 325, 358 and 775˚C. Ethylene glycol gives endothermic peaks around 200˚C, that which is the boiling temperature of EG (197˚C). [59] DTA-TGA of YSZ was given endothermic peaks at 210 and 360˚C and exothermic two exothermic peaks observed 540 and a wider one between 620-970˚C shown in figure 8.3.b. In the composite NiO-YSZ powders DTA-TGA analysis exothermic peaks observed at 155, 365 and 485˚C and endothermic peaks observed at ca. 200, 400˚C and after the last exothermic peak 3 steep endothermic peaks observed from the figure 8.3.c.

Ch. Laberty-Robert et al. synthesized 8YSZ by Pechini method in citric acid (CA) and ethylene glycol with 5 to 0.6 CA/EG ratios. From the DTA-TGA an endothermic peak observed at low temperature (100-200˚C) and exothermic peaks observed with several steps at 168 and 300˚C. [60] In figure 8.3b also two exothermic peaks observed but at the different temperatures, CA could be responsible that difference because the melting and boiling temperatures are 153 and 310˚C of CA thus decomposes between that temperatures. In the study of S. Li et al. Ni-YSZ produced from the $ZrOCl_2.8H_2O$, Y_2O_3 and $NiCl_2.6H2O$ powders were dissolved in water together by coprecipitation method with NaOH, $NH_3.H_2O$ and $NH_3.H_2O$-NH_4HCO_3 solutions. DTA curves for 40 volume % Ni-YSZ resulted in an endothermic peak at 299˚C and exothermic peak at 548˚C. [61] H. Mohebbi et al. synthesized NiO-YSZ by microwave-assisted combustion method, DTA/TGA measured between 50-250˚C. Precursor solutions prepared at different pH values 0.5 to 9, the width of the exothermic peaks increased with increasing pH values thus decomposition and combustion affected by pH. [56] In the study of T. Razpotnik, J. Macek NiO-YSZ powders synthesized by Pechini Method using ethylene glycol (EG) with ascorbic acid (AA) and citric acid (CA) as chelating agents. DTA/TGA analysis for the CA/EG sample endothermic peak observed at 200˚C caused by dehydration of gel and evaporation of EG also for both samples prepared with CA/EG and AA/EG exothermic peaks observed from 200 to 700˚C because of the

combustion of the polymeric gels.[57] F.-Y. Shih et al. synthesized NiO-8YSZ powders by succinic acid combustion method endothermic peaks observed at 102 and 171˚C, and exothermic peaks observed at 245 and 302˚C. [62] In the study of C. Suciu et al. to obtain NiO-YSZ particles, salts dissolved in water and synthesis with sucrose and pectin. An endothermic peak observed between 100-200˚C which was caused by water loss and three exothermic peaks observed at between 200-400˚C as an effect of decomposition by organics, 400-475˚C and 475-800˚C caused by the formation of ZrO_2, NiO. [63] In the study of the M.-J. Lee et al. core-shell structured Ni-8YSZ powders synthesized by hydrothermal technique with cationic surfactant cetyltrimeyhyl ammonium bromide (CTAB) used to form produce Ni core and YSZ shell. Two exothermic peaks observed from the DTA analysis a small at 250˚C caused by melting CTAB (254˚C) and a strong one at 500˚C which was the result of oxidation of Ni core particles. From the TGA weight decrease observed until 350˚C and increased steeply at 400˚C that weight changes caused by the decomposition of CTAB in low temperature and NiO formation from 400 to 600˚C. [64]

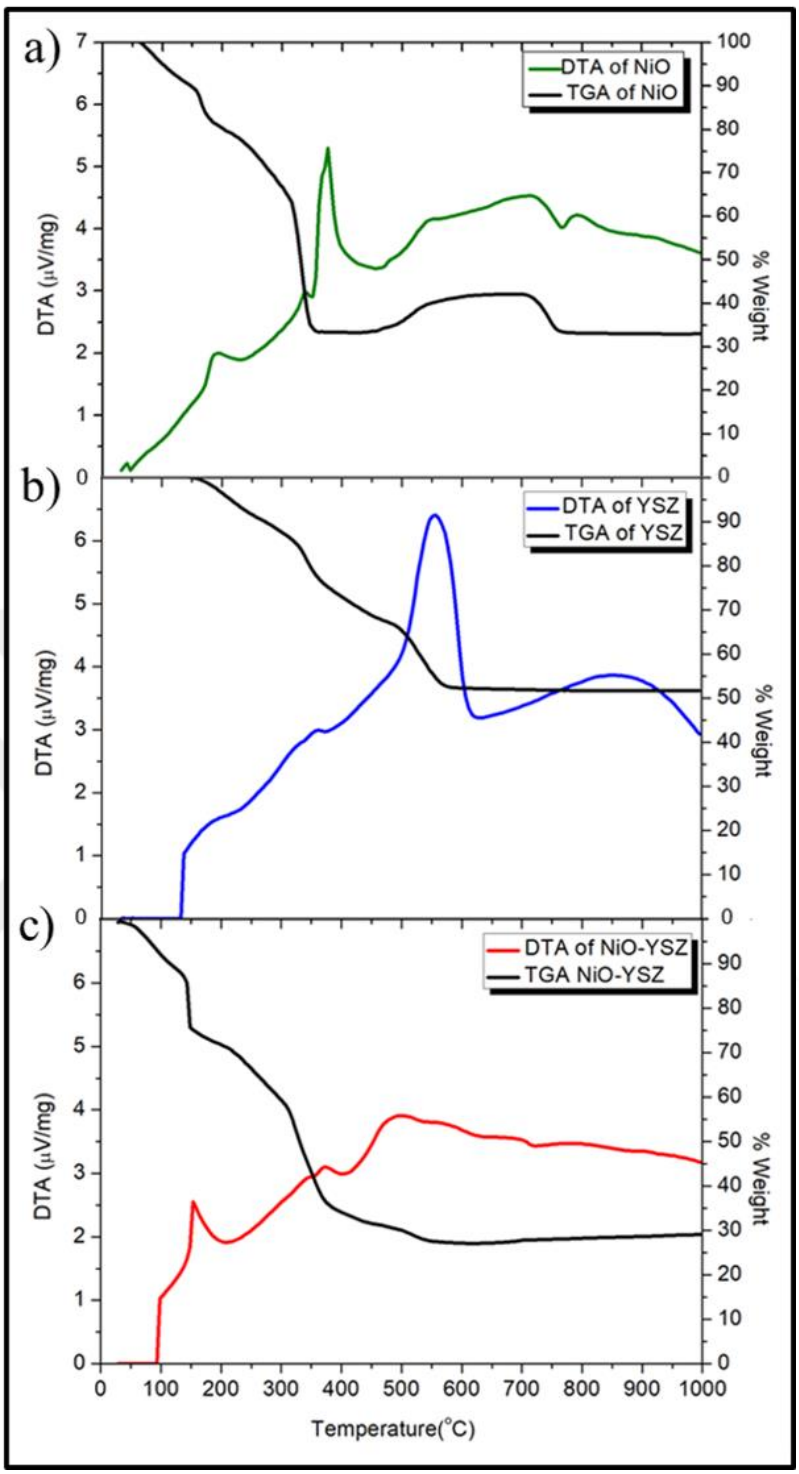

Figure 8.3: DTA/TGA analysis of a) NiO b) YSZ c) NiO-YSZ.

8.1.3. Phase Evolution of Gels Upon Calcination

To determine the phase evolution of NiO-YSZ composite powders, first, the crystal structures of gels dried from separate polymeric NiO and YSZ precursors after calcination at 600, 700 and 800°C for 4 hours were determined by x-ray diffraction (XRD). Peaks belonging to cubic NiO (PDF: 03-065-5745) as well as metallic Ni phase (also cubic in structure, PDF:00-004-0850) were observed, after calcination at 600°C (Figure 8.4a). With increasing calcination temperature, metallic Ni transformed into cubic NiO (Figure 8.4a). Cubic YSZ phase (PDF: 00-030-1468) was obtained at all calcination temperatures (Figure 8.4b). The peak widths decreased with increasing calcination temperature, indicative of increasing crystal size (Figure 8.4b). The XRD patterns obtained from a mixture of polymeric NiO and YSZ precursors showed that cubic NiO and YSZ phases crystallized separately and no solid solution formation took place, regardless the calcination temperature (Figure 8.4c). The YSZ peaks typically had wider peaks in comparison to those that belonged to NiO (Figure 8.4b).

To determine the effect of mixing the polymeric NiO and YSZ precursors on the crystallization behaviour of the respective phases, the average crystallite sizes of NiO and YSZ phases were calculated from XRD patterns using the Scherrer equation (Equation 7.1),

$$D_p = \frac{0.9\lambda}{B\cos\theta} \tag{7.1}$$

where λ is x-ray wavelength, θ is the diffraction angle and B is the full width at half maximum intensity and Dp is the average crystallite size.

Figure 8.5 shows the changes in the crystallite sizes of NiO and YSZ phases with increasing calcination temperature, in the cases of separate and mixed polymeric precursors. The crystallite size of NiO and YSZ phases increased with increasing calcination temperatures in both separate and mixed precursor solution cases (Figure 8.5). The crystallite size of the NiO phase was significantly smaller in the mixed precursor solution case in comparison to single precursor derived NiO (Figure 8.5). Evidently, the presence of Zr4+ and Y3+ ions in the solution hindered the clustering of Ni2+, thereby resulting in smaller NiO crystals in comparison to

those obtained from a separate NiO precursor. The inhibition of long-range order NiO crystal formation by the addition of Zr4+ and Y3+ ions to the solution suggests the formation of a nanocomposite powder. On the other hand, no significant effect of polymeric NiO precursor addition on the YSZ phase evolution was determined within the measurement accuracy of our equipment (figure 8.5). Overall, NiO-YSZ composite powders with average NiO and YSZ crystal sizes in the ranges of 26-37 and 7 - 11 nm, respectively, were obtained using a mixture of polymeric NiO and YSZ precursors upon calcination at 600-800 °C.

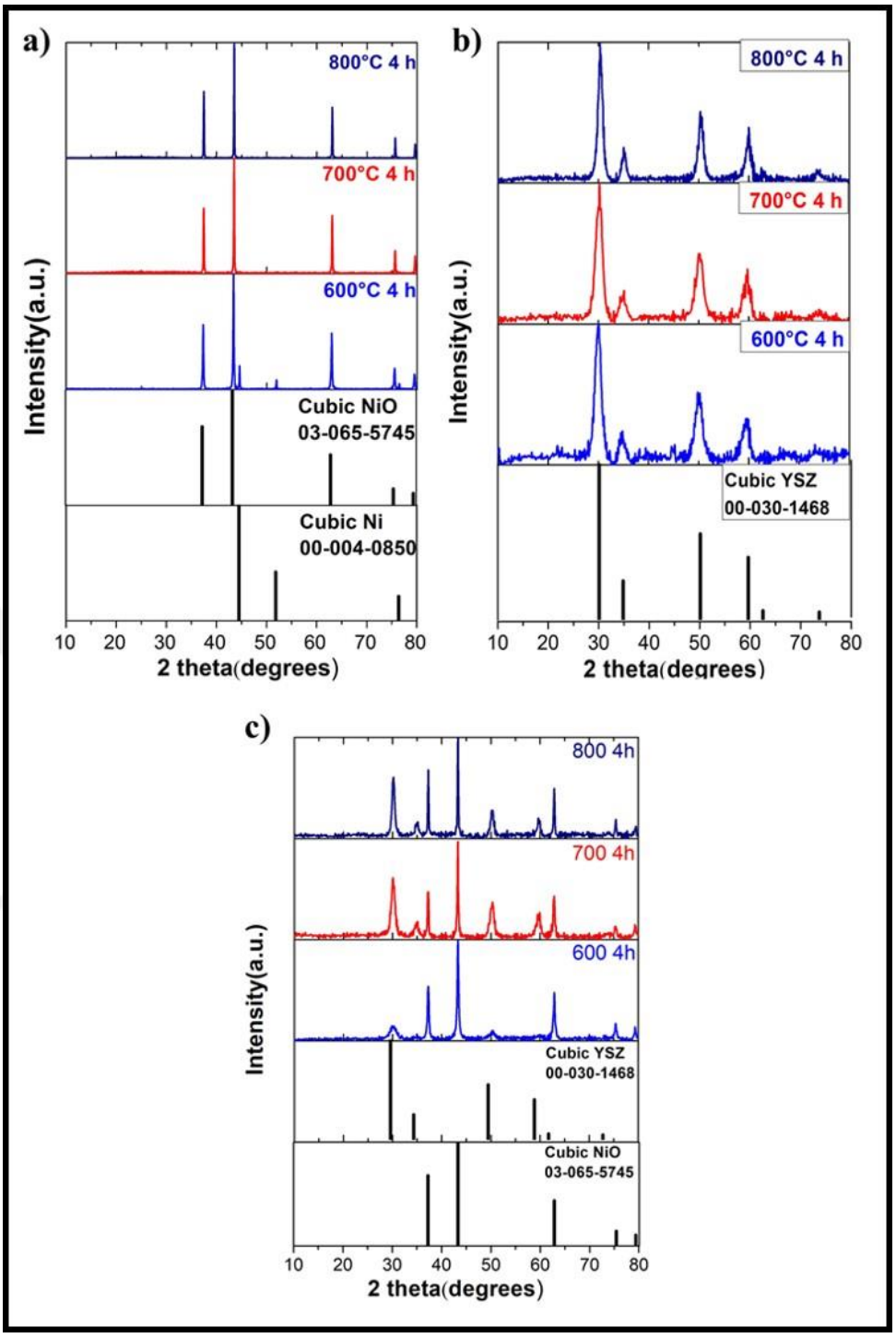

Figure 8.4: X-ray diffraction patterns obtained from gels dried from a) NiO, b) YSZ and c) NiO-YSZ polymeric precursors, calcined at 600, 700 and 800 °C.

NiO-YSZ powders synthesized by microwave-assisted combustion reported having average crystal sizes ranging from 8 to 33 nm and from 14 to 32 nm for NiO and YSZ respectively, depending on the pH from of the solution [56]. On the other hand, Razpotnik et al. reported that average crystal sizes of NiO and YSZ varied between 42 to 48 nm and 6 to 15 nm, respectively, when a Pechini method, similar to

the one adopted in the present study, was used [57]. However, the NiO and YSZ crystal sizes reported here for the Pechini-derived composite powders are somewhat smaller than those reported in Refs 56 and 57 suggesting a more intimate mixing and thus, potentially longer triple phase boundaries.

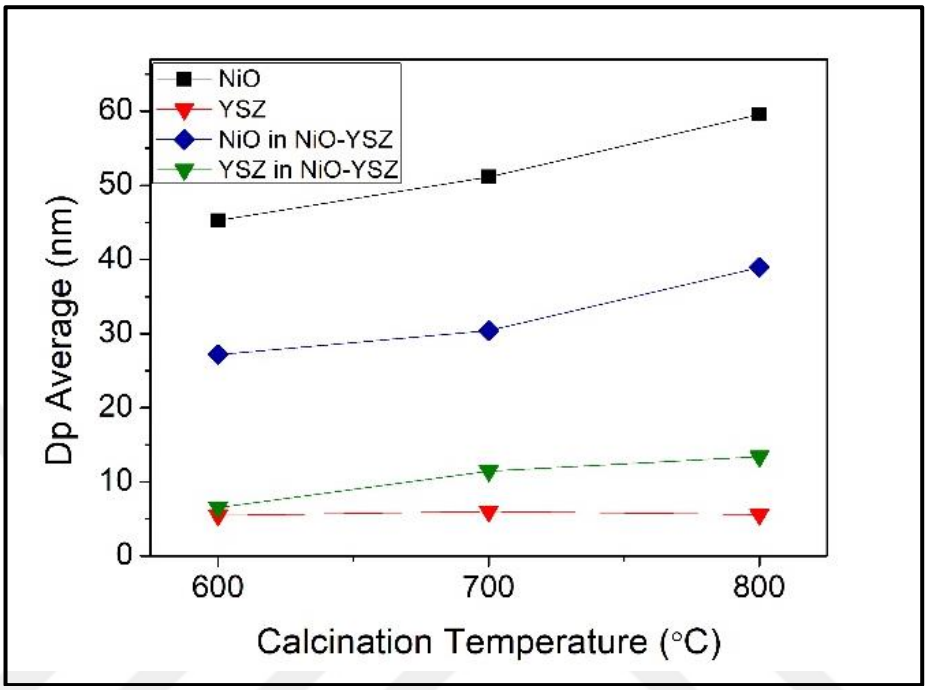

Figure 8.5: Average crystallite size of NiO and YSZ phases in NiO, YSZ and NiO-YSZ powders as a function of calcination temperature.

8.2. Ni-YSZ Anodes from Composite Powders Prepared from Polymeric Precursors

8.2.1. Particle Size

Another important characteristic of the synthesized powders that may be detrimental to the electrochemical activity is the particle size distribution. Laser diffraction measurements revealed that the amount of submicron-sized particles decreased with increasing calcination temperature (Figure 8.6a). The average particle size of NiO-YSZ powders was 897 ±31, 1073 ±16 and 1313 ±19 nm at 600, 700 and 800 °C, respectively (Figure 8.6b), which is significantly smaller than the particle size values reported for the Pechini-derived NiO-YSZ powders reported in the literature (average particle size 8.6-14.9 μm in REF-57). Particle sizes somewhat

smaller than those reported in the present work have been achieved by Han et al. (0.4 – 0.7 μm), who mixed a NiO precursor solution with fine, commercial YSZ powder [58] to achieve NiO-YSZ composite powders. Overall, the relatively small crystallite and particle sizes were obtained in this present study via Pechini process. Thus, favourable microstructure upon sintering and thus, the promising electrochemical activity can be expected.

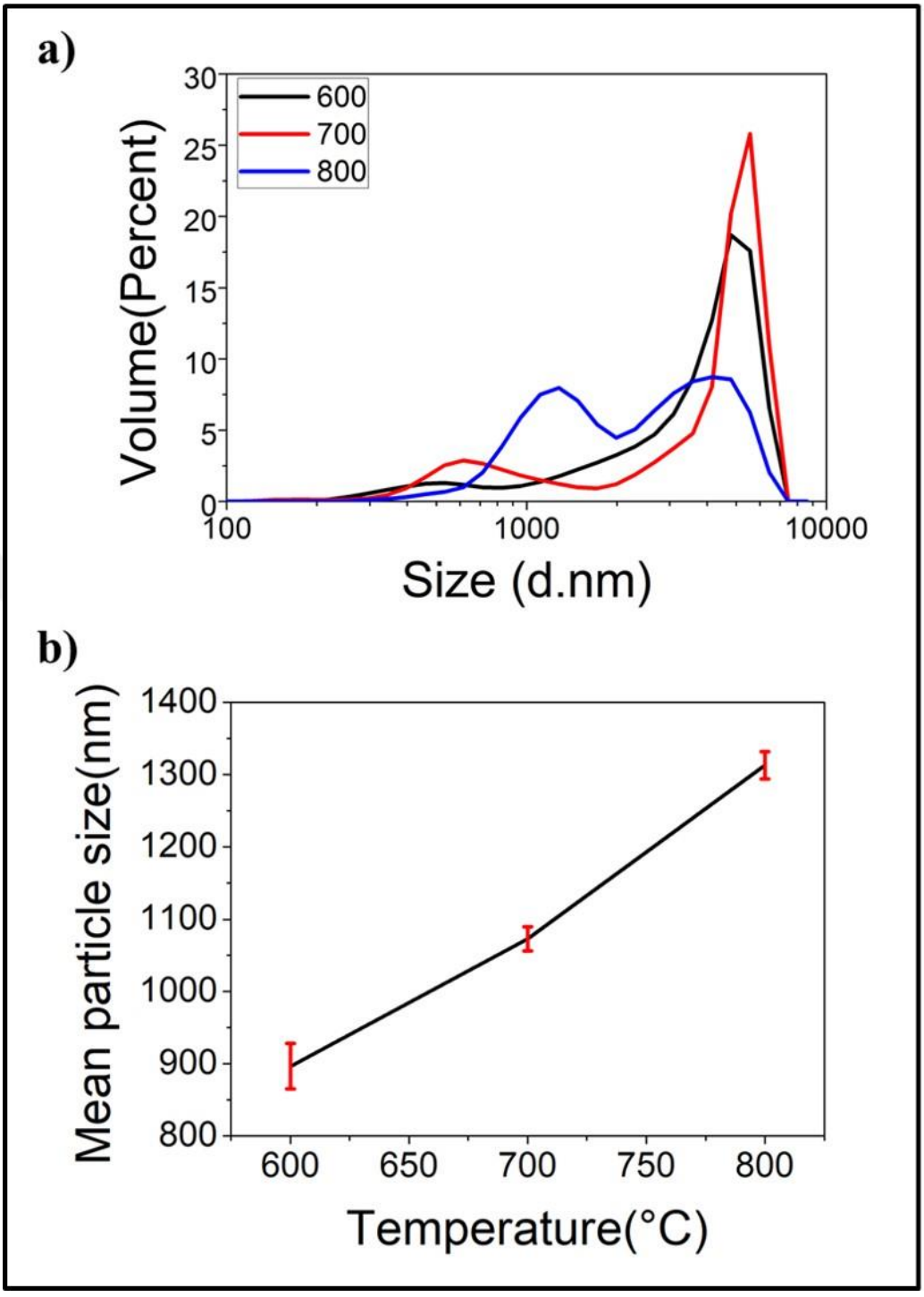

Figure 8.6: Effect of calcination temperature on a) particle size distribution and b) average particle size of NiO-YSZ powders.

8.2.2. Microstructure

Symmetrical half-cells were fabricated by depositing inks containing NiO-YSZ powders calcined at 600, 700 or 800 °C, followed by sintering at 1350 °C. The obtained NiO-YSZ composites were then reduced under 10% H_2-90%Ar flow, at 750 °C before microstructural analysis by scanning electron microscopy (SEM), to simulate electrochemical analysis conditions. Cross-sectional SEM images collected from the fracture surfaces of Ni-YSZ anode layers fabricated from NiO-YSZ powders calcined at 600-800 °C are provided in Figure 8.7. Ni-YSZ anode fabricated from powders calcined at 600 °C appears to be homogeneous in general, with only two larges (a few microns in size) particle chunks visible (shown with arrows in Figure 8.7a). With increasing powder calcination temperature, both the number and size of these large particle chunks increase significantly (Figures 8.7b and c), in agreement with the particle size analysis in Figure 8.6. Although the distribution of Ni and YSZ phases within these particle chunks may be homogeneous and provide long triple phase boundaries (as seen in Figures 8.7d-f), they are hardly sinterable, thus, their extent of bonding to the electrolyte and to their surrounding particles are quite poor (Figures 8.7b and c). The deteriorated contact between the powders and the electrolyte substrate is also evident when the low-magnification top surface images of anodes using powders calcined at 600 and 700 °C (Figures 8.7g and h) to those using powders calcined at 800 °C (Figure 8.7.i). Consequently, electrochemical activity is expected to decrease with increasing powder calcination temperature.

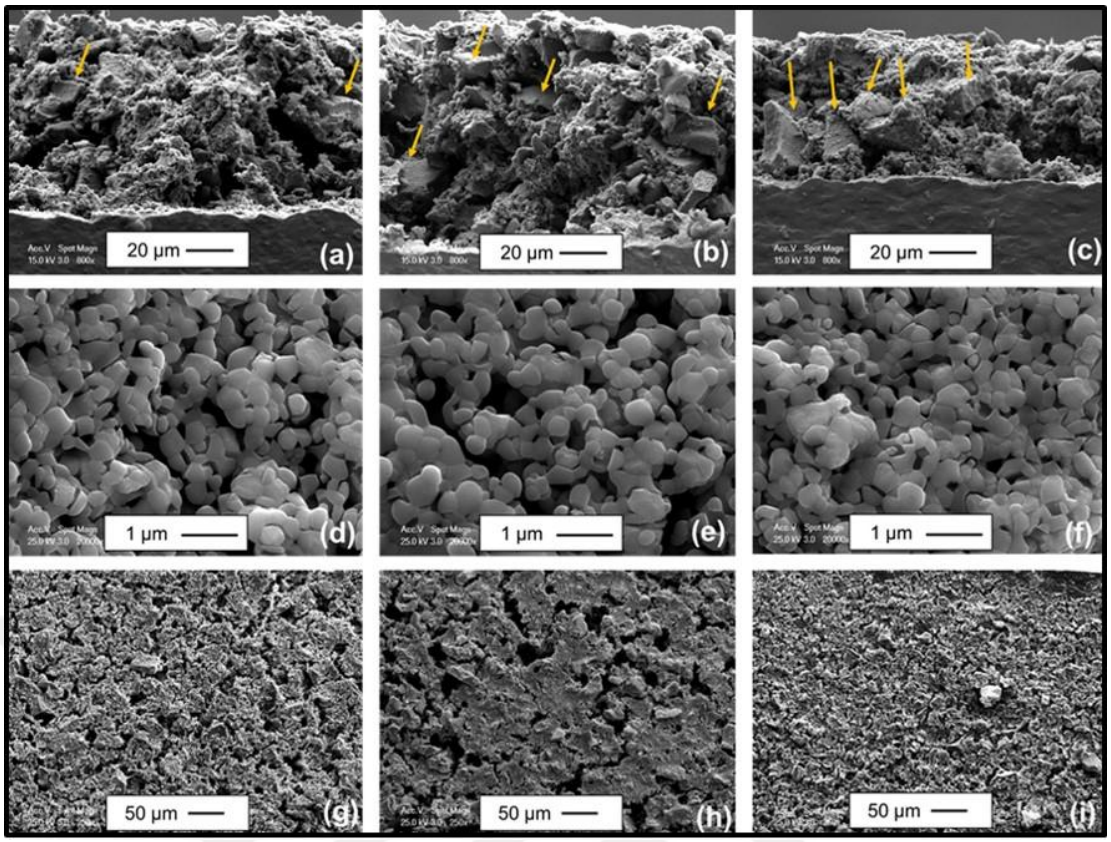

Figure 8.7: Cross section SEM of a) 600°C powder b) 700°C powder c) 800°C powder
Surface SEM of d,g) 600°C powder e,h) 700°C powder f,ı) 800°C powder.

8.2.3. Electrochemical Performance

The assessment of the electrochemical activities of Ni-YSZ anodes prepared from Pechini-derived NiO-YSZ powders was performed by electrochemical impedance spectroscopy (EIS) analyses of symmetrical half-cells at 500-750 °C, under humidified 10%H_2 – 90%Ar flow. Figures 6a-c depict the Nyquist curves obtained at 750 °C from Ni-YSZ anodes fabricated from composite powders calcined at 600-800 °C, with corresponding Bode diagrams provided in the insets. At this operating temperature, the EIS responses consisted of two distinct semi-circles, indicating two separate electrochemical processes (Figures 8.8.a-c). Therefore, an equivalent circuit consisting of one resistor (Rs) connected in series to two other resistors (R1 and R2), both of which is also connected in parallel to two constant phase elements (Q1 and Q2) was used to fit the EIS data (Figures 8.8a-c). Here, Rs describes the resistance to ionic conduction through the YSZ electrolyte, while R1/Q1 and R2/Q2 describe the high and low frequency processes, respectively. At

lower operating temperatures, only one semi-circle was observed (data not shown), therefore fitting procedures were performed using an equivalent circuit consisting of only one R/Q element connected in series to Rs.

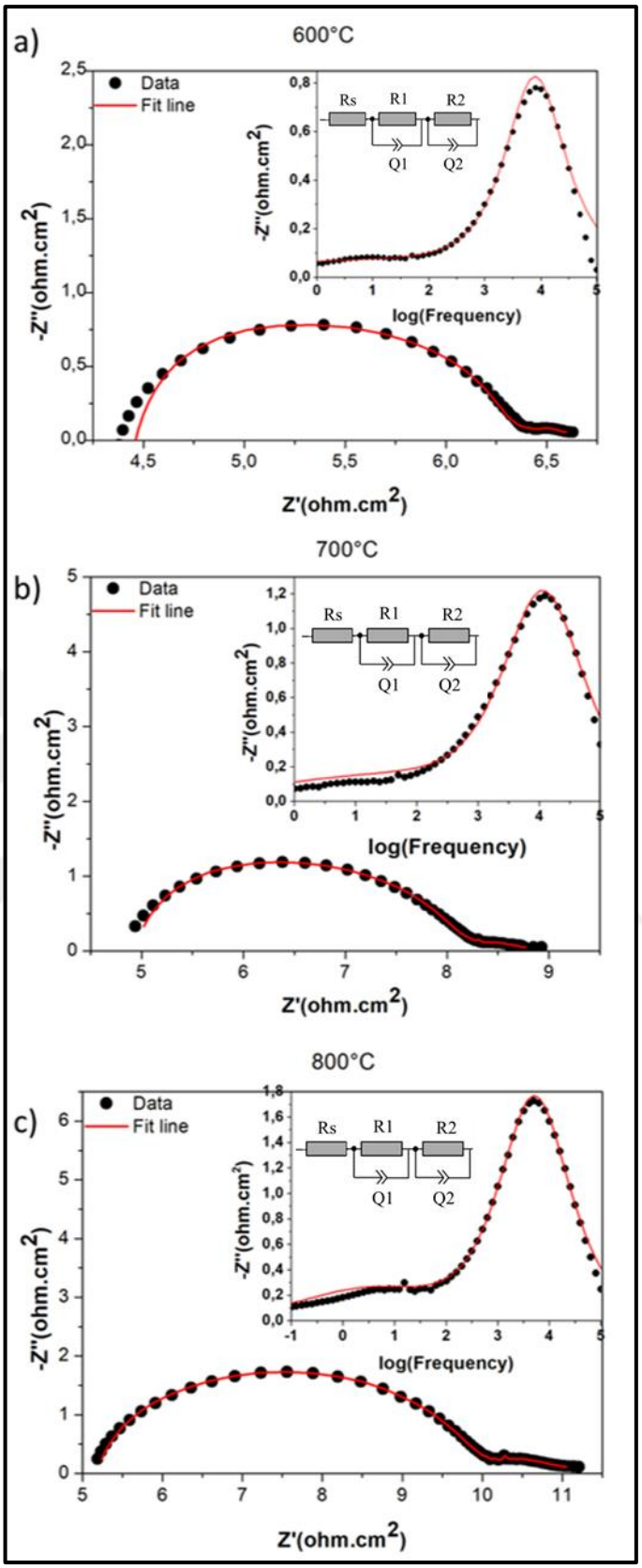

Figure 8.8: Electrochemical impedance spectroscopy data obtained from anodes fabricated using powders calcined at a) 600, b) 700 and c) 800°C in the form of Nyquist and Bode (insets) diagrams. Note that the filled circles and the red lines show the data points and the fit curves, respectively.

Table 8.1 provides the resistance and frequency values obtained from the equivalent fitting of the EIS data, in addition to the capacitance values calculated from these two parameters. Rs values, evidently, increased from 4.5 to 5.1 Ω.cm2 with increasing powder calcination temperature (Table 8.1).

Table 8.1: Resistance, frequency and capacitance values summarized table.

Powder calcination temperature (°C)	Rs ($\Omega.cm^2$)	$f_1$summit (Hz)	R_1 ($\Omega.cm^2$)	C_1 (F/ cm^2)	$f_2$summit (Hz)	R_2 ($\Omega.cm^2$)	C_2 (F/ cm^2)	Rtotal ($\Omega.cm^2$)	Ranode ($\Omega.cm^2$)
600	4.50	17100	1.83	5.09×10^{-6}	153	0.50	2.08×10^{-3}	2.33	1.16
700	4.76	26800	3.10	1.92×10^{-6}	180	1.08	8.19×10^{-3}	4.18	2.09
800	5.06	15300	4.78	2.18×10^{-6}	25	1.42	4.56×10^{-3}	6.20	3.10

Considering that i) the conductivity of YSZ electrolyte substrates are the same and ii) the thickness variation in the electrolyte substrates is below ca. 5%, the increase in Ωic resistance is considered to have originated from the poorer physical, hence electrical contact in Ni-YSZ anodes fabricated from larger particles. In a similar way, the sizes of both high and low frequency semi-circles also increased with increasing powder calcination temperature. R1 increased from 1.83 to 4.78 $\Omega.cm^2$ when the powder calcination temperature was increased from 600 to 800 °C. The capacitance values associated with the high frequency process were in the 10^{-6} F/cm^2 range, which has been ascribed to the double layer capacitance at the Ni/YSZ interface [65,66]. The low capacitance associated with the high-frequency arc suggests that the charge transfer at the triple phase boundary dominated the total polarization resistance. The low frequency process, on the other hand, had capacitance values in the10^{-3} F/cm^2 range, which was ascribed to the hydrogen adsorption/desorption processes at the Ni surface. [65] The fact that R1 is significantly larger than R2 in all cases indicates that charge transfer at the triple phase boundary is the process limiting the hydrogen oxidation rate in all samples.

Rtotal values were determined by adding R1 and R2, which was then divided by two, to obtain the total polarization of one electrode (Ranode) in the symmetrical two-electrode cell (Table 8.1). The lowest Ranode value obtained was 1.16 $\Omega.cm^2$, in the case of Ni-YSZ anode prepared from NiO-YSZ composite powders calcined at 600 °C. This value corresponds to a better electrode performance than reported in REF-65, in which Dasari et al obtained a Ranode value of 1.63 $\Omega.cm^2$ at 750 °C from

Ni-YSZ anode fabricated by co-sintering a mixture of NiO and YSZ powders. On the other hand, infiltration of Ni into porous YSZ scaffolds resulted in lower Ranode values than those reported here, i.e., 1.3 and 0.1 Ω.cm^2 at 700 and 800 °C, respectively. [47,67] Despite the higher electrochemical activity of the infiltrated Ni-YSZ anodes, the necessity for numerous infiltration/drying cycles for their fabrication (as many as 60 cycles in the case of REF-47) renders them unsuited for scaling up.

Figure 8.9 shows a comparison of the temperature dependencies of the Ni-YSZ anodes fabricated from composite NiO-YSZ powders synthesized by the Pechini method. Activation energies of anodes fabricated from NiO-YSZ composites calcined at 600, 700 and 800°C were determined as 0.98, 0.94 and 1.20 eV, respectively. The activation energies of the charge-transfer dominated polarization resistances of Ni-YSZ anodes have been reported to lie in the 1.00-1.30 eV range [47, 67], due to the combined effects of oxygen ion transport through the YSZ network (which has an activation energy of 0.9-1.1 eV [67]) and electron transfer at the triple phase boundary (which has an activation energy of ca. 1.30 eV [67, 68]). The activation energies of Ranode obtained from anodes with NiO-YSZ powders calcined at 600 and 700 °C are close to that of oxygen ion transport through the YSZ network, while the activation energy of Ranode obtained from anodes with NiO-YSZ powders calcined at 800 °C is close to that of the electron transfer at the triple phase boundary. The effect of powder calcination temperature on the Ranode activation energy is likely related to the quality of the powder/electrolyte substrate contact. Specifically, coarse powders obtained by calcination at 800 °C resulted in a poor powder/electrolyte substrate contact, resulting in the dominance of the resistance of the high activation energy-electron-transfer process.

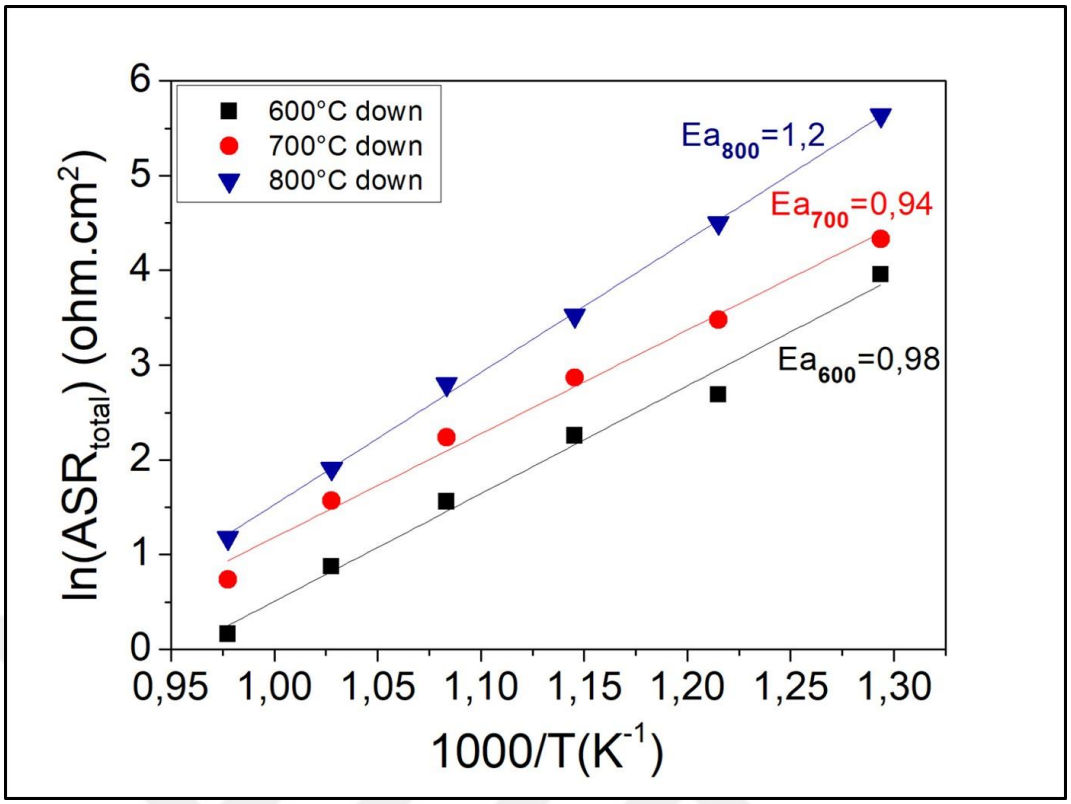

Figure 8.9: Temperature dependence of Ranode, measured in the cooling regime.

8.3. Thin Film Anodes from Polymeric Precursors

Results of the thin film-based anodes will be discussed in this section. XRD, crystallite size, particle size and thermal analysis results in mentioned before was for both powder based and thin film based samples, this section focus on polymeric precursors viscosity and the thin films microstructural and electrochemical analysis results. For the produce thin films separately prepared NiO and YSZ solution precursors were mixed with 60:40 volumetric ratio of NiO to YSZ, then polymeric precursor mixed with a solvent to reduce surface tension and homogenous distribution on electrolyte surface that added amount of the precursor weight. That coated on electrolyte surface with spin coater 1000-3000 rpm for 40 seconds then heat treated at 400˚C degrees. That deposition/decomposition cycle was repeated 5-20 times to achieve the required thin film thickness. As mentioned before in the experimental part this thesis mainly focuses on NiO-YSZ thin film deposition because of the thin film coated samples do not require high temperature calcination thus better electrochemical activity achieved.

8.3.1. Microstructure

In the literature, single phase oxide coatings have been deposited onto dense substrates by many solution precursor-based methods [69, 70]. In the present study, our aim is to fabricate composite coatings using a mixture of the precursors of the two phases, specifically NiO (Ni after in-situ reduction) and YSZ. We envision that the two insoluble phases will form as a result of the preferential clustering of the cations upon heat-treatment and that the obtained composite will have a nanostructured morphology.

Figure 8.10a depicts the top-down scanning electron microscopy (SEM) image of the NiO film deposited on the YSZ substrate. A homogeneous and interconnected film with ca. 80 nm-sized grains beginning to form is evident (Figure 8.10a). After reduction under 10% H_2-90% Ar flow at 600 ˚C, some uncovered electrolyte surfaces are seen, which is likely due to the high surface tension at the metal/ceramic interface (Figure 8.10b). Evidently, the addition of the polymeric YSZ precursor had a significant impact on the as-prepared and as-reduced microstructure of the Ni film. The as-prepared microstructures of the NiO-YSZ without heat treatment (NiO-YSZ-nh) and NiO-YSZ heat treated at 800 °C for 4 hours (NiO-YSZ-800) does not consist of 80 nm-sized grains, as NiO thin film did. NiO-YSZ-nh had a featureless surface microstructure, whereas NiO-YSZ-800 surface consisted of ca 20 nm-sized particles (Figures 8.10c and e). The as-reduced states of these anodes (Ni-YSZ-nh and Ni-YSZ-800 in Figures Figures 8.10d and f) did not induce uncovered YSZ substrate surfaces but had additional porosity in comparison to their as-fabricated states. The absence of substrate de-wetting is due to the YSZ phase within the film acting as an anchor, inhibiting the movement of the Ni phase. Porosity generation in NiO-YSZ anodes upon reduction into Ni-YSZ has been commonly observed, due to the smaller molar volume of Ni (molar volume) in comparison to NiO (molar volume).

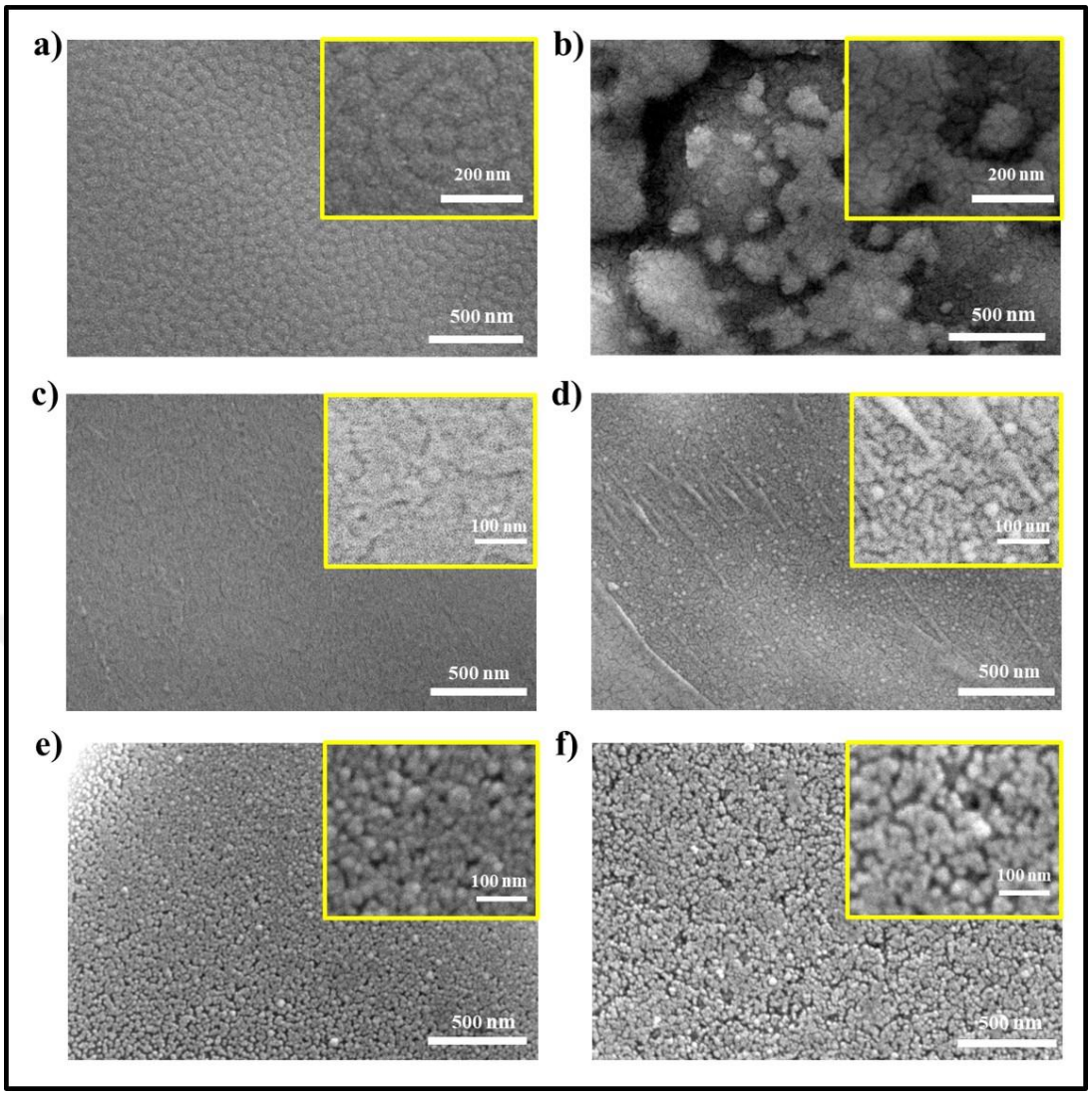

Figure 8.10: Microstructure of a) NiO thin film b) Ni thin film (a as reduced) c) NiO-YSZ thin film d) Ni-YSZ thin film (c as reduced) e) NiO-YSZ thin film pre-heat treated in air at 800˚C for 4 hours f) Ni-YSZ thin film pre-heat treated in air 800˚C for 4 hours (e as reduced).

The spatial distribution of the Ni and YSZ phases is as important as the general microstructure, just discussed, to come up with a general understanding of the triple phase boundary length present in the Ni-YSZ thin films. Unfortunately, SEM-EDX analyses have proven inadequate to reach this goal (data not shown here), mostly due to the large interaction volume this technique brings about. Therefore, to be able to map the distribution of the Ni and YSZ phases, we have used transmission electron microscopy-energy dispersive x-ray spectroscopy (TEM-EDX analyses) on the Ni-YSZ-nh and Ni-YSZ-800 samples (Figures 8.11 and 8.12). To perform these analyses, ca. 50 nm-thick slices of samples were cut via focused ion beam (FIB) milling.

Figure 8.11a shows the bright field TEM image along with the EDX maps of Ni, Zr, Y elements and their overlaid image. Evidently, the Ni-YSZ composite structure consisted of ca. 7 nm-thick Ni and YSZ layers stacked up in an alternating fashion. In Figure 8.11b, EDX maps collected at higher magnification, along with a line-scan, which indicated no dissolution among the two phases are given. It is interesting to note that, there are 20 Ni and 20 YSZ layers, which is exactly equal to the number of spin coating/drying cycles performed to fabricate the film. The correlation between the number of deposition/drying cycles and the number of Ni and YSZ layers or whether the layered structure is a consequence of these parameters will be discussed later. Meanwhile, it is worth mentioning that the although the layered structure consists of nanoscale particles, an interconnectivity among the Ni and YSZ phases is lacking (Figures 8.11a and b), hence, a significant portion of the generated TPB is likely to be ineffective.

Figure 8.12 shows the TEM-EDX images of Ni-YSZ-800, which reveal a microstructure with a larger average particle size (ca. 20 nm this time), but a greater extent of interconnectivity in comparison to the case of Ni-YSZ-nh, which surely resulted from the pre-calcination step performed in the oxidized state.

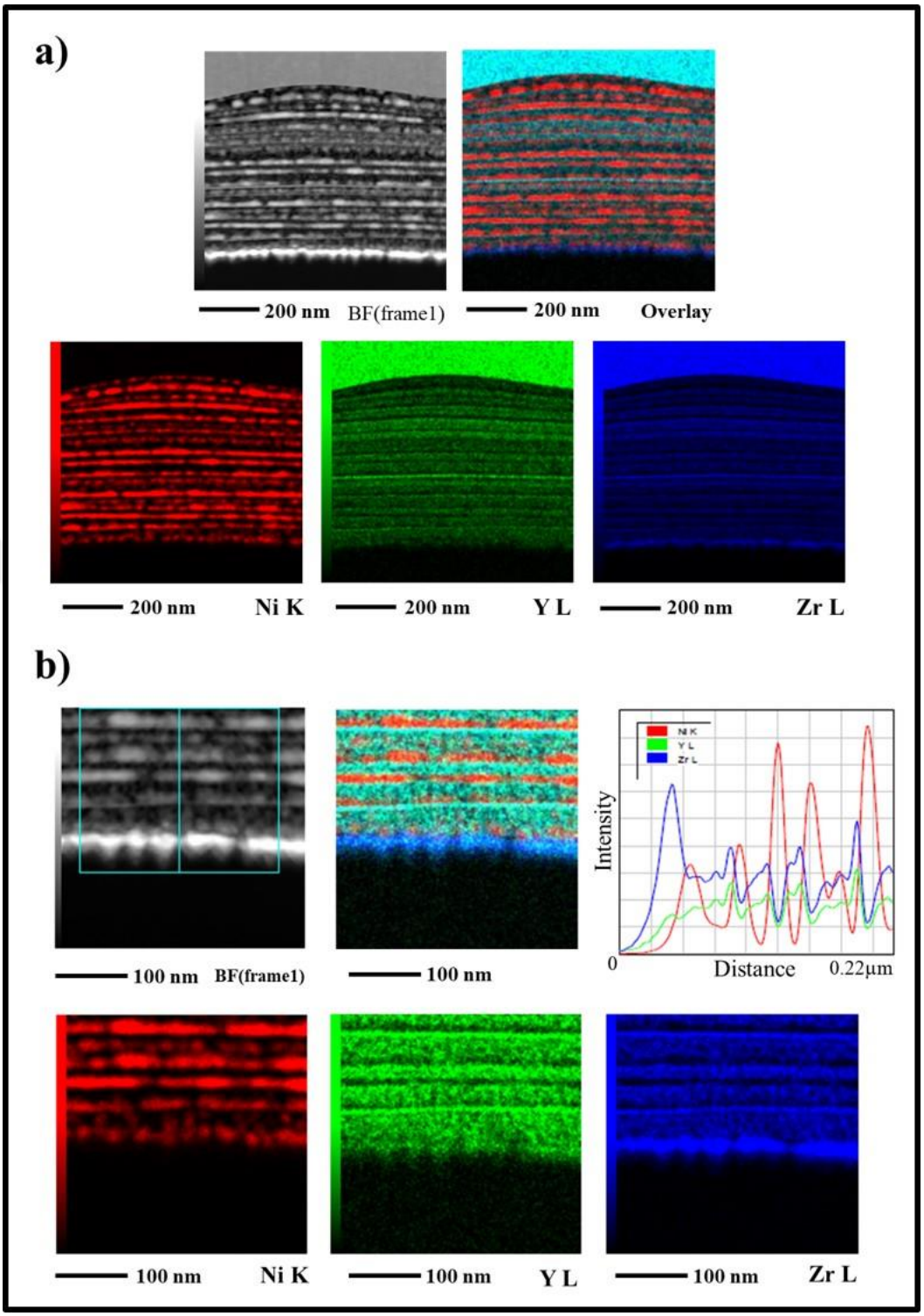

Figure 8.11: a-b) TEM analysis of Ni-YSZ thin film without prior heat treatment.

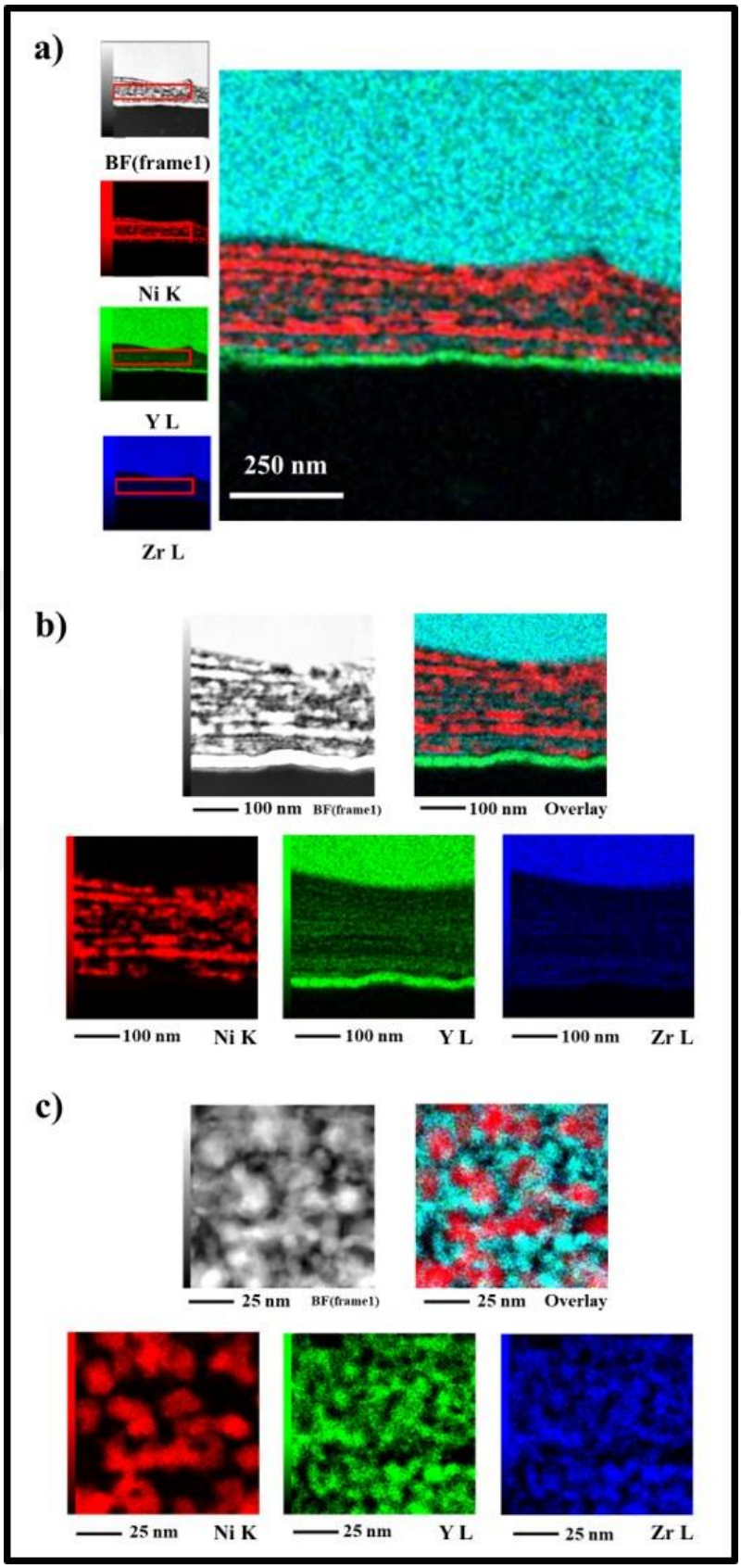

Figure 8.12: a-c) TEM-EDX analysis of Ni-YSZ thin film pre ht at 800˚C for 4 hours.

8.3.2. Electrochemical Performance of Thin Film Anodes

To evaluate the electrochemical performance of the Ni-YSZ anodes fabricated by the preferential clustering of cations from polymeric precursors, electrochemical impedance spectroscopy (EIS) measurements were performed at 450-600 °C under humidified 10%H_2-90%Ar gas flow. Figure 8.13a shows the impedance responses obtained from Ni thin film, Ni-YSZ-nh and Ni-YSZ-800 at 600 °C, depicted in the form of Nyquist and Bode plots. In general, the distance between the two horizontal intercepts gives the total polarization resistance of the two electrodes, ASR_{pol} (i.e, distance needs to be divided by two to obtain the polarization resistance of one electrode - ASR_{anode}) and the high frequency horizontal intercept (called the ohmic resistance) gives the resistance to oxygen ion transport within the electrolyte, plus any current collection resistances in the Nyquist plots given in Figure 8.13a.

In the current case, for a clearer comparison, we have subtracted the ohmic resistances from all of the Nyquist plots Figure 8.13a. The Bode plot of the Ni thin film electrode indicates that the major electrochemical process dominating the overall impedance is at ca 10^2 Hz (Figure 8.13.a).

Evidently, the Ni thin film electrode exhibited an extremely high ASR_{anode} value of 45 $\Omega.cm^2$ 600 °C (Figure 8.13.a). Such a poor performance was expected from the Ni thin film electrode because the only TPB it contains is that at the Ni/electrolyte/gas interface. The semi-circles obtained from Ni-YSZ-nh and Ni-YSZ-800 were so small that they could not be visualized in the same Nyquist plot as the Ni thin film electrode (Figure 8.13.a). Therefore, the Nyquist and Bode plots of Ni-YSZ-nh and Ni-YSZ-800 are depicted in a separate plot (Figure 8.13a). ASR_{anode} values of ca. 1 and 0.75 $\Omega.cm^2$ were obtained from Ni-YSZ-nh and Ni-YSZ-800, respectively at 600 °C (Figure 8.13.b). These values correspond to electrochemical performances far exceeding those obtained from conventionally prepared Ni-YSZ anodes. For example, X. Xi et al obtained an ASR_{anode} value of 5 $\Omega.cm^2$, at 600 °C in Ni-YSZ anodes fabricated by co-sintering of NiO and YSZ powders [71].

Figure 8.13c provides the temperature dependence of the ASR_{anode} values, indicating activation energies in the 0.9 – 1.1 eV range, in agreement with the literature [67,68].

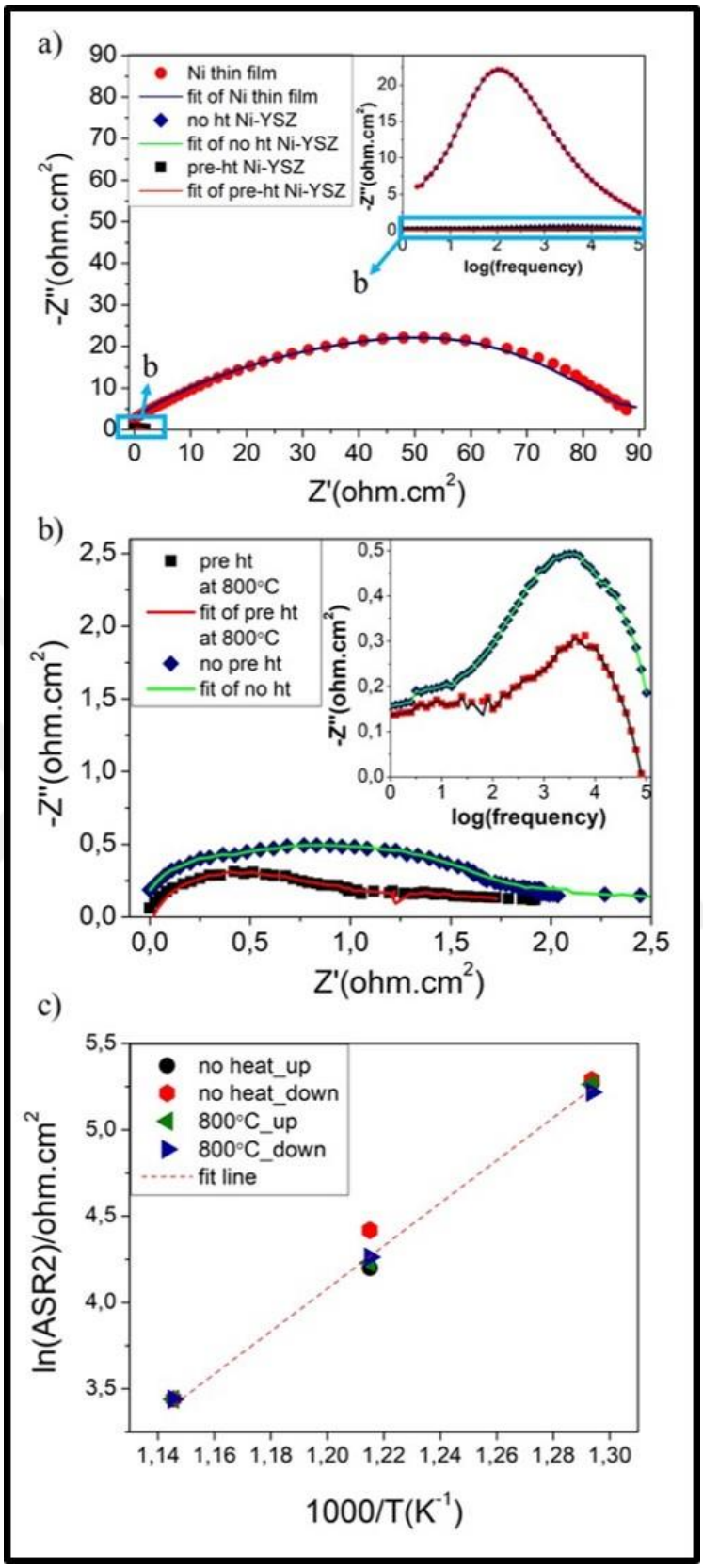

Figure 8.13: a) Nyquist and inset Bode plot of Ni and Ni-YSZ thin films b) Nyquist and Bode plots of Ni-YSZ thin films c) ln (ASR)-1000/T graph of Ni-YSZ thin films.

8.3.3. Long-Term Electrochemical Performance Stability

The purpose of trying to lower the SOFC operating temperatures is to slow-down the diffusion – mediated phenomena that cause performance degradation. To be able to lower the SOFC performance degradation with minimal performance loss, here, we have fabricated Ni-YSZ anodes with a nanocomposite structure and hence, extremely long triple phase boundaries. However, the nanoscale particle size of the developed anode itself is likely to induce a driving force for surface area loss even at 600 °C. In this section, we will describe our efforts on understanding the long-term performance degradation in polymeric precursor-derived Ni-YSZ anodes and its prevention.

8.3.3.1. Effect of Pre-Calcination Temperature

To analyse whether the thin film Ni-YSZ developed here is stable or not upon long-term operation, EIS measurements were performed intermittently upon 100-hour exposure to 600 °C under humidified 10% H_2 - 90% Ar gas mixture. Since it has been reported that the highest fuel cell performance degradation rates are observed in the first 250 hours of operation [38], 100-hour tests were considered reasonable for laboratory-scale experiments. Therefore, Ni-YSZ-nh exhibited an extremely fast increase in the ASR_{anode} value from 1.42 to 163.94 $\Omega.cm^2$ upon exposure to 100-hour exposure to 600 °C under the reducing gas flow (Figure 8.14.c). On the other hand, the ASR_{anode} value obtained from Ni-YSZ-800 increased from 0.93 to 9.49 $\Omega.cm^2$ under the same conditions with a linear trend, exhibiting a slope of 0.086 $\Omega.cm^2/h$. These results suggest that the pre-calcination temperature has a strong impact on performance stability.

The most plausible reason for the difference in the long-term performance stabilities is a difference in the microstructural evolutions of the as-prepared and pre-calcined samples taking place during operation. Figures 8.14a and b show the top-surface SEM images of Ni-YSZ-nh and Ni-YSZ-800, respectively. The microstructure of Ni-YSZ-nh appears to consist of ca. 40 nm sized particles (Figures 8.14a), while the surface of the Ni-YSZ-800 appeared featureless (Figures 8.14.b).

In the literature, the degradation mechanisms of Ni-YSZ anodes have largely been connected to the growth of Ni particles and the consequent loss of triple phase boundary length [35,36]. In the case of conventional anodes, the top surface is generally too far from the electrochemically active zone located close to the electrolyte [72]. Therefore, the microstructural evolution of the top surfaces and its correlation to the performance stability has not been studied up to date. However, in electrodes with a few micron-thicknesses, the top surface is within the electrochemically active zone, thus the microstructural changes that occur at this location is strongly influential to the overall performance stability. Muecke et al prepared Ni-CGO thin film anodes by spray pyrolysis and reported that in the sample which was not pre-calcined, Ni particles coarsened, pushing away the mechanically weak CGO network [53]. The majority of the coarsening process took place at the top surface of the Ni-CGO film, where there is no constraint whatsoever [53]. In the present case, it is likely that a similar mechanism is at play, i.e., the pre-calcination step strengthens the YSZ phase and inhibits Ni coarsening under the operating conditions. In this regard, it can be deduced that the particles at the surface of the Ni-YSZ-nh are Ni particles moved out of the surface, due to the lack of mechanical constraint by the weak YSZ network (Figure 8.14a). For the first time in the literature, we report here that the pre-calcination step has such a profound impact on electrochemical performance stability.

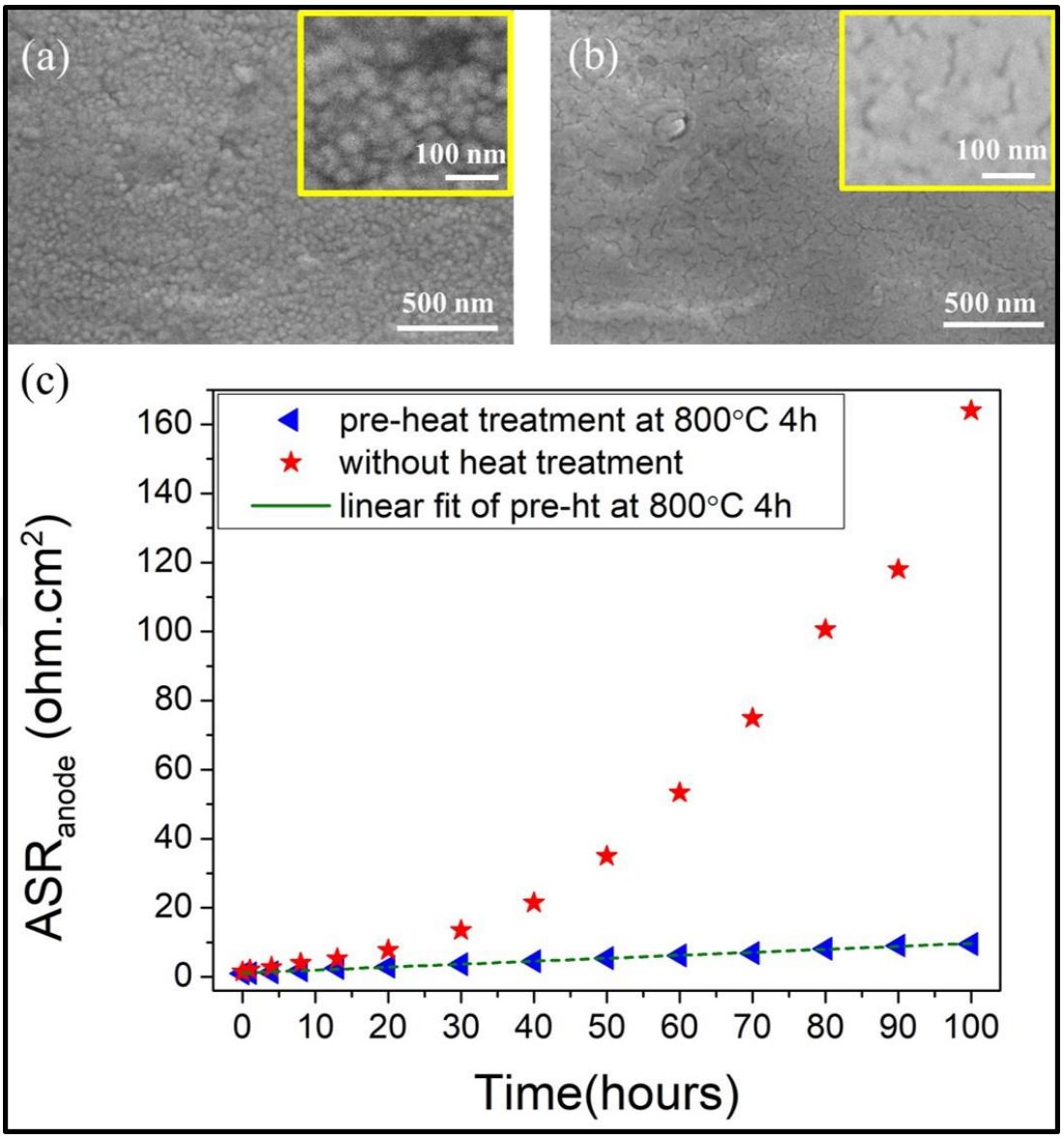

Figure 8.14: Scanning electron microscopy images obtained from the top surfaces of a) Ni-YSZ-nh and b) Ni-YSZ-800 after 100 hours exposure to 600 °C, under 10% H_2 – 90% Ar gas mixture.
c) Changes in the ASR_{anode} of Ni-YSZ-nh and Ni-YSZ-800 upon exposure to 600 °C, under 10% H_2 – 90% Ar gas mixture.

8.3.3.2. Effect of CeO_2 Overlayer Deposition

As mentioned earlier, the microstructural degradation mechanism of nanocomposite Ni-YSZ anodes involves the coarsening of the Ni particles i) within the coating by pushing the YSZ network and ii) formation of even larger Ni particles at the top surface of the Ni-YSZ anodes where there is no constraint. We have seen that strengthening the YSZ network by pre-calcination impacts the first step and

reduces the performance degradation (Figure 8.14a). Another precaution to take to slow down performance degradation would be to inhibit the Ni coarsening at the top surface, which can be realized by introducing a mechanically stable top-surface overlayer. An ideal overlayer material would be an oxide (thereby would have a relatively stable microstructure under the operating temperatures) that is also an electronic conductor under reducing conditions to avoid additional current collection resistances. Undoped CeO_2 is such a material, which also exhibits a certain electrocatalytic activity for fuel oxidation [73]. Therefore, we have deposited CeO_2 layers onto the Ni-YSZ anodes to prevent Ni coarsening at the surface.

To determine the effect of CeO_2 overlayer alone, symmetrical Ni-YSZ half-cells without prior heat-treatment were coated with 5 and 10 layers of CeO_2. For the EIS measurements, samples were reduced 10%H_2 – 90%Ar flow at 500 ˚C, and long-term stability test stared 600˚C then continued the measurement for 100 hours at this temperature. As seen in Figure 8.15, degradation rates of 0.044 and 0.030 $\Omega.cm^2/h$ were achieved in the cases of 5 and 10 layers of CeO_2 coating, respectively. The significantly enhanced stability of the polarization resistance in comparison to the Ni-YSZ anodes with no overlayers suggests that CeO_2 overlayers do inhibit Ni coarsening and stabilize the microstructure. To obtain even more stable anodes, both strong YSZ networks and stable surface morphologies are targeted. For this purpose, 10 layers of CeO_2 coatings were applied onto the composite anodes in the oxidized state, which were subsequently heat 800 °C before reduction and measurement. This sample exhibited an even lower degradation rate of reduced to 0.008 $\Omega.cm^2/h$. Microstructures examined with SEM after the long-term stability test shown in figure 8.15d-f, the microstructure of the pre heat treated sample denser and smaller particle sized.

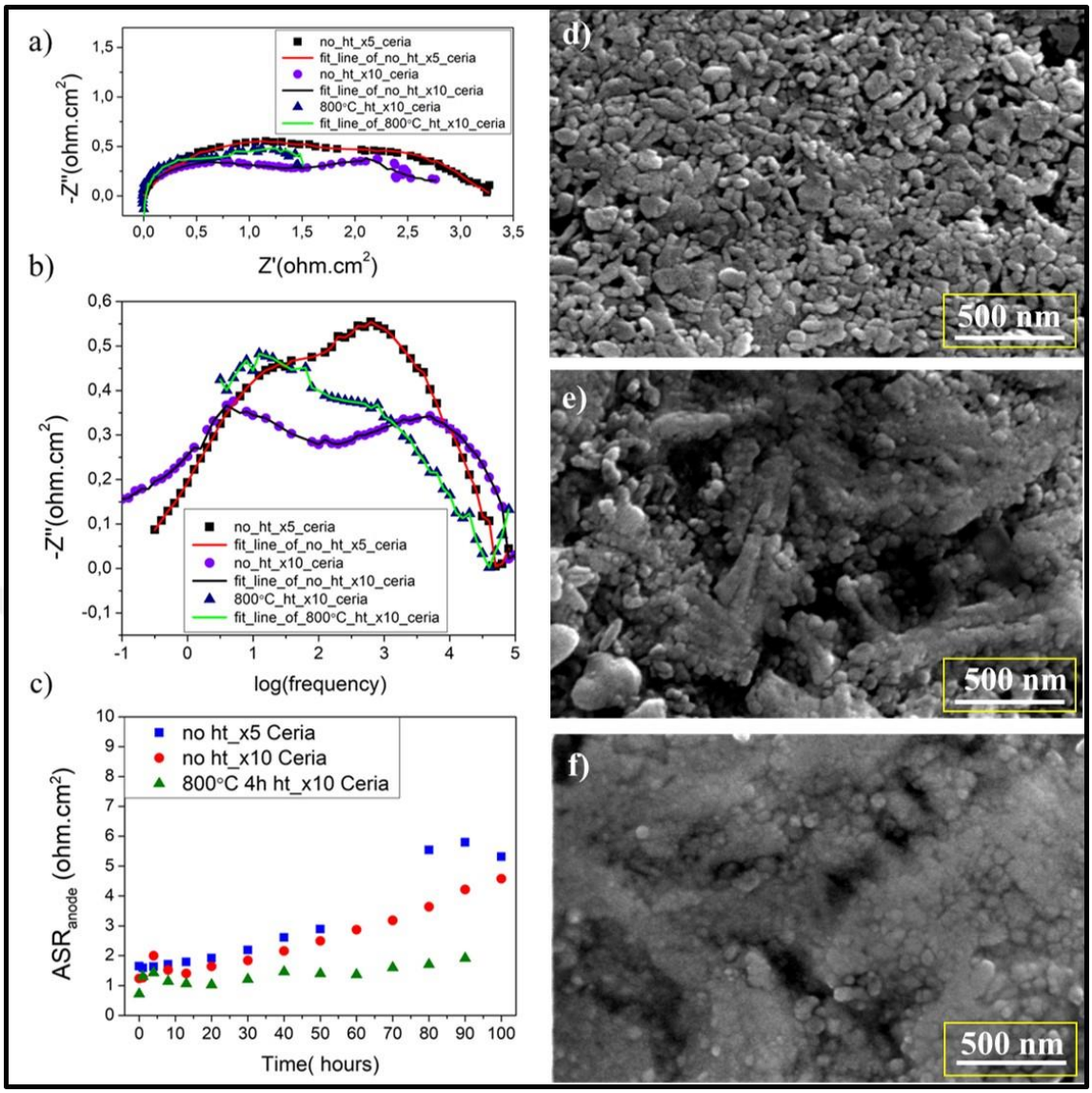

Figure 8.15: a) Nyquist plot of the 5 and 10 layers of ceria overlayer, and 10 layers of overlayer coated sample heat treated at 800C b) Bode plots of the sample from the a c) ASR change with long time testing d) Microstructure of the 5 ceria overlay sample after long-term testing e) Microstructure of the 10 ceria overlay sample after long-term testing f) Microstructure of the 10 ceria overlay sample heat treated at 800C after long-term testing.

8.3.3.3. Overall Long-Term Stability Improvements of Thin Films

To avoid the instability caused by anode degradation YSZ skeleton strengthened with pre-heat treatment at 800˚C and ceria overlayer coated to block the surface of the anode. Both ways improve the instability of the anode resistance, shown in figure 8.16 and when two solutions used together lowest degradation rate achieved.

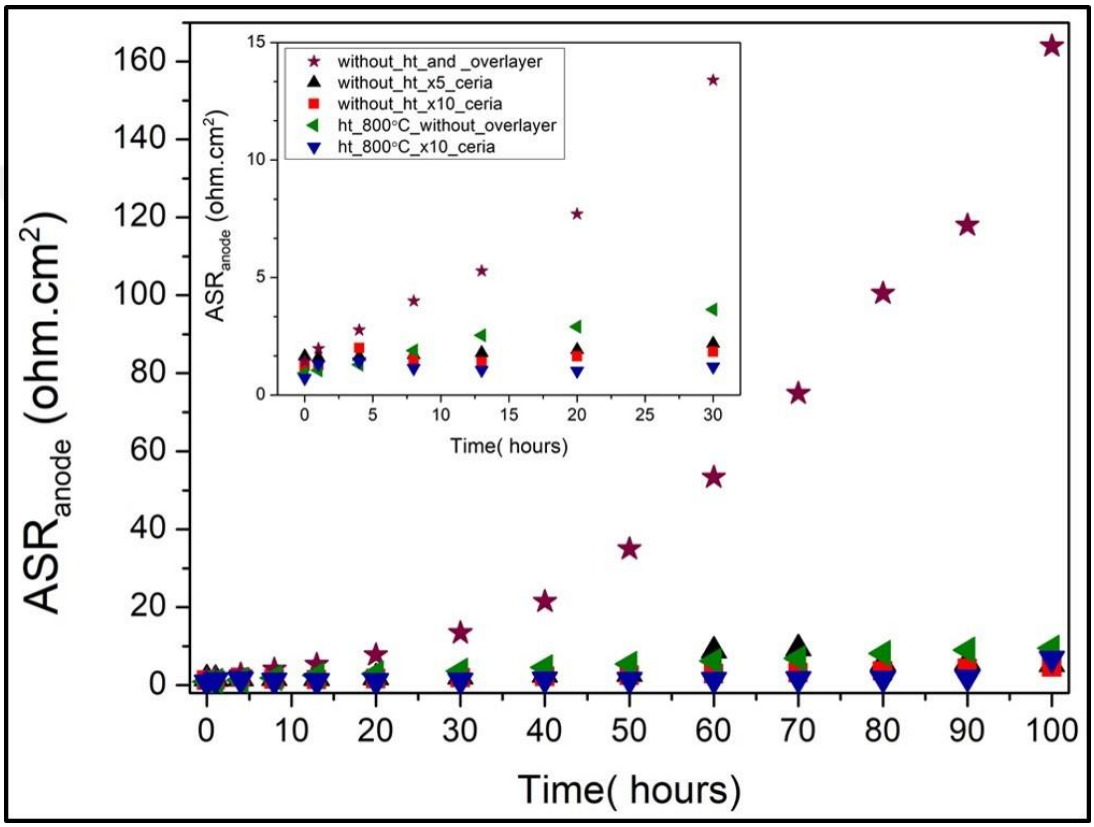

Figure 8.16: Overall heat treatment and overlayer coating effect on degradation of anode resistance.

SEM EDX-mapping of the samples after the long-term stability test from the top surfaces shown in figure 8.17. In figure 8.17.c ceria coated sample microstructure shown, Ni agglomerated areas observed on the surface.

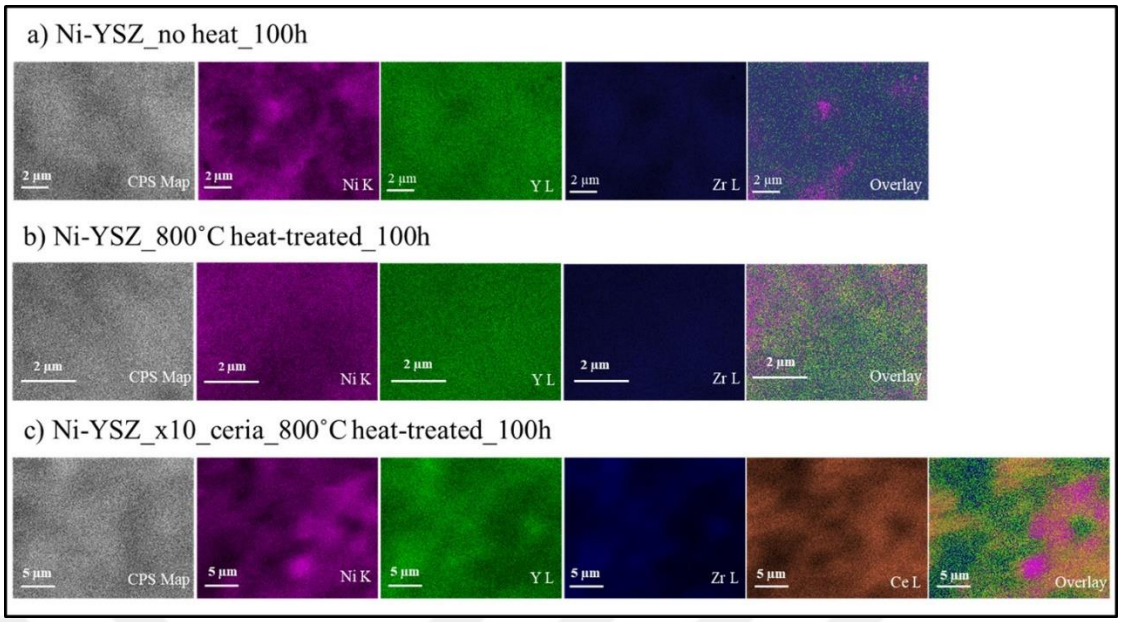

Figure 8.17: SEM EDX-mapping of a) no prior ht b) 800˚C heat treated c) 10 cycle ceria overlayer deposited and 800˚C heat treated, Ni-YSZ thin films after the long-term stability test.

To avoid the instability problem in the study of H.-S. Noh et al. Ni-YSZ anode produced by PLD and YSZ skeleton strengthen by annealing at 1200˚C [74] and A. Buyukaksoy et al. deposited YSZ as overlayer on the anode surface. [75] Without ht and and overlayer coating, after the 100 hours EIS testing Ni particles coarsening by destroying mechanically weak YSZ network and migrated to the outer surface of the anode, shown in figure 8.18.a. Pre-heat treated at 800˚C sample after the long term test has higher resistance to coarsening, because pre-heat treatment strengthen the YSZ network, shown in figure 8.18.b. And ceria overlayer coating on the anode surface also improved the Ni migration on the anode surface, shown in figure 8.18.c.

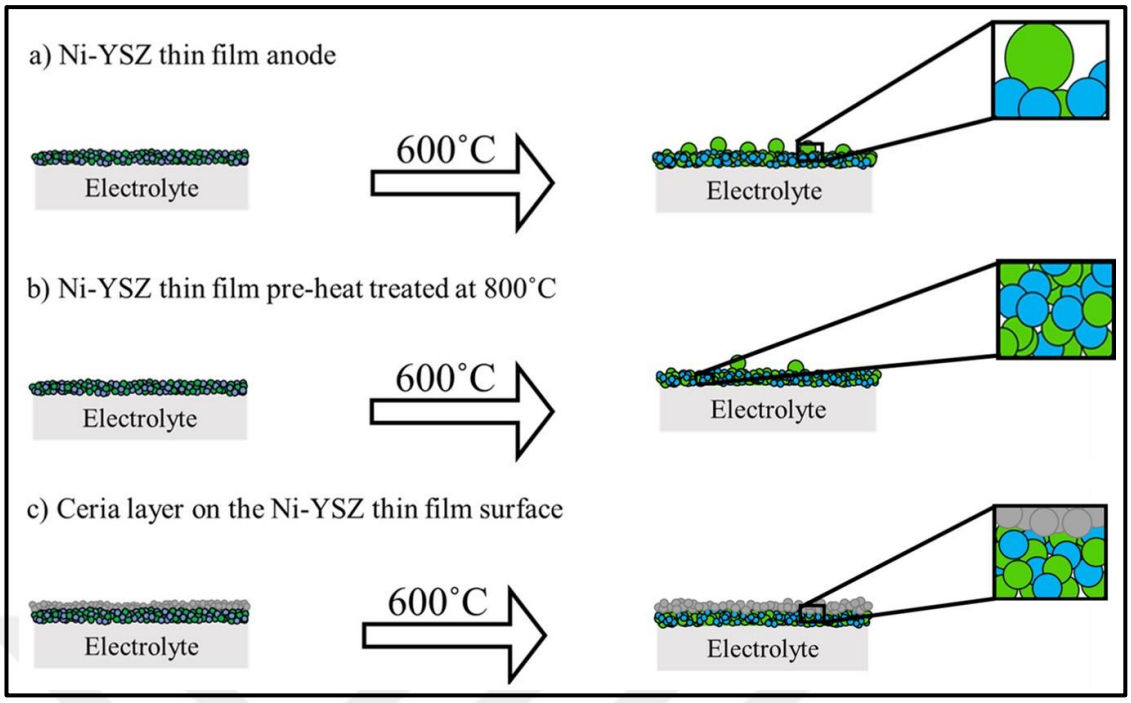

Figure 8.18: Scheme of a) Ni-YSZ thin film anode b) Ni-YSZ thin film pre-heat treated at 800˚C c) ceria layer on the Ni-YSZ thin film surface.

8.3.4. Influence of Deposition Parameters on The Microstructure and Electrochemical Performance

Further experiments focused to answer two questions these are;

-Does that layered structure depend on the number of thin film deposition cycles?

-What caused that layered structure?

To answering layered structure depends on the number of the thin film deposition cycles or not, samples coated with different rpms to achieve required thin film thickness. We coated the YSZ electrolyte with NiO-YSZ polymeric precursor with 3000 rpm for 20 deposition/decomposition experiments in general, for the comparison in there also coated with 5 deposition/decomposition cycle with 2000 rpm. A layer of ceria coated with the same rpm for 2000 rpm and for the 3000 rpm 5 layers ceria coated to achieve similar film thickness, Nyquist plot shown in figure 8.19.a Similar 2ASR values achieved by chosen coating cycles and rpms.

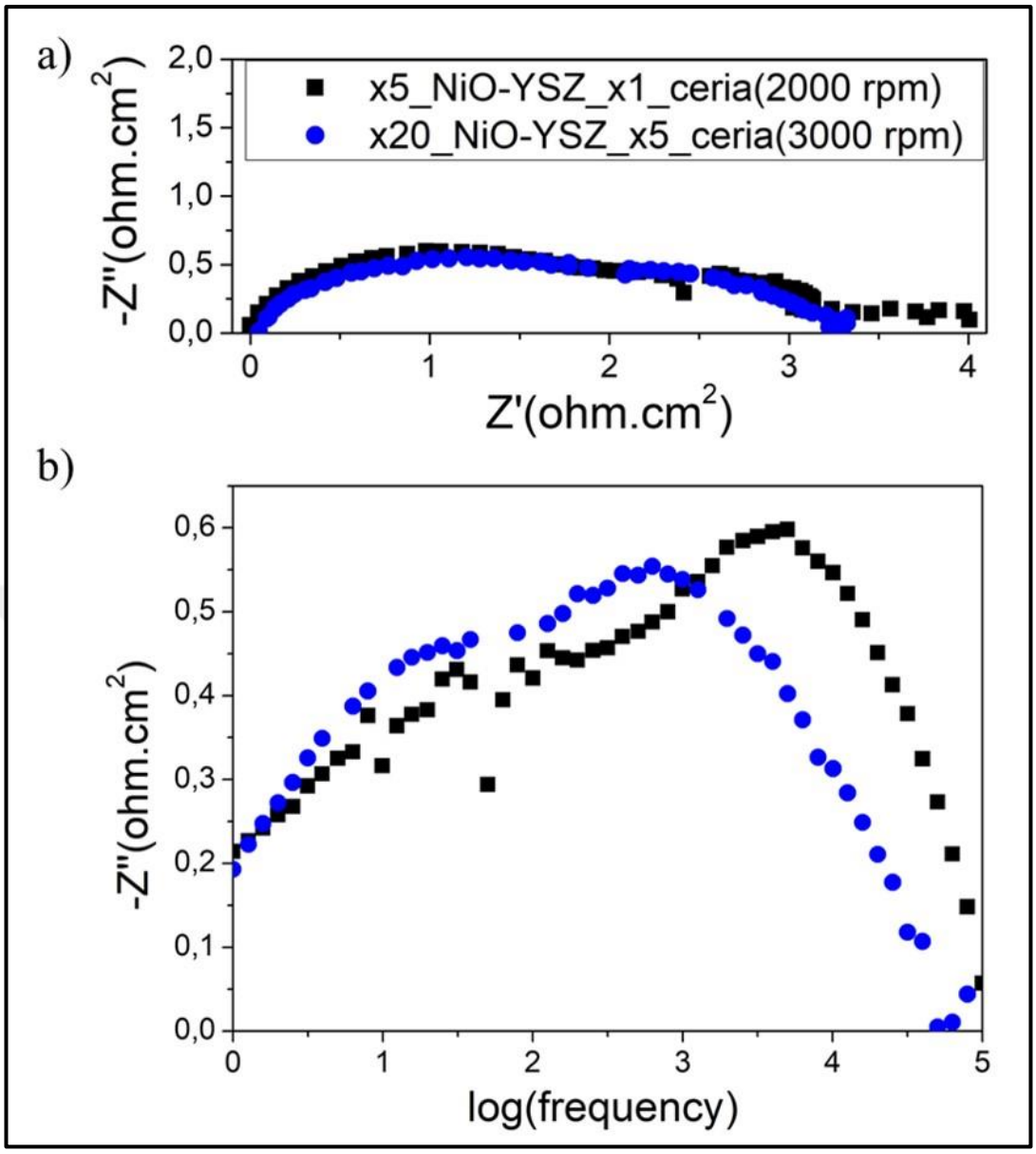

Figure 8.19: Rpm effect on the a) Nyquist diagram Ni-YSZ with 2000 and 3000 rpm b) Bode diagrams Ni-YSZ with 2000 and 3000 rpm.

The microstructure of the sample coated with 2000 rpm with 5 cycles of NiO-YSZ and a ceria deposition/decomposition by spin coater analysed by TEM-EDX mapping. Microstructural analyses were performed after EIS measurements at 600˚C in the humidified 10%H_2 – 90%Ar atmosphere for coated with 2000 rpm sample. The microstructure of Ni-YSZ anode coated with 2000 rpm shown in figure 8.20. Homogeneously prepared and coated of the NiO-YSZ precursor became the layered structure, and layers of Ni and layers of YSZ easily countable, ca. 20 layers of Ni observed in figure 8.11, and with the 5 cycles coated sample layered structure does

not observed in figure 8.20. The deposition cycle thickness affected layered structure when thin film deposited with thicker layers random distribution is allowed.

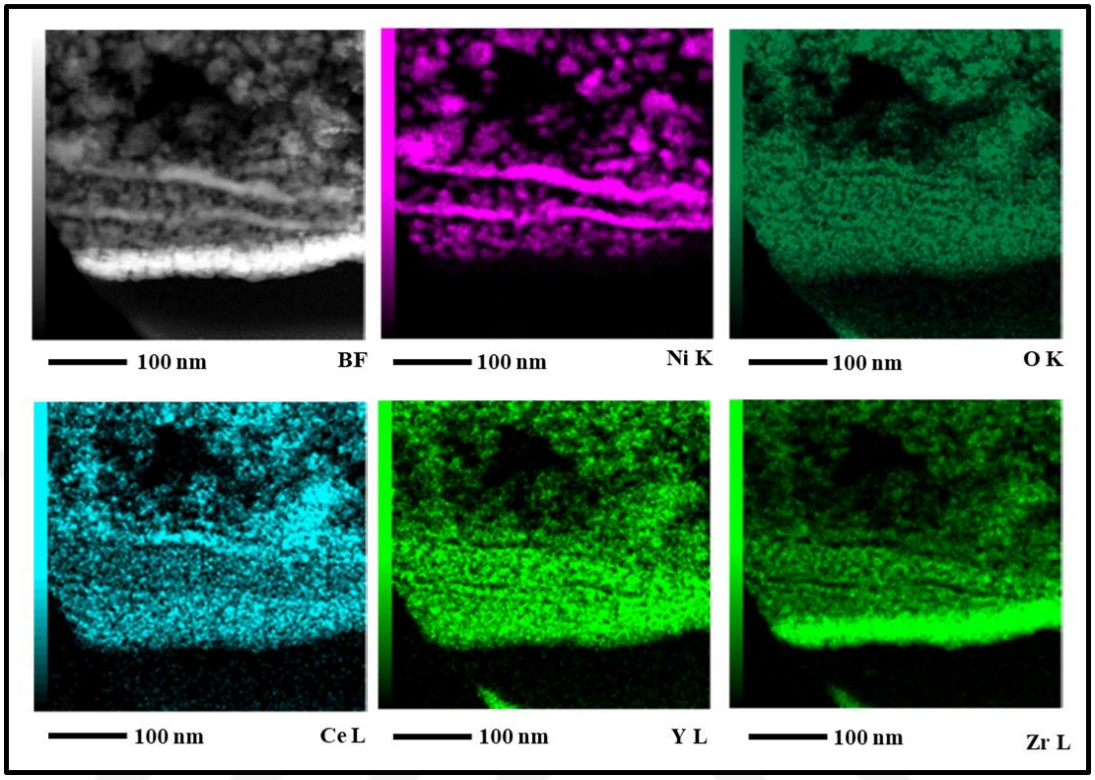

Figure 8.20: TEM-EDX Mapping of NiO-YSZ thin film 5 layers and a layer of ceria coated with 2000 rpm.

9. CONCLUSIONS

Composite solid oxide fuel cell (SOFC) anodes with long triple phase boundaries (TPBs) and thus, low polarization resistances must be developed to obtain high power densities from these devices even at temperatures significantly lower than the conventional ones, e.g., 600 °C). Conventional fabrication methods involving the co-sintering of electrocatalyst (mostly NiO) and ionic conductor (mostly yttria stabilized zirconia – YSZ) powders at high temperatures (1200-1400˚C) yield relatively coarse microstructures, which correspond to short TPBs and produce high polarization resistances.

In this work, a novel fabrication approach that allows the synthesis of both powders (which can be co-sintered to achieve composite anodes) and thin films (which do not require a high temperature sintering step) was adopted. This approach involved the preparation of polymeric precursors that contain all the cations of the electrocatalyst and ionic conductor phases, which are envisioned to form a nanocomposite structure upon heat treatment as a result of preferential clustering of cations.

X-ray diffraction (XRD) analyses revealed both NiO and YSZ phases were obtained upon the calcination of dried gels. A polarization resistance of 1.17 $\Omega.cm^2$ at 750 °C was achieved in the case of anodes fabricated from composite powders derived from polymeric precursor mixtures. On the other hand, the thin film anodes (which did not require high-temperature sintering) exhibited a polarization resistance of 0.75 $\Omega.cm^2$ at 600 °C. Transmission electron microscopy-energy dispersive x-ray spectroscopy analyses revealed that this extremely high electrochemical performance originated from the nanocomposite structure that consists of 5 - 20 nm Ni and 5 - 10 nm YSZ particles.

In this work, we have also focused on the long-term performance stability of the nanocomposite Ni-YSZ anodes, which are associated with a large driving force for microstructural coarsening due to their high surface area. It was determined that Ni particles tend to form larger particles upon long-term exposure to 600 °C by i) destroying the mechanically weak YSZ network and ii) migrating to the outer surface where there is no constrain for coarsening. Therefore, to enhance the performance stability, pre-heat treatment and an electronic conductor oxide overlayer deposition

were employed to strengthen the YSZ network and block Ni migration to the outer surface, respectively. As a result, significantly enhanced performance stabilities were obtained. These results are considered to be beneficial for the development of intermediate temperature solid oxide fuel cells that are commercially relevant.

REFERENCES

[1] Wuebbles D. J., Jain A. K., (2001), "Concerns about climate change and the role of fossil fuel use", Fuel Processing Technology, 71, 99-119.

[2] Shafiee S., Topal E., (2009), "When will fossil fuel reserves be diminished?", Energy Policy, 37, 181-189.

[3] Singhal S. C., Kendall K., (2003), "High temperature solid oxide fuel cells: fundamentals, design, and applications" Elsevier Science Ltd, 1st Edition, Oxford, UK.

[4] Blomen L. J. M. J., Mugerwa M. N., (1993), "Fuel Cell Systems", 1st Edition, New York, USA.

[5] Appleby A. J., (1990), "From Sir William Grove to today: Fuel Cell and the future", Journal of Power Sources, 29, 3-11.

[6] de Boer B., (1998), "SOFC Anodes: Hydrogen oxidation at porous nickel and nickel/yttria-stabilized zirconia cermet electrodes", Universiteit Twente, Netherlands.

[7] Kirubakaran A., Jain S., Nema R., (2009), "A review on fuel cell technologies and power electronic interface", Renewable and Sustainable Energy Reviews, 13, 2430–2440.

[8] Cascos V., Troncoso L., Alonso J. A., Fernandez-Diaz M.T., (2017), "Design of new Ga-doped $SrMoO_3$ perovskites performing as anode materials in SOFC", Renewable Energy, 111, 476-483

[9] Badwal S. P. S., Foger K., (1996), "Solid Oxide Electrolyte Fuel Cell Review", Ceramics International, 22, 257-265.

[10] Kan W.H., Samson A. J., Thangadurai V., (2016), "Trends in electrode development for next generation solid oxide fuel cells", Journal of Materials Chemistry A, 4, 17913-17932.

[11] Boivin J.C., Mairesse G., (1998), "Recent Material Developments in Fast Oxide Ion Conductors", Chemistry of Materials, 10, 2870–2888.

[12] Orera A., Slater P.R., (2010), "New Chemical Systems for Solid Oxide Fuel Cells" Chemistry of Materials, 22, 675–690.

[13] Singh P., Goodenough J.B., (2012), "$Sr_{1-x}K_xSi_{1-y}Ge_yO_{3-0.5x}$: a new family of superior oxide-ion conductors", Energy & Environmental Science, 5, 9626–9631.

[14] Mori M. Abe T., Itoh H., Yamamoto O., Takeda Y., Kawahara T., (1994), "Cubic-stabilized zirconia and alumina composites as electrolytes in planar type solid oxide fuel cells", Solid State Ionics, 74, 157-164.

[15] Asadikiya M., Sabarou H., Chen M. and Zhong Y., (2016), "Phase diagram for a nano-yttria-stabilized zirconia system", The Royal Society of Chemistry, 6, 17438-17445.

[16] Sun C., Stimming U., (2007), "Recent Anode Advances in Solid Oxide Fuel Cells", Journal of Power Sources, 171, 247–260.

[17] Zhu W. Z., Deevi S. C., (2003), "A review on the status of anode materials for solid oxide fuel cells", Materials Science and Engineering:A volume 362, 228-239

[18] Jadhav S. T., Puri V.R, Jadhav L. D., (2016), "NiO-GDC-BYC composites as an anode for SOFC", Journal of Alloys and Compounds, 685, 626-632.

[19] Muecke U. P., Graf S., Rhyner U., Gauckler L. J., (2008), "Microstructure and electrical conductivity of nanocrystalline nickel oxide/gadolinia-doped ceria thin films", Acta Materialia, 56, 677–687.

[20] Zhang X., Ohara S., Maric R., Mukai K., Fukui T., Yoshida H., Nishimura M., Inagaki T., Miura K., (1999), "Ni-SDC cermet anode for medium-temperature solid oxide fuel cell with lanthanum gallate electrolyte", Journal of Power Sources, 83, 170–177.

[21] Yin Y., Zhu W., Xia C., Meng G., (2004), "Gel-cast NiO-SDC composite as anodes for solid oxide fuel cells", Journal of Power Sources, 132, 36-41.

[22] Liu X., Meng X., Han D., Wu H., Zeng F., Zhan Z., (2013), "Impregnated nickel anodes for reduced-temperature solid oxide fuel cells based on thin electrolytes of doped $LaGaO_3$", Journal of Power Sources, 222, 92-96.

[23] Karim A. H., Park K. Y., Lee T. H., Muhammed Ali S. A., Hossain A., Absah H. Q. H. H., Park J.-Y., Azad A. K., (2017), "Synthesis, structure and electrochemical performance of double perovskite oxide $Sr_2Fe_{1-x}Ti_xNbO_{6-\delta}$ as SOFC electrode", Journal of Alloys and Compounds, 724, 666-673.

[24] Prakash B. S., Kumar S. S., Aruna S. T., (2014), "Properties and Development of Ni/YSZ as an anode material in solid oxide fuel cell: A review", Renewable and Sustainable Energy Reviews, 36, 149-179.

[25] Bieberle A., Gauckler L. J., (2000), "Reaction mechanism of Ni pattern anodes for solid oxide fuel cells", Solid State Ionics, 135, 337–345.

[26] Pecho O. M., Mai A., Münch B., Hocker T., Flatt R. J., Holzer L., (2015), "3D Microstructure Effects in Ni-YSZ Anodes: Influence of TPB Lengths on the Electrochemical Performance", Materials, 8 (10), 7129–7144.

[27] Marina O. A., Mogensen M., (1999), “High-temperature conversion of methane on a composite gadolina-doped ceria-gold electrode”, Applied Catalysis A: General ,189 (1), 117–126.

[28] Mogensen M., Sammes N. M., Tompsett G. A., (2000), “Physical, chemical and electrochemical properties of pure and doped ceria”, Solid State Ionics, 129,63–94.

[29] Tournoux M., Ganne M., Piffard Y., (1992), “HTB-like six-membered rings of octahedra in some new oxides: Structural aspects and related properties”, Solid State Chemistry, 96, 141–153.

[30] Kim M.-S., Wang P., Lee J.-H., Kim J.-J., Lee H. Y., Cho S.-H., (2002), “Site Occupancy and Dielectric Characteristics of Strontium Barium Niobate Ceramics: Sr/Ba Ratio Dependence”, Japanese Journal of Applied Physics, 41, 7042–7047.

[31] Park S., Lang M., Tracy C.L., Zhang J., Zhang F., Trautmanne C., Rodriguez M.D., Kluth P., Ewing R.C., (2015), “Response of $Gd_2Ti_2O_7$ and $La_2Ti_2O_7$ to swift-heavy ion irradiation and annealing”, Acta Materialia, 93, 1-11.

[32] Tao S., Irvine J. T. S., (2004), “Discovery and Characterization of Novel Oxide Anodes for Solid Oxide Fuel Cells”, The Chemical Record, 4, 83-95.

[33] Yu J.H., Park G. W., Lee S., Woo S. K., (2007), Microstructural effects on the electrical and mechanical properties of Ni–YSZ cermet for SOFC anode”, Journal of Power Sources, 163, 926-932.

[34] Dees D. W., Claar T. D., Easier T. E., Fee D. C., and Mrazek F. C., (1987), “Conductivity of porous Ni/ZrO_2-Y_2O_3 Cermets”, Journal of Electrochemical Society, 134, 2141-2146.

[35] Sarikaya A., Petrovsky V., Dogan F., (2012), “Effect of the anode microstructure on the enhanced performance of solid oxide fuel cells,” International Journal Hydrogen Energy, 37, 11370-11377.

[36] Lee J.-H., Moon H., Lee H-W., Kim J., Kim J.-D., Yoon K-H., (2002), “Quantitative analysis of microstructure and its related electrical property of SOFC anode, Ni–YSZ cermet”, Solid State Ionics, 148, 15-26.

[37] Simwonis D., Tietz F., Stover D., (2000), “Nickel coarsening in annealed Ni/8YSZ anode substrates for solid oxide fuel cells” Solid State Ionics, 132, 241-251.

[38] Sun X., Hendriksen P. V., Mogensen M. B., Chen M., (2019), “Degradation in Solid Oxide Electrolysis Cells During Long Term Testing”, Fuel Cells, 19, 1-8.

[39] Web 1 (2020), https://www.energy.gov/fe/science-innovation/clean-coal-research/solid-oxide-fuel-cells, (Date of Access: 17/05/2020).

[40] Young J. L., Vedahara V., Kung S., Xia S. and Birss V. I., (2007), "Understanding Nickel Oxidation and Reduction Processes in SOFC Systems", ECS Transactions, 7, 1511-1519.

[41] Sarantaridis D., Atkinson A., (2007), "Redox Cycling of Ni-Based Solid Oxide Fuel Cell Anodes: A Review.", Fuel Cells, 7(3), 246–258.

[42] Faes A., Hessler-Wyser A., Zryd A., Van herle J., (2012), "A Review of RedOx Cycling of Solid Oxide Fuel Cells Anode", Membranes, 2, 585-664.

[43] Pihlatie M., Kaiser A., Mogensen M., (2009), "Redox Stability of SOFC: Thermal analysis of Ni-YSZ composites", Solid State Ionics, 180, 1100-1112.

[44] Kofstad V.P., (1988), "High temperature corrosion", Elsevier applied science: London/ New York, ISBN 1-85166-154-9.

[45] Faesa A., Nakajo A., Hessler-Wyser A., Dubois D., Brisse A., Modena S., Van herle J., (2009), "RedOx study of anode-supported solid oxide fuel cell", Journal of Power Sources, 193, 55‑64.

[46] Sumi H., Kishida R., Kim J.-Y., Muroyama H., Matsui T., and Eguchi K., (2010), "Correlation Between Microstructural and Electrochemical Characteristics during Redox Cycles for Ni–YSZ Anode of SOFCs", Journal of The Electrochemical Society, 157(12), B1747-B1752.

[47] Buyukaksoy A., Kammampata S. P., Birss V. I., (2015), "Effect of porous YSZ scaffold microstructure on the long-term performance of infiltrated Ni-YSZ anodes", Journal of Power Sources, 287, 349-358.

[48] Szycher M., (1991), "High Performance Biomaterials, A Complete Guide to Medical and Pharmaceutical Applications", Technomic Publishing Co, ISBN No: 87762-7754.

[49] Buyukaksoy A., Petrovsky V., Dogan F., (2012), "Redox Stable Solid Oxide Fuel Cells with Ni-YSZ Cermet Anodes Prepared by Polymeric Precursor Infiltration" Journal of The Electrochemical Society, 159, B232-B234.

[50] Busawon A.N., Sarantidis D., and Atkinson A., (2008), "Ni Infiltration as a Possible Solution to the Redox Problem of SOFC Anodes", Electrochemical and Solid-State Letters, 11(10), B186-B189.

[51] Buyukaksoy A., Petrovsky V., and Dogan F., (2012), "Optimization of Redox Stable Ni-YSZ Anodes for SOFCs by Two-Step Infiltration", Journal of The Electrochemical Society, 159, 12, F841-F848.

[52] Klemensø T., Thydén K., Chen M., Wang H-J., (2010), "Stability of Ni yttria stabilized zirconia anodes based on Ni-impregnation", Journal of Power Sources, 195, 7295-7301.

[53] Muecke U.P., Graf S., Rhyner U., Gauckler L. J., (2008), “Microstructure and electrical conductivity of nanocrystalline nickel oxide/gadolinia-doped ceria thin films”, Acta Materialia, 56, 677–687.

[54] Ayhan Y.S., Buyukaksoy A., (2019), “Impact of fabrication temperature on the stability of yttria doped bismuth oxide ceramics”, Solid State Ionics, 338, 66–73.

[55] Anderson H. U., Nasrallah M. M., Chen C. C., (1996), “Method of coating a substrate with a metal oxide film from an aqueous solution comprising a metal cation and a polymerizable organic solvent”, American Patent, No: 5, 494, 700.

[56] Mohebbi H., Ebadzadeh T., Hesari F.A., (2008), “Synthesis of nano-crystalline (Ni/NiO)-YSZ by microwave-assisted combustion synthesis method: The influence of pH of precursor solution”, Journal of Power Sources, 178, 64-68.

[57] Razpotnik T., Macek J., (2007), “Synthesis of nickel oxide/zirconia powders via a modified Pechini method,” Journal of European Ceramic Society, 27, 1405-1410.

[58] Han K. R., Jeong Y., Lee H., Kim C-S., (2007), “Fabrication of NiO/YSZ anode material for SOFC via mixed NiO precursors”, Materials Letters, 61, 1242-1245.

[59] Tai L-W., Lessing P. A., (1992), “Modified resin-intermediate processing of perovskite powders: Part I. Optimization of polymeric precursors”, Journal of Materials Research, 7, 502-510.

[60] Laberty-Robert Ch., Ansart F., Deloget C., Gaudon M., Rousset A., (2001), “Powder Synthesis of nanocrystalline ZrO_2-8%Y_2O_3 via a polymerization route”, Materials Research Bulletin, 36, 2083–2101.

[61] Li S., Guo R., Li J., Chen Y., Liu W., (2003), “Synthesis of NiO–ZrO2 powders for solid oxide fuel cells”, Ceramics International, 29, 883–886.

[62] Shih F-Y., Fung K-Z., Lin H-C., Chen G-J., (2006), “Low-temperature synthesis of nanocrystalline NiO–YSZ powders by succinic acid-assisted combustion”, Journal of Power Sources, 160, 148–154.

[63] Suciu C., Hoffmann A. C., Dorolti E., Tetean R., (2008), “NiO/YSZ nanoparticles obtained by new sol–gel route”, Chemical Engineering Journal ,140, 586–592.

[64] Lee M-J., Hong S-K., Choi B-H., Hwang H-J., (2016), “Fabrication and performance of solid oxide fuel cell anodes from core-shell structured Ni/yttria-stabilized zirconia (YSZ) powders, Ceramics International, 42, 10110-10115.

[65] Dasari H. P., Park S-Y., Kim J., Lee J-H., Kim B-K., Je H-J., Lee H-W., Yoon K. J., (2013), “Electrochemical characterization of Ni-yttria stabilized zirconia

electrode for hydrogen production in solid oxide electrolysis cells," Journal of Power Sources, 240, 721-728.

[66] Dierickx S., Joos J., Weber A., Ivers-Tiffée E., (2018), "Advanced impedance modelling of Ni/8YSZ cermet anodes," Electrochimica Acta, 265, 736-750.

[67] Buyukaksoy A., Birss V. I., (2016), "Comparison of the Electrochemistry of Ni Thin Film and Ni-YSZ Composite Anodes Fabricated by Polymeric Precursor Deposition," Journal of The Electrochemical Society, 163, F1350-F1357.

[68] Sonn V., Leonide A., and Ivers-Tiffée E., (2008), "Combined deconvolution and CNLS fitting approach applied on the impedance response of technical Ni8YSZ cermet electrodes," Journal of the Electrochemical Society, 155, B675-B679.

[69] Hasannejad H., Aliofkhazraei M., Shanaghi A., Shahrabi T., Sabour A. R. (2009), "Nanostructural and electrochemical characteristics of cerium oxide thin films deposited on AA5083-H321 aluminium alloy substrates by dip immersion and sol–gel methods", Thin Solid Films, 517, 4792–4799.

[70] Tang L., Salamon M., de Guire M. R., (2010), "Cerium Oxide Thin Films on Solid Oxide Fuel Cell Anodes", Science of Advanced Materials, 2(1), 79-89.

[71] Xi X., Abe H., Naito M., (2014), "Effect of composition on microstructure and polarization resistance of solid oxide fuel cell anode Ni-YSZ composites made by co-precipitation", Ceramics International ,40(10), 16549-16555.

[72] Andersson M., Yuan J., Sundén B., (2012), "SOFC Modeling Considering Electrochemical Reactions at the Active Three Phase Boundaries", International Journal of Heat and Mass Transfer ,55 (4-5), 773-788.

[73] Costa-Nunes O., Gorte R. J., Vohs J. M., (2005), "Comparison of the performance of Cu–CeO2–YSZ and Ni–YSZ composite SOFC anodes with H2, CO, and syngas", Journal of Power Sources, 141(2), 241-249.

[74] Noh H-S., Son J-W., Lee H., Ji H. I., Lee J. T. and Lee H.-W., (2010), "Suppression of Ni agglomeration in PLD fabricated Ni-YSZ composite for surface modification of SOFC anode", Journal of the European Ceramic Society, 30(16), 3415–3423.

[75] Buyukaksoy A., Birss V. I., (2015), "Stabilization of Ni-YSZ Nanocomposite Anodes by Deposition of a Thin YSZ Overlayer", ECS Transactions, 66(2), 267-274.

[76] Ding C., Sato K., Mizusaki J., Hashida T. (2012), "A comparative study of NiO-$Ce_{0.9}Gd_{0.1}O_{1.95}$ nanocomposite powders synthesized by hydroxide and oxalate co-precipitation methods", Ceramics International, 38, 85-92.

[77] Akbari-Fakhrabadi A., Avila R. E., Carrasco H. E., Ananthakumar S., Mangalaraja R. V. (2012), "Combustion synthesis of NiO-$Ce_{0.9}Gd_{0.1}O_{1.95}$

nanocomposite anode and its electrical characteristics of semi-cell configured SOFC assembly", Journal of Alloys and Compounds 541, 1-5.

[78] Prakash B. S., Pavitra R., Kumar S. S. and Aruna S. T., (2017), "Evalution of solution combustion synthesized NiO-GDC ceramic powders for anode substrate and anode functional layers of intermediate temperature solid oxide fuel cell", Ceramics International, 43, 12138-12144.

[79] Lim C-H., Lee K.T., (2016), "Characterization of core-shell structured Ni@GDC anode materials synthesized by ultrasonic spray pyrolysis for solid oxide fuel cells", Ceramics International, 42, 13715-13722.

[80] Pezeshkpour S., Salamatinia B., Amini B.H., (2017), "Synthesis and characterization of nanocrystalline NiO-GDC via sodium alginate-mediated ionic sol-gel method", Ceramics International, 44, 3201-3210.

BIOGRAPHY

Buse Bilbey was born in 1995 in Kadıköy/ISTANBUL. Graduated BS degree from Materials Science and Engineering, Department of Gebze Technical University in 2017. At the same year started M.Sc. degree from Materials Science and Engineering, Department of Gebze Technical University. She worked in "Development of Low Temperature Solid Oxide Fuel Cells with High Performance and Durability" 217M031 TUBITAK Project in 2018-2020. Her research area is Solid Oxide Fuel Cells, mostly focused on fabrication and characterization of the nanocomposite anodes.

APPENDICES

APPENDIX A: Publication and Proceedings

Journal Paper:

[1] Bilbey B., Erol G., Buyukaksoy A. (2020), "Structural, Microstructural and Electrochemical Characterization of Ni-YSZ Anodes Fabricated from PechiniDerived Composite Powders.", Sakarya University Journal of Science, 24(4), 740-750, DOI: https://doi.org/10.16984/saufenbilder.659147.

Conference Proceedings:

[1] Bilbey B., Sezen M., Ow-Yang C., Buyukaksoy A., "Microstructure, performance and stability of thin film Ni-YSZ anodes", EFCF 2020, 14th European SOFC & SOE Forum 2020 (October 2020), Luzern/Switzerland.

[2] Bilbey B., Sezen M., Ow-Yang C., Buyukaksoy A., "Addressing the Performance Degradation Issue in Nanoscaled Ni-YSZ Anodes in Solid Oxide Fuel Cells", Electroceramics XVII (August 2020), Darmstadt/Germany.

[3] Bilbey B., Sezen M., Ow-Yang C., Buyukaksoy A., "Influence of Processing Conditions on the Electrochemical Performance of Ni-YSZ Thin Film Anodes Prepared by Polymeric Precursor Deposition", mESC-IS 2019, 4th International Symposium on Materials for Energy Storage and Conversion, Muğla, Turkey.

[4] Bilbey B., Smitshuysen A., Skafte T., Jensen S.H., Büyükaksoy A., "Development of NiO-YSZ Precursors for Solid Oxide Fuel Cell Anode Fabrication", SERES'18 IV. International Ceramic, Glass, Porcelain, Enamel, Glaze and Pigment Congress, Eskişehir,Turkey.

[5] Bilbey B., Erol G., Buyukaksoy A, "Development of NiO-YSZ Precursors for Solid Oxide Fuel Cell Anode Fabrication", Gebze Teknik Üniversitesi Fen Bilimleri Enstitüsü, Lisansüstü Araştırmalar Sempozyumu & Tanıtım Günleri, Kocaeli/Turkey.

APPENDIX B: Preliminary Experiments with Ni-GDC Cermet Anode

Phase Analysis

Although main study of this thesis is Ni-YSZ anodes, after the experiments done with Ni-YSZ GDC used instead of YSZ as ionic conductor with electro catalyser Ni, GDC has better ionic conductivity and more resistance to Ni coarsening than YSZ. Because of the ceria used for overlay coating to prevent the Ni migration on anode surface, we also characterized CeO_2. To determine the crystallization behaviour of GDC, Ni-GDC and Ceria polymeric precursors, as mentioned before in experimental part, GDC, composite Ni-GDC and Ceria polymeric precursor gels dried and calcined 600,700 and 800˚C for 4 hours in stagnant air atmosphere for the obtain powders with the same way. XRD data was collected between 2θ=10-90˚C with rate of 2˚C per minute. NiO XRD pattern also added in figure B.1.a to compare composite NiO-GDC powder. Cubic structured GDC phase (PDF: 01-075-0161) were observed all calcined powders, xrd pattern shown in figure B.1.b. Cubic GDC peaks are at 2θ =28,51˚, 33,04˚, 47,42˚, 56,27˚, 59,01˚, 69,32˚, 76,60˚, 78,96˚, and 88,30˚. Composite NiO-GDC powder xrd patterns obtained from polymeric precursors shown in figure in figure B.1.c Cubic NiO and GDC phases crystallized separately all calcination temperatures in NiO-GDC powder like NiO-YSZ powder. Cubic structured ceria phase (PDF: 03-065-59-23) were observed all calcined powders, peaks are at 2θ =28,59˚, 33,13˚, 47,56˚, 56,43˚, 59,18˚, 69,53˚, 76,83˚, 79,21˚, and 88,59˚ shown in in figure B.1.d.

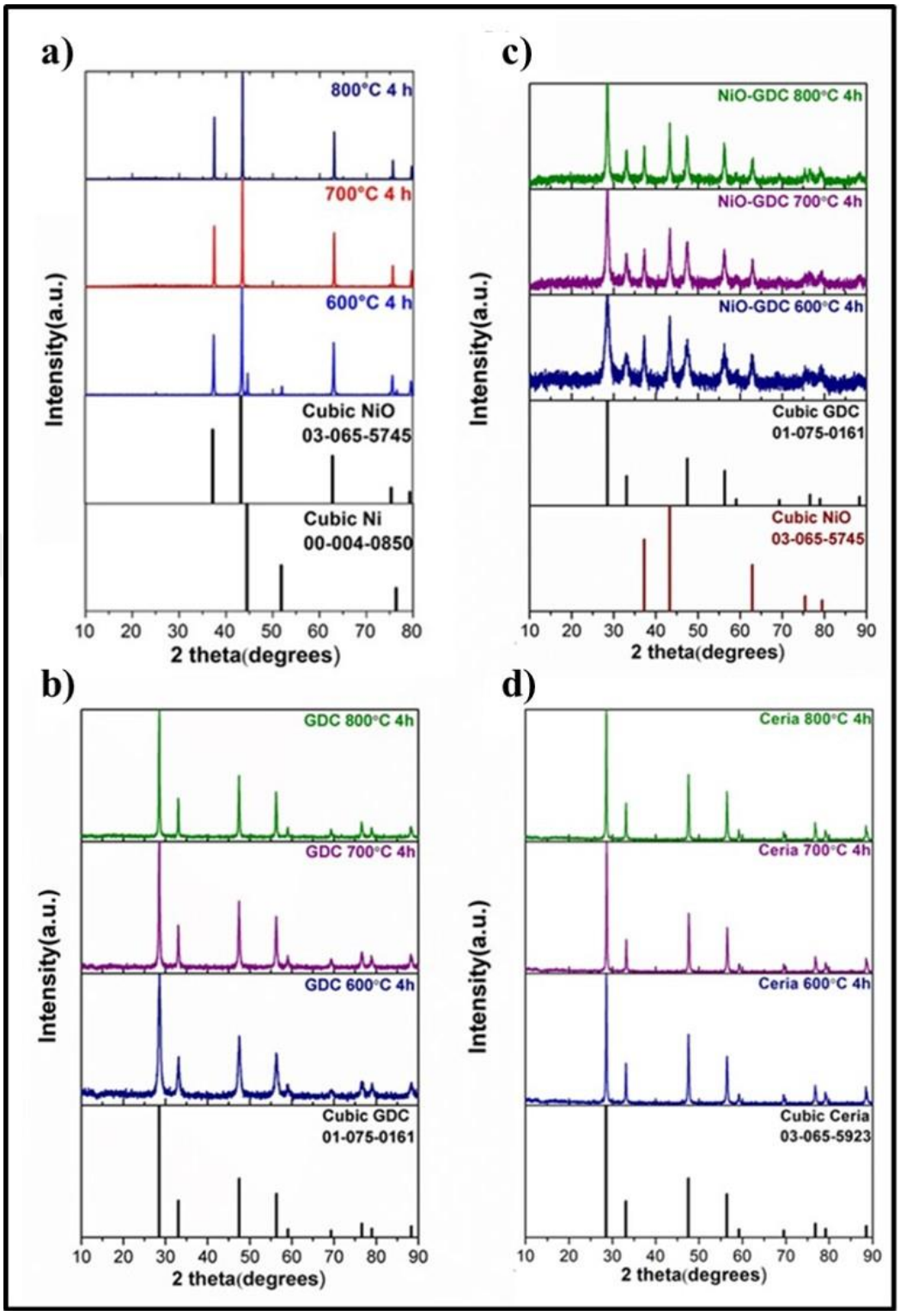

Figure B.1: XRD Patterns of a) NiO b) GDC c) NiO-GDC and d) Ceria, powders calcined at 600°C, 700°C, 800°C for 4 hours.

Crystallite Size

Also, to determine the crystallization in NiO-GDC average crystallite sizes of NiO, GDC and NiO-GDC phases from the XRD pattern peaks calculated, shown in figure B.2. Average crystallite sizes of NiO and GDC phase increases with increasing calcination temperatures separate and in the composite powders derived from polymeric precursors, while ceria crystallite size has not significantly change. The crystallite size of the NiO phase from 600 to 800 ˚C in separate NiO powder is same (45,26, 51,13 and 59,60 nm), and in composite powder is 5,09, 11,02 and 14,44 nm. Crystallite size of NiO phase significantly smaller in composite NiO-GDC precursor than single precursor derived NiO also smaller than NiO-YSZ. As same in YSZ, presence of Ce^{4+} and Gd^{3+} ions are hinder the clustering of Ni^{2+}, that is resulting smaller NiO crystal in NiO-GDC composite precursor than the separate NiO precursor. The crystallite size of GDC is 600 to 800 ˚C in separate 12,71, 23,43 and 29,83 nm and in composite NiO-GDC 3,52, 8,79 and 13,07 nm. Average crystallite sizes of GDC higher than YSZ in separate, and GDC crystallization lower in NiO-GDC on the other hand YSZ crystallization increases in NiO-YSZ. NiO average crystallite size in NiO-GDC significantly lower than NiO-YSZ, but both composites with NiO range of the crystallization YSZ and GDC is similar. In NiO-GDC composite powders derived from polymeric precursors average NiO and GDC crystal sizes range of 5-14 and 4-13 nm upon calcination 600 to 800˚C.

C. Ding et al. prepared NiO-GDC powders with hydroxide and oxalate reverse co-precipitation method, that study shows NiO crystallites grows quicker than the GDC and different crystallite sizes achieved by different synthesis methods because of the different mechanisms.[76] A. Akbari-Fakrabadi et al. produced NiO-GDC anode by combustion synthesis method, crystallite size calculated before calcination founded 16 and 9 nm for NiO and GDC. After calcination at 600˚C crystallite size of NiO increased 21 nm while GDC stayed same size, thus crystal growth observed at NiO [77]. B. Shri Prakash et al. synthesized NiO-GDC powders with solution combustion method by using oxalyl di hydrazide (ODH) and hexamethylenetetramine (HMT) fuels. Crystallite size of NiO 6-31 nm and GDC 4-20 nm calculated change with different fuel and different volume of %NiO.[78] In the study of C.-H. Lim and K.-T. Lee core shell structured Ni-GDC produced different pH and carrier gas flow rate by ultrasonic spray pyrolysis method, achieved

crystallite size of NiO was 12.8-18.8 nm and GDC crystallite size was 10.8-16 nm. [79] All studies mentioned from the literature NiO has larger crystallite size than GDC, but in our study NiO and GDC crystallite size very similar.

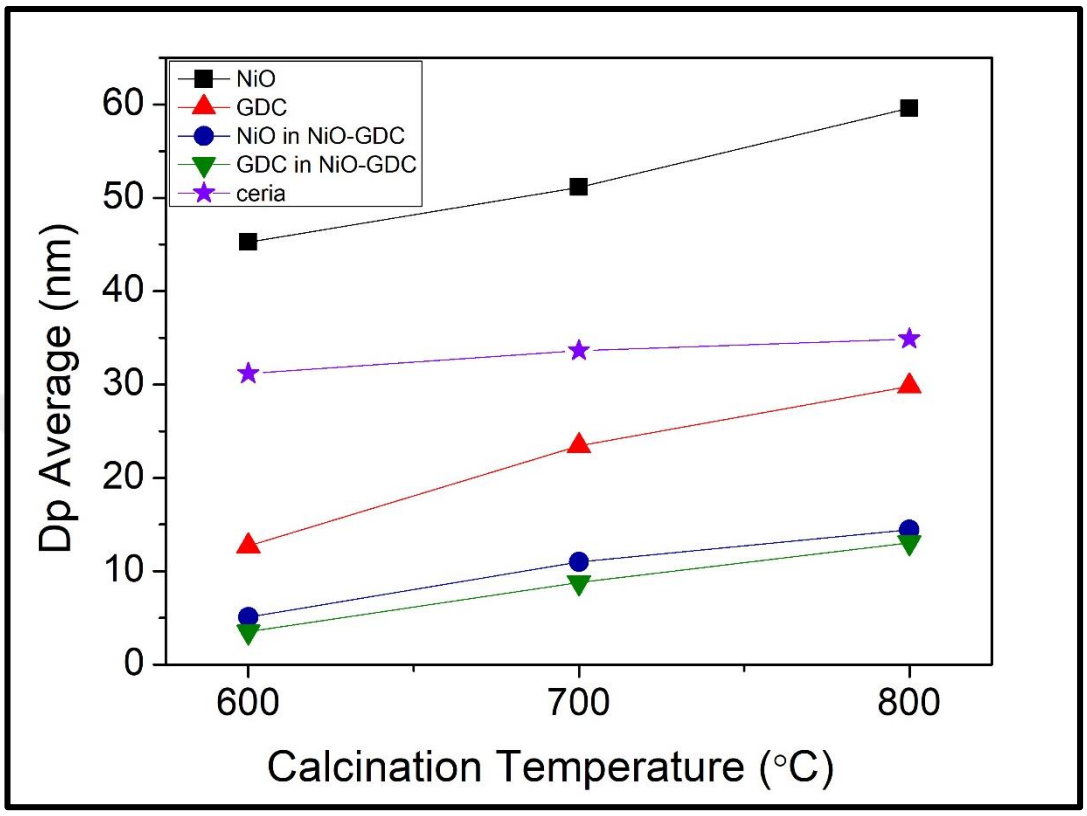

Figure B.2: Average crystallite size of Ceria, NiO GDC and NiO and GDC in NiO-GDC powders.

Thermal Analysis

Differential thermal and thermogravimetric analysis were used for thermal analysis to examine property change of the samples with a function of the chancing temperature. Gels derived from the polymeric precursor of NiO, GDC, composite NiO-GDC and Ceria dried at 120˚C to analysis, measurements took place between room temperature to 1000˚C. Analysis of NiO mentioned before in NiO-YSZ cermet anode part but for the see difference between NiO and composite NiO-GDC also shown again in figure B.3.a. Figure B.3.b shows DTA/TGA analysis of GDC powders derived from the polymeric precursor, two exothermic peaks observed at 280 and 540˚C, and an endothermic peak observed at ca. 900˚C. DTA/TGA analysis of composite NiO-GDC powder shown in figure B.3.c two exothermic peaks

observed at 325 and wider one at 700˚C. Figure B.3.d. shows DTA/TGA analysis of Ceria exothermic peaks observed at 225, 275 and 550˚C.

In the study of C. Ding et al. co-precipitation with hydroxide gives endothermic peaks at 53.8 and 279.1˚C while endothermic peaks at 125.0 and 229.0˚C and an exothermic peak at 338.7˚C observed with oxalate. [76] Combustion synthesis NiO-GDC analysed with DTA-TGA in the study of A. Akbari-Fakrabadi et al. Two thermal decomposition observed below 300˚C and 300 to 500˚C weight gained then the gained weight decreased steeply [77]. C.-H. Lim and K.-T. Lee produced Ni-GDC by ultrasonic spray pyrolysis method from Ni acetate, Gd and Ce nitrate, and TGA data shows dehydration between 133-178˚C and thermal decomposition between 262-378˚C [79]. S. Pezeshkpour et al. produced NiO-GDC with Na-Alginate mediated ionic sol gel method and 4 step weight loss observed 25-186, 186-301, 301-380 and 380-500 from thermogravimetric analysis [80].

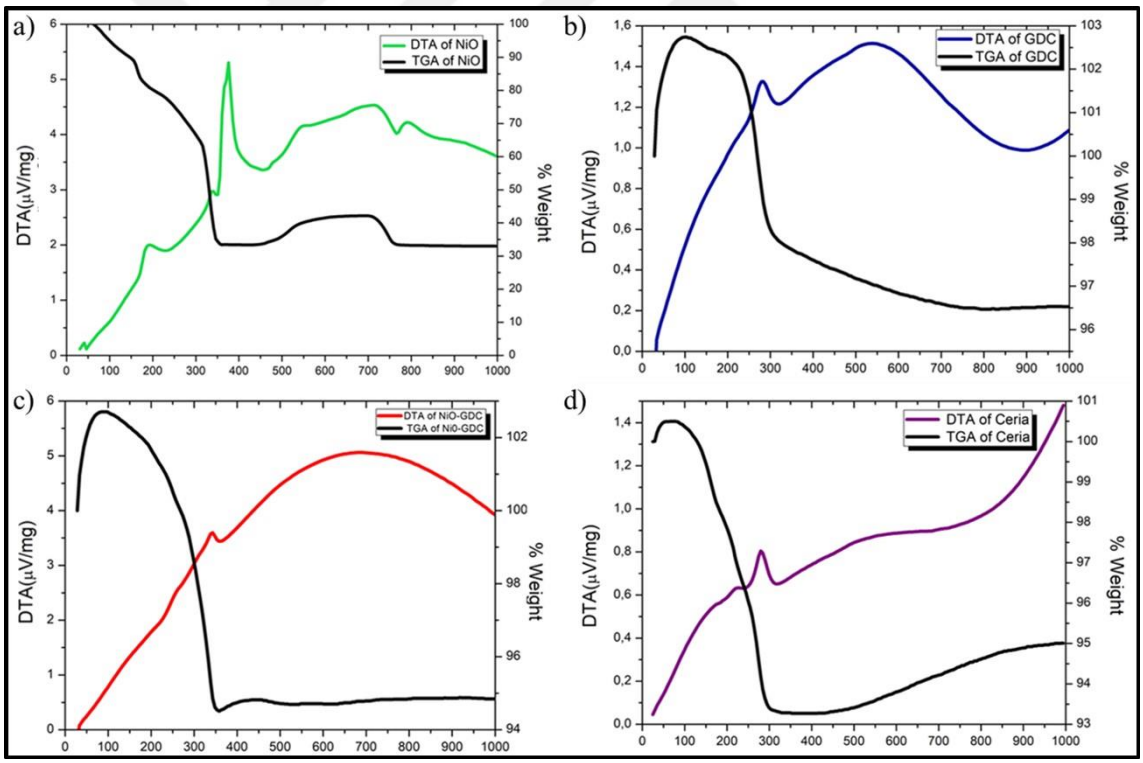

Figure B.3: DTA/TGA analysis of a) NiO b) GDC c) NiO-GDC.

Precursor Stabilities

As polymeric solution stability important for the thin film coating viscosities change with time and temperature shown in figure B.4. Viscosity of GDC when first prepared was 71.9 mPa.s at 23.4˚C after 292 hours viscosity 54.4 mPa.s measured at 27.3˚C, increasing temperature effect on viscosity that much if we look similar temperature e.g. 122.95 hours later viscosity measured 72.2 at 22.1˚C, in figure B.4.a. GDC polymeric precursor stable with time and we also know polymeric precursor of NiO stable with time shown in figure B.4.b. Composite NiO-GDC polymeric precursor viscosity decreased from 42.1 to 29.1 mPa.s at the 23.6 and 27.9˚C 312.45 hours later, also NiO-GDC polymeric precursor is stable with time, temperature change caused that much viscosity difference, in figure B.4.c. And polymeric precursor of ceria measured in figure B.4.d, viscosity decreased 288.63 hours later from 44.9 to 24.5 mPa.s at 23.6 to 27.7˚C, ceria is also stable with time. While NiO-YSZ polymeric precursor is not stable with time NiO-GDC polymeric precursor is more stable.

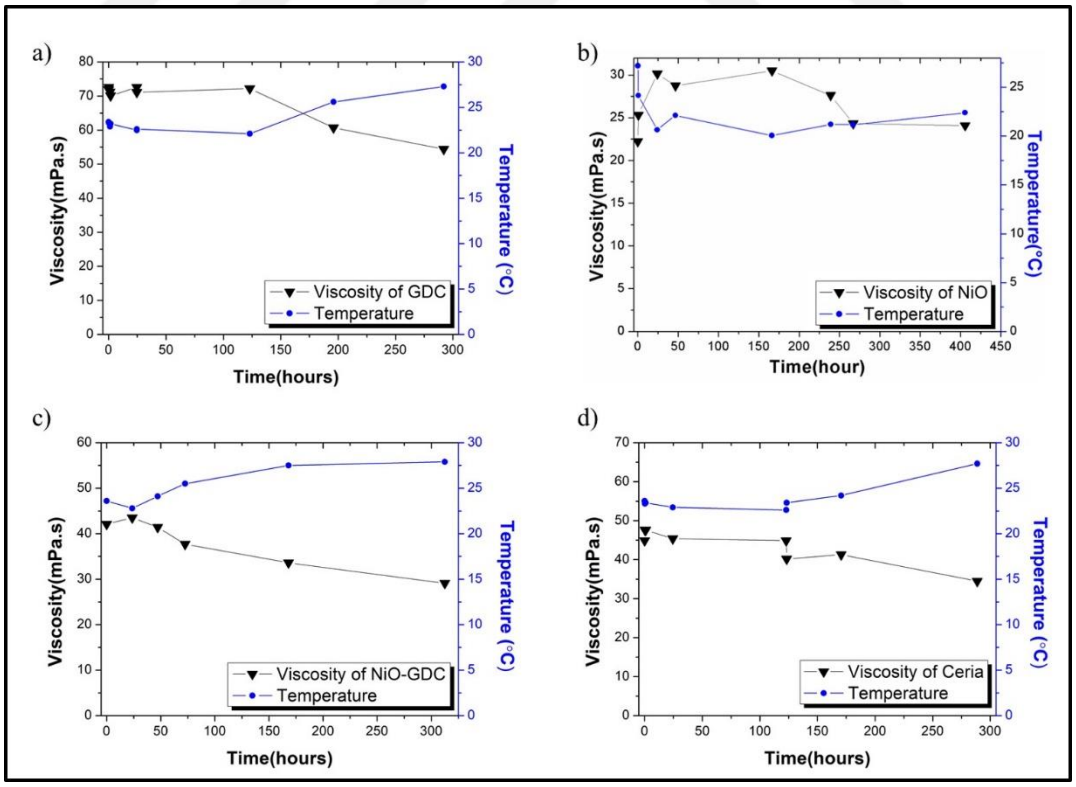

Figure B.4: The change of viscosity a) GDC b) NiO C) NiO-GDC and d) Ceria polymeric precursors with time.

Microstructure of Ni-GDC Thin Film

To observe initial microstructure and long-term stability, NiO-GDC composite polymeric precursor coated with spin coater at 3000 rpm and heat treated at 400˚C that deposition cycle repeated 20 times, microstructure analysed with SEM in figure B.5.a. Sample reduced to Ni-GDC and 100 h waited under 10% H_2-90% Ar atmosphere at 600˚C, that microstructure shown in figure B.5.b. After the long-term testing conditions ca. 50 nm Ni particles coarsen on the surface. That coarsening more than the Ni-YSZ cermet anodes.

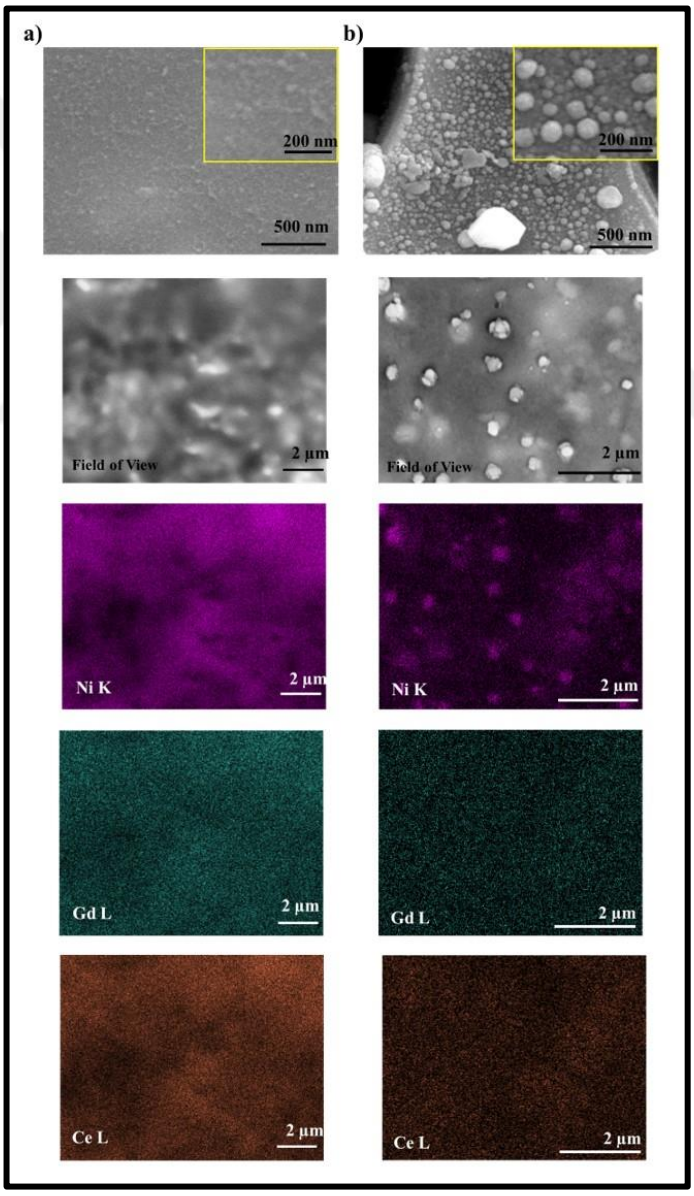

Figure B.5: Microstructure of a) NiO-GDC thin film b) Ni-GDC film reduced at 600˚C for 100 h.

Electrochemical Activity of Ni-GDC Anode

For the electrochemical activity test 5 ceria overlayer coated Ni-GDC thin film used. Compared with the Ni-YSZ sample which is prepared same condition with the Ni-GDC. ASR_{anode} of the Ni-GDC thin film 0.55 while Ni-YSZ is 1.65 $\Omega.cm^2$, in figure B.6. GDC has better ionic conductivity than the YSZ thus that improves anode performance.

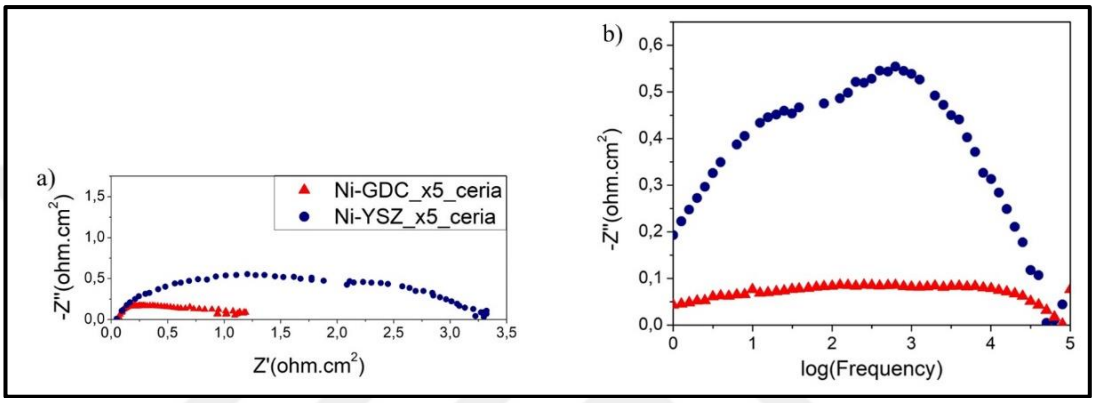

Figure B.6: a) Nyquist b) Bode Diagram of Ni-YSZ and Ni-GDC anod with 5 overlayer ceria coating.

APPENDIX C: Redox Stability

For the redox stability, Ni-YSZ anode with ceria overlayer coated measured at 600˚C and after 3 redox cycle change in the ASR_{anode} shown in figure C.1. Reducing atmosphere interrupted 15 minutes then air flushed with Ar and exposed to reducing 10%H_2-90%Ar atmosphere, that cycle repeated 3 times. After the redox cycle improvement observed on the ASR_{anode}.

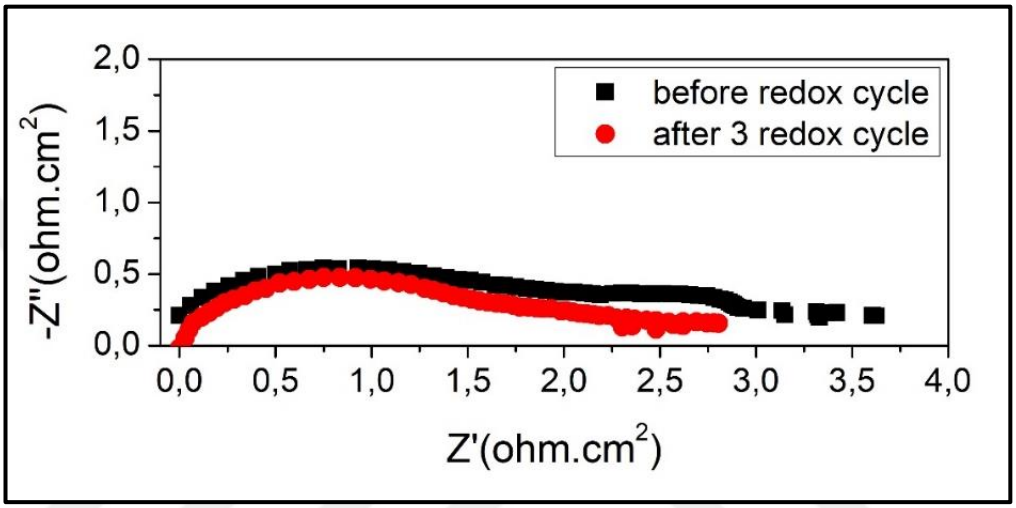

Figure C.1: ASR_{anode} change after redox cycle.